HELSINGIN YLIOPISTO
HELSINGFORS UNIVERSITET
UNIVERSITY OF HELSINKI

Master`s thesis
Master´s Programme in Geology and Geophysics
Petrology and Economic Geology

Age constraints for the mineralization of the metamorphosed Kutemajärvi gold deposit using the single-grain U-Pb dating method of accessory minerals

Georgios Dimakopoulos
April 2022

HELSINGIN YLIOPISTO
MATEMAATTIS-LUONNONTIETEELLINEN TIEDEKUNTA

PL 64 (Gustaf Hällströmin katu 2)
00014 Helsingin yliopisto

HELSINGIN YLIOPISTO
HELSINGFORS UNIVERSITET
UNIVERSITY OF HELSINKI

Tiedekunta/Osasto Fakultet/Sektion – Faculty Faculty of Science	Osasto/Institution – Department University of Helsinki-Department of Geosciences and Geography	
Tekijä/Författare – Author Georgios Dimakopoulos		
Työn nimi/Arbetets titel – Title Age constraints for the mineralization of the metamorphosed Kutemajärvi gold deposit using the single-grain U-Pb dating method of accessory minerals		
Maisteriohjelma, opintosuunta/Magister Program, studier inriktning – Master´s Programme, Study Track Master's Programme in Geology and Geophysics, Petrology and Economic Geology		
Työn laji/Arbetets art – Level Master's Thesis	Aika/Datum – Month and year 04/2022	Sivumäärä/ Sidoantal – Number of pages 90

Tiivistelmä/Referat – Abstract

The metamorphosed Kutemajärvi gold deposit is located near the town of Orivesi, at the eastern flank of the Tampere Schist Belt, which constitutes part of the Svecofennian domain of southern Finland, and it is hosted in the volcanic rocks of the Koskuenjärvi formation. Previous isotopic studies have mainly focused on the igneous and metamorphic rocks of the Tampere Schist Belt and only a few of them have presented ages for the area of Kutemajärvi. This study aims to shed light on the timing of mineralization by employing the single-grain U-Pb dating method of monazite and zircon, in order to evaluate the relationship between the ore and its host rocks.

Based on the results from the SEM mineral identification, monazite grains are divided into metamorphic and hydrothermal grains. In the case of zircon grains, a third magmatic type has been identified. Results from U-Pb dating of single monazite and zircon grains are well constrained and document four distinct stages of geodynamic evolution in the region. Ages older than 1.91 Ga represent detrital material transported during the stage of rifting that led to the opening of the Tampere basin. Subsequent subduction resulted in active volcanism which is expressed with the extrusion of the Koskuenjärvi formation at 1904 Ma. At the late stages of subduction or at the outset of the collision stage, the subvolcanic Pukala porphyry intruded into the volcanic sequence of the Tampere Schist Belt at 1890 Ma, which provides the maximum mineralization age. Release of hydrothermal fluids, due to the crystallization of the Pukala intrusion caused pervasive hydrothermal alteration of the Kutemajärvi host rocks and deposition of epithermal gold and other elements. However, the participation of hydrothermal fluids, released by high-temperature metamorphism of the lower crust, cannot be ruled out. Ages between 1890–1878 Ma record the syn-collision stage, during which the deposit, the Pukala intrusion and its adjoining rocks were deformed and metamorphosed at greenschist to lower-amphibolite facies. The majority of ages fall within the 1880–1878 Ma time-interval, characterizing the metamorphic peak that marks the culmination of the Svecofennian orogeny and provides a minimum age of the mineralization. This major orogenic event is partly overlapped by the collision of the Central Svecofennian Arc Complex with the Southern Svecofennian Arc Complex that transpired at 1880–1860 Ma, as indicated by ample age data. Monazite and zircon also yield lower ages (<1860 Ma), which record retrograde metamorphic and subordinate cooling events, and resonate recurring tectonothermal activity, associated with the syn- and post-collisional magmatism of Southern Svecofennia and the emplacement of rapakivi intrusions in southern Finland.

Single-grain U-Pb dating of monazite and zircon from polished thin sections, in tandem with collation of the obtained ages with earlier published data, establishes a spatial and temporal framework with respect to the tectonometamorphic evolution of the Kutemajärvi gold deposit and the Tampere Schist Belt. Precise temporal constraints substantiate the intricate geological history of the area and can be used to discriminate magmatic, metamorphic and hydrothermal events, with a view to breaking ground on the exploration of other epithermal deposits in the metamorphic terranes of southern Finland.

Avainsanat – Nyckelord – Keywords
Kutemajärvi gold deposit, Orivesi, epithermal deposits, U-Pb geochronology, Tampere Schist Belt, Svecofennian domain

Säilytyspaikka – Förvaringställe – Where deposited
HELDA-Digital repository of the University of Helsinki

Muita tietoja – Övriga uppgifter – Additional information
The thesis was done in collaboration with the University of Helsinki and the Geological Survey of Finland

CONTENTS

1. Introduction

1.1. Classification of gold deposits

Classification of ore deposits simplifies the process of understanding their formation mechanisms and permits the evaluation of prospects for selected areas, which are crucial factors for the determination of strategic planning in exploration. Commonly used attributes to discriminate gold deposits include the genetic and geochemical processes, the host-rock types, the geotectonic setting and the nature of the ore (i.e. mineralogy and texture) (Robert et al. 1997). For economic gold deposits, Phillips and Powell (2015) proposed a classification based on their content in base metals and the gold chemistry with respect to metal complexing, as well as the salinity and the redox state of the mineralizing fluids.

The main bedrock gold deposit types that are distinguished, according to the aforementioned geological attributes are: paleoplacer deposits, submarine gold-rich massive sulfide deposits, hot spring deposits, epithermal deposits, porphyry gold deposits, breccia pipe deposits, skarn gold deposits, carbonate replacement (manto) deposits, sediment-hosted micron gold deposits, non-carbonate stockwork-disseminated gold deposits, Au-Cu sulfide-rich vein deposits, batholith-associated quartz vein deposits, greenstone-hosted quartz-carbonate vein deposits, turbidite-hosted quartz-carbonate vein deposits, and iron-formation-hosted vein and disseminated deposits (Robert et al. 1997).

Many of these deposit types are genetically related and correlate with large hydrothermal systems around magmatic intrusions, active at the same crustal levels, whereas others (e.g. porphyry and skarn gold deposits) can occur in several settings (Robert et al. 1997, Walshe and Cleverley 2009). Moreover, some gold deposits can be identified by one parameter, for instance the quartz texture that is affiliated to a specific type (Dowling and Morrison 1989). Elemental association is diagnostic for particular gold deposit types for fluid-dominated hydrothermal systems, owing to the similar ore-forming processes, but it is less informative for rock-dominated systems. Consequently, despite that elemental suites can be used for the accurate identification of a specific deposit type, they are not considered as a universal indicator in gold exploration (Robert et al. 1997).

1.2. Age dating of gold mineralizing events

The exact timing of mineralization is critical in order to comprehend the genetic model and the geological setting of ore deposits. Therefore, geochronological studies aid to form better understanding of the ore-forming processes and the spatial and temporal relationship between a mineral deposit and its host rocks. Dating of accessory and ore minerals is a useful tool, based on the fundamental principles of isotope geochemistry, providing insight on the formation age of ore deposits.

There are various methods of radiometric geochronology that are utilized to date the different types of gold deposits. In the case of orogenic, lode and epithermal gold deposits, the K-Ar, Rb-Sr or $^{40}Ar/^{39}Ar$ methods have been widely used to date hydrothermal micas (Selby et al. 2002, Mortensen et al. 2010), adularia (Sanematsu et al. 2005, Márton et al. 2010), biotite, and feldspar (Siani et al. 2015). Re-Os geochronology has been extensively applied to sulfides such as molybdenite (Stein et al. 1998, Steven et al. 2013), arsenopyrite (Selby et al. 2002, Morelli et al. 2005; Molnár et al. 2018, Wang et al. 2019), pyrite (Stein et al. 1998, Mathur et al. 1999, Feng et al. 2009, Hnatyshin et al. 2015, Liu et al. 2020), chalcopyrite (Freydier et al. 1997, Barra et al., 2003, Deng et al., 2016a), bornite, and chalcocite (Selby et al. 2009). Epithermal pyrite has also been dated with the Rb-Sr method (Wang et al. 2014).

Direct dating of gold in ore deposits with the U-Th-^{4}He method is also feasible, as demonstrated by Cabral et al. (2013), without presuming concurrence between gold and the hydrothermal minerals being dated. He and Ar isotopic studies have also been applied to sulfides (pyrite, arsenopyrite, chalcopyrite etc.) of several ore deposit types, including principally orogenic gold deposits (Hu et al. 2004, Morelli et al. 2007, Zhu and Peng, 2015, Wang et al. 2019), porphyry copper deposits (Kendrick et al. 2001), and uranium deposits (Hu et al. 2009). U-Pb is also a typical dating method in both rock-forming and hydrothermal minerals, such as zircon (Pelleter et al. 2007, Käpyaho et al. 2017, Molnár et al. 2018), baddeleyite (Fielding et al. 2018), monazite (Fielding et al. 2017, Pohjolainen et al. 2017, Molnár et al. 2018), xenotime (Fielding et al. 2017, 2018, Molnár et al. 2018), titanite (Käpyaho et al. 2017), and arsenopyrite (Mortensen et al., 2010, Fielding et al. 2017, 2018).

In terranes with intricate geotectonic history, metamorphism has a profound effect in the preservation of the original ages in some of the radiogenic isotopic systems noted above. Elements of these isotopic systems reside in major and accessory silicate minerals,

as well as in ore minerals that are less susceptible to post-crystallization modification; a feature that renders them a powerful geochronological tool. Furthermore, elemental solubility in fluids varies considerably, depending on the physical and chemical parameters (pressure, temperature, and composition) of the fluids. Thus, isotopic systems, such as Rb-Sr remain unperturbed during metamorphism, hydrothermal alteration, or weathering, whilst the U-Pb, K-Ar and $^{40}Ar/^{39}Ar$ systems experience loss or addition of radiogenic material. The U-Th-^{4}He system in gold also remains a closed system, due to gold's high retentivity for ^{4}He (Cabral et al. 2013). The He and Ar isotope ratios exhibit minor discrepancies, owing to the enhanced ability of sulfides to sequester noble gases, and hence the He-Ar system is suitable for dating of mainly orogenic gold deposits (Hu et al. 2004, Morelli et al. 2009, Zhu and Peng, 2015, Wang et al. 2019), but also porphyry copper deposits (Kendrick et al. 2001) and uranium deposits (Hu et al. 2009). In reality, nonetheless, hardly any system remains closed during metamorphism, causing partial removal or introduction of the trapped elements. It is a common phenomenon that even resistant mineral grains yield discordant ages that should be interpreted with extreme caution in order to separate the primary crystallization ages from the subsequent metamorphic ages.

In spite of the utilized method, gold exploration is highly contingent on the successful dating of suitable minerals that provide absolute ages for one or multiple mineralizing events. In addition, thorough geochronology promotes the association between mineralization and specific tectonomagmatic events, thereby facilitating exploration by focusing on the most prospective areas within the endowed regions. A typical example of the significance of geochronology in exploration are the orogenic gold deposits, which are located in geotectonically complex regions (Fielding et al. 2017).

1.3. Aims of the study

Within the Tampere Schist Belt, isotopic studies have managed to determine the ages of different events with respect to its tectonometamorphic evolution. Previous research has focused predominantly on the geochronology and geochemistry of the igneous and metamorphic rocks that constitute the Tampere Schist Belt, but only a few studies have managed to yield ages for the Kutemajärvi area.

The most relevant age determinations that have been reported are the crystallization and deformation ages of the Pukala porphyry intrusion, the crystallization ages from monazite and zircon, derived from the chlorite-sericite schist, as well as the Pb-model age of a galena from the ore (Mänttäri et al. 1997, Talikka and Mänttäri 2005, Talikka, 2007). Nevertheless, the results of the prior isotopic studies refer to multigrain isotope age determinations for fractions of specific analyzed minerals and do not necessarily reflect the precise timing of ore formation. In addition, the majority of the samples, which were collected from the area of the deposit, represent a single rock type. As a result, a large number of samples, derived from different rock types of the hydrothermal alteration halo, needs to be dated, in order to reach a safe conclusion about the formation age of the gold deposit.

The primary goal of this Master's Thesis is to obtain single-grain U-Pb ages for monazite and zircon from the Kutemajärvi gold deposit by applying the Single Collector Laser Ablation Inductively Coupled Plasma Mass Spectrometry method (SC-LA-ICP-MS). The newly obtained ages, together with the results from previous geochronological studies, are applied to determine the timing of mineralization in the Kutemajärvi gold deposit and evaluate the spatial and temporal relationship between the ore and its host rocks, throughout the Late Paleoproterozoic of the Tampere Schist Belt.

2. Geological setting

2.1. Regional geology

The Svecofennian orogeny was a protracted tectonometamorphic event that affected large parts of Sweden and southwestern Finland, but it has also been recorded in the Central Lapland Greenstone Belt (e.g., Molnár et al. 2018), which constitutes one of the largest greenstone belts, spanning from northern Norway to Russian Karelia. The Svecofennian domain is an amalgamation of island arcs and ophiolites that have been accreted to the Archean Karelian craton between 2.0 Ga and 1.78 Ga (Lahtinen 2009, Kara et al. 2021). Based on structural, geochemical and geochronological criteria, it can be further divided into a primitive arc complex west of the Archean Karelian craton, the Central Svecofennian Arc Complex, and the Southern Svecofennian Arc Complex (Nironen, 1997, Korsman et al. 1999, Rämö et al. 2001, Väisänen et al. 2002, Saalmann

et al. 2009). Within the Central Svecofennian Arc Complex lies the Tampere Schist Belt, which hosts the Kutemajärvi gold deposit, near the town of Orivesi.

The east-west-striking Tampere Schist Belt (Figure 1) is a c. 200 km long volcano-sedimentary belt, located in the central part of the Paleoproterozoic Svecofennian domain in Southern Finland. In the north, the Tampere Schist Belt is bordered by the c. 1.88 Ga Central Finland Granitoid Complex (Kähkönen 1999, Nironen et al. 2000). To the south, lies the Vammala migmatite belt or Pirkkala Migmatite Domain, which is dominated by paragneisses and migmatites. Near Tampere, the contact between the Tampere Schist Belt and Vammala migmatite belt forms a curvilinear shear zone (Kalliomäki et al. 2014), whereas in the east, the contact is concealed by the c. 1.88–1.87 Ga Siitama batholith (Nironen et al. 2000).

The Tampere Schist Belt is composed of metavolcanics and turbiditic metasedimentary rocks (Kähkönen 1987, Kähkönen et al. 1989). Its central part constitutes a main east-west-striking syncline with subvertical planes that formed during the main folding phase (Kähkönen 1989, Nironen, 1989, Kähkönen 1999, Kähkönen, 2005). The northern limb is dominated by volcanic rocks, whereas in the southern limb sedimentary rocks predominate, although in the southernmost margin volcanic rocks become abundant (Kähkönen 1987, Kähkönen et al. 1989, Kähkönen 1999). The majority of the metavolcanics are pyroclastic rocks with minor lava flows and sills. Pillow lavas have only been reported in the Haveri Formation at Viljakkala. The chemical composition of the metavolcanics varies significantly, ranging from alkaline and calc-alkaline to tholeiitic rocks, with low-K to high-K or shoshonitic calc-alkaline being the most prevalent. In general, these metavolcanics display chemical features of modern continental or island-arcs. However, mafic rocks of the Haveri Formation exhibit E-MORB, non-arc type geochemical affinities, which are indicative of extensional settings (Kähkönen et al. 1989, Kähkönen and Nironen 1994, Kähkönen 1999). The metasedimentary rocks are mainly turbiditic greywackes, siltstones, and mudstones, deposited in a forearc basin and later metamorphosed to mica schists and slates. Near Mauri, fluvial-deltaic arkoses form a 2.5 km thick and 20–40 km long unit. Metamorphic conditions for the rocks of the Tampere Schist Belt have been defined as low-P, low-T amphibolite to transitional greenschist-amphibolite facies (Kilpeläinen et al. 1994). The metavolcanic rocks of the Tampere Schist Belt have yielded U-Pb zircon ages of 1.89–1.90 Ga (Kähkönen et al. 1989), while detrital zircons from greywackes are 1.9–2.0 Ga old and have an additional Archean component (Huhma et al. 1991, Lahtinen et al. 2009).

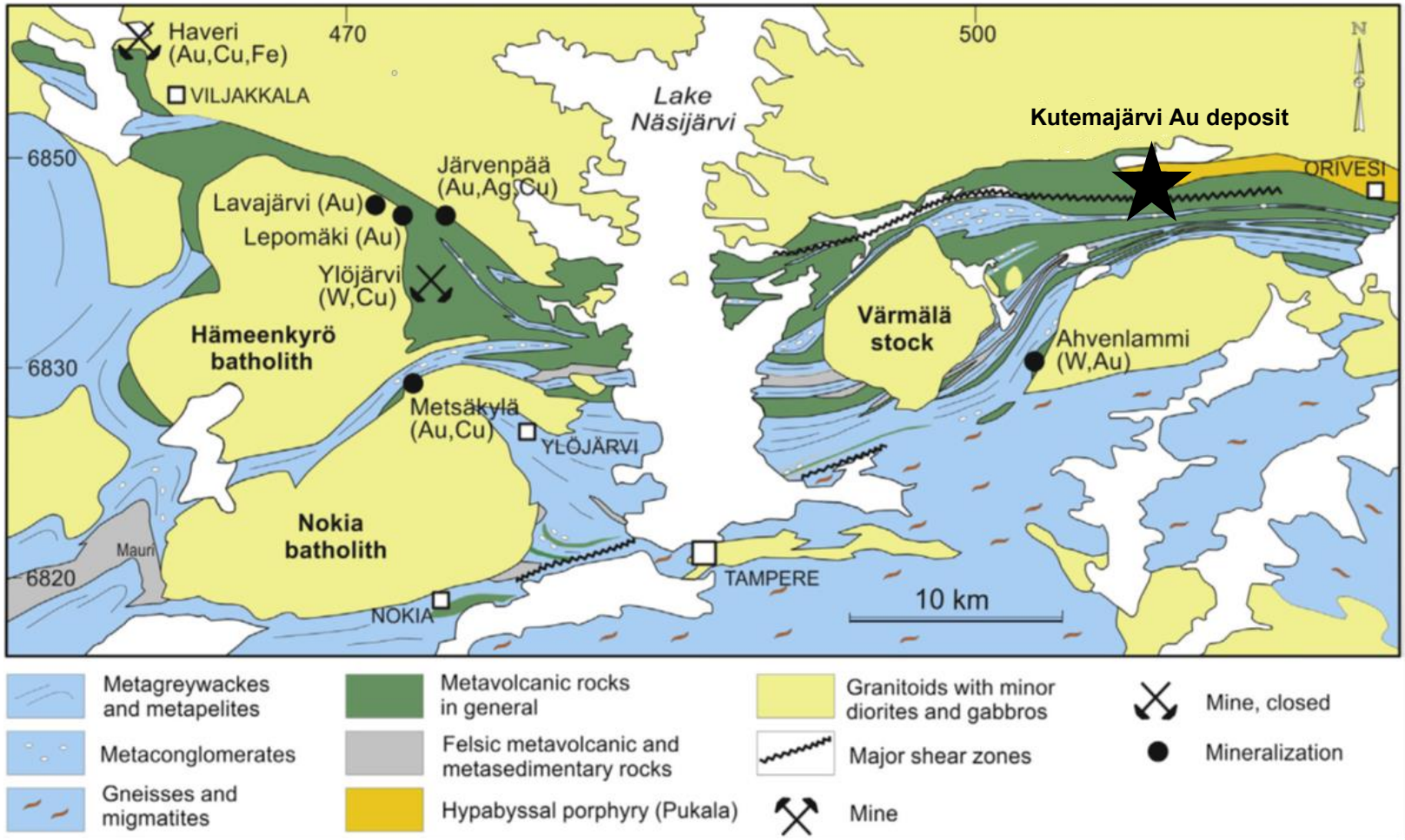

Figure.1. Geological map of the central Tampere Schist Belt showing locations of hydrothermal ore deposits and prospects associated with granitoids (modified after Haapala and Rämö 2015).

According to the generalized stratigraphic scheme of Simonen (1980), greywackes, siltstones, and mudstones comprise the lowermost formation and are overlain by quartz-feldspar rocks (arkoses, greywackes, and pyroclastics), mafic and intermediate volcanics, conglomerates and associated sedimentary rocks, and finally by mafic volcanics. Exceptions to the aforementioned scheme are the Haveri formation, which underlies the lowermost sediments, and the volcanic intercalations among the lowest greywackes near Lake Näsijärvi (Kähkönen et al. 1989).

A geotectonic model for the southeastern margin of the Tampere basin has been proposed by Kalliomäki et al. (2014), on the basis of field observations (Figure 2). According to the model, a siliciclastic unit is deposited in a continental-rift marginal basin at c. 1.92–1.90 Ga, on top of the rift-related Haveri-type volcanics. At c. 1.90–1.89 Ga subduction and arc-type volcanism commence, resulting in basin inversion and the creation of an intra-arc basin. During this event, some of the extensional faults were reactivated as reverse faults, causing folding of the volcanic and sedimentary rocks. Progressive closure of the basin causes the development of a southward-propagating thin-skinned thrust system that is layer-parallel to the siliciclastic unit and contributes to further shortening of the basin. Hydrothermal fluids originated from the deeper parts of the basin may have percolated along the thrust system. An opposite directed thrust develops at the southern margin of the Vammala basin. As shortening continues, the folds become tighter and the thrust faults are rotated into an upright position, leading to formation of schistosity (S_1) and entrapment of the sulfide mineralization. Sinistral strike-slip faults are likely to activate along the paleothrust planes, thereby inducing the formation of fractures that act as a trap for the secondary mineralization. Finally, the closure of the basin occurs at c. 1.88–1.87 Ga, marked by the intrusion of the Siitama batholith along the Tampere Shear Zone.

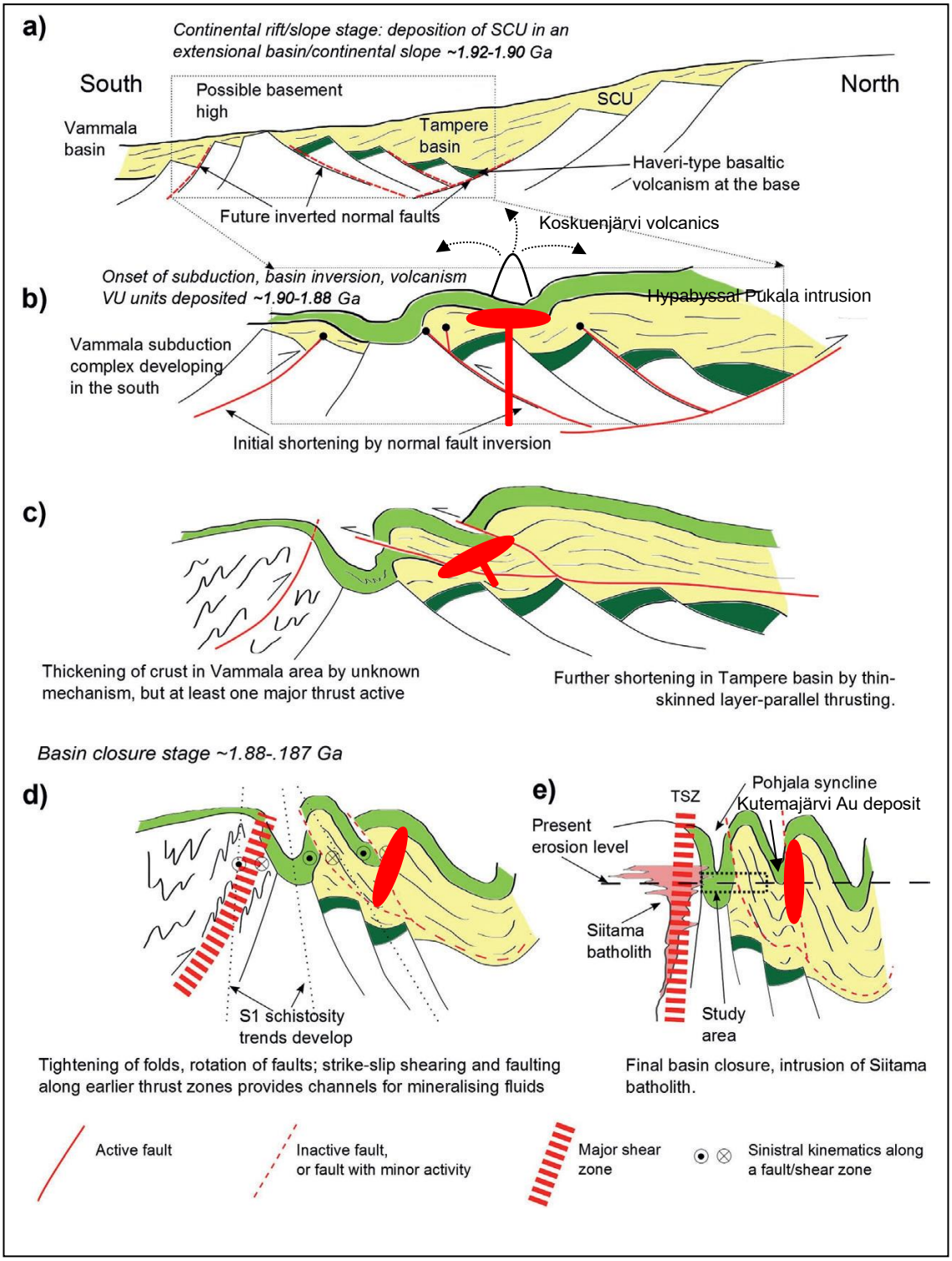

Figure 2. Conceptual tectonic model for the (southern) Tampere basin (modified after Kalliomäki et al. 2014).

2.2. Geology of the Kutemajärvi gold deposit

2.2.1. Host rocks

The metamorphosed Kutemajärvi gold deposit is hosted in the Koskuenjärvi formation, located in the lowermost part of the northern limb of a major east-west-striking synform. At Orivesi, the synform appears to be 1 km thick and extends up to 10 km. The Koskuenjärvi formation comprises primarily massive to stratified plagioclase-porphyritic high-K dacites and andesites and in which felsic volcanics relatively abound, whereas mafic volcanics are scarce. The volcanics of Koskuenjärvi formation are of pyroclastic origin, deposited in subaerial to shallow-water environments due to the prevalence of epidote-rich fragments and the paucity or absence of turbiditic intercalating sediments (Kähkönen 1999).

The Kutemajärvi deposit is located at the western edge of the Koskuenjärvi formation. The latter is further divided into two subunits: the unaltered southern subunit, comprised of intermediate volcanics, and the hydrothermally altered northern subunit, which includes pyroclastics, rhyolites, and minor intermediate volcanics (Figure 3). The two subunits are separated by a sharp contact, which does not appear to be tectonic. The lack of sedimentation and erosion in the transition zone, separating the two subunits, favors a subaerial environment for the deposition of the volcanic rocks. The sharp contact between the two subunits, in conjunction with the abrupt changes in the mineral content, denote that there is a slight difference in age between them. The hydrothermal alteration of the northern subunit precedes the emplacement of the unaltered subunit (Kinnunen 2008).

North of the alteration halo of the northern subunit lies the hypabyssal Pukala porphyry intrusion, which is 18 km long and 1–2 km wide. The major rock types of the intrusion are porphyritic granodiorite and trondhjemite with minor granitic, tonalitic, and aplitic parts (Kinnunen 2008). On the basis of the geochemical data, the Pukala intrusion displays characteristics of both I-and S-type granitoids and it was emplaced in an island-arc or fore-arc setting (Talikka and Mänttäri 2005).

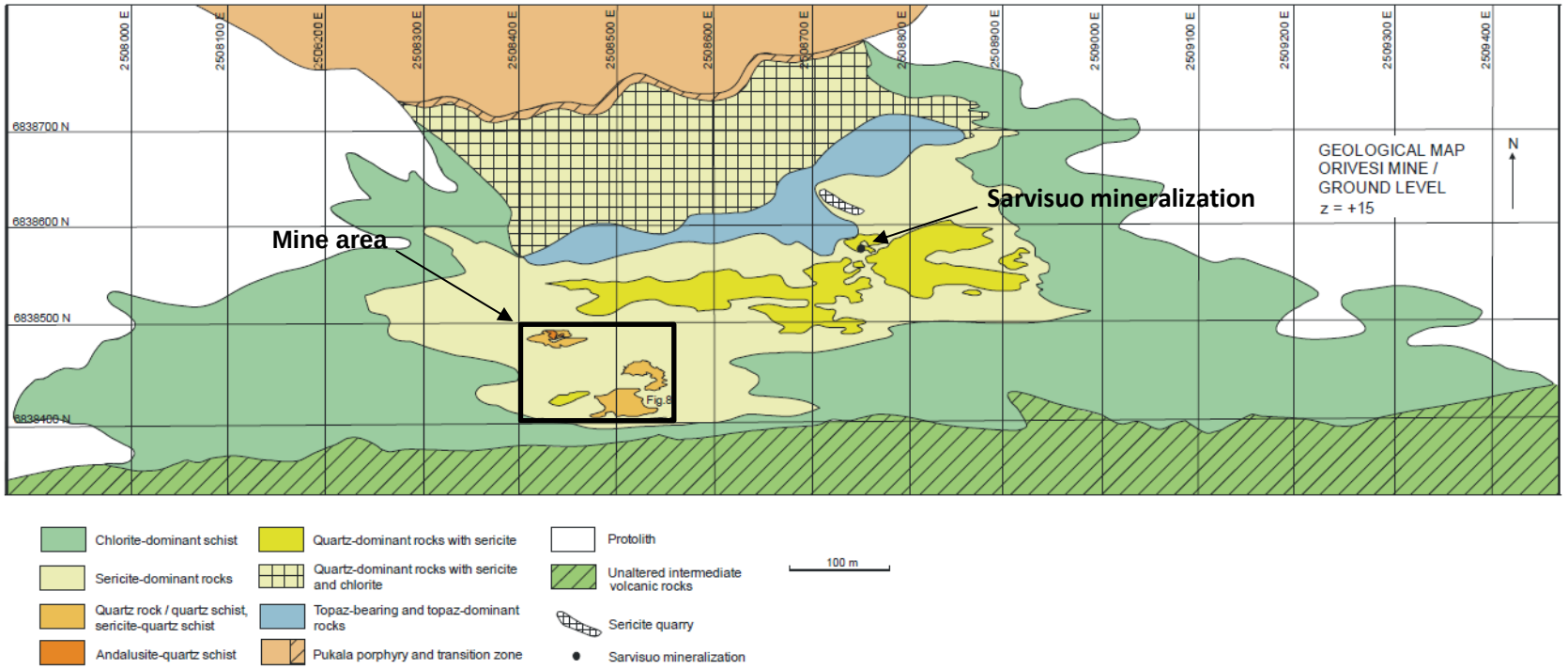

Figure 3. Geological map of the Kutemajärvi gold deposit and its surroundings (modified after Kinnunen 2008).

2.2.2. Alteration

The hydrothermally altered zone is surrounded on all sides by metavolcanics rocks. Signs of alteration increase gradually from east and west to the center of the zone as the content of associated minerals, such as chlorite, sericite, and pyrite increases. Apart from the features described, some locations are also characterized by the presence of quartz augens which mark the onset of silicification (Luukkonen 1994, Kinnunen 2008).

The alteration halo is divided into the following five rock types, which are named after their prevailing minerals: chlorite-dominant schists, sericite-dominant schists, topaz-bearing and topaz-dominant schists, andalusite-dominant schists, and quartz-dominant schists. Chlorite-dominant schists consist of chlorite, sericite, quartz, andalusite, and pyrite, whereas sericite replaces chlorite as the major mineral in the case of sericite-dominant schists. Quartz, topaz, sericite, and kaolinite are the main components of the topaz-bearing and topaz-dominant schists. The andalusite-dominant schists contain quartz, andalusite, sericite, telluride, gold, and pyrite, whereas the quartz-dominant schists are characterized by a similar mineral assemblage in which andalusite is absent (Kinnunen 2008).

The aforementioned rock types are distributed into three distinct alteration zones that have been preserved despite the deformation and metamorphism. The outer zone comprises chlorite-sericite±quartz schists with interlayers of magnetite-bearing amphibole schists that contain abundant andalusite and phlogopite with accessory amounts of rutile. In contrast, the intermediate and the inner alteration zones consist of sericite-quartz schists and quartz-rich rocks, respectively. The topaz-bearing and topaz-dominant rocks are included within the inner alteration zones. The majority of them are quartz schists in which topaz occurs as kaolinized spot-like fragments, whilst a small percentage is nearly monomineralic. The hosts of the vertical pipe-shaped ore bodies are quartz-andalusite-pyrophyllite rocks, which envelop the ore and entrain minor to trace amounts of topaz, fluorine, lazulite, kaolinite, rutile, apatite, tellurides and gold. (Luukkonen et al. 1992, Luukkonen 1994, Kinnunen 2008, Eilu 2015).

This zonal alteration pattern (Figure 4) clearly resembles the alteration sequence of the high-sulfidation epithermal deposits (Hedenquist et al. 2000, Sillitoe 2010). The quartz-dominant rocks are equivalent to vuggy quartz, which represents the silicic core of the epithermal system, surrounded by the proximal advanced argillic alteration (andalusite-dominant rocks, topaz-bearing, and topaz-dominant schists). Argillic alteration (sericite-

quartz schists) encloses the advanced argillic alteration, which in turn is succeeded by the distal propylitic alteration zone (chlorite-sericite schists) (Kinnunen 2008, Eilu 2015). The presence of topaz fragments in the both the advanced argillic and the argillic alterations is interpreted as the result of leaching that led to the collapse of the hydrothermal system (Kinnunen 2008).

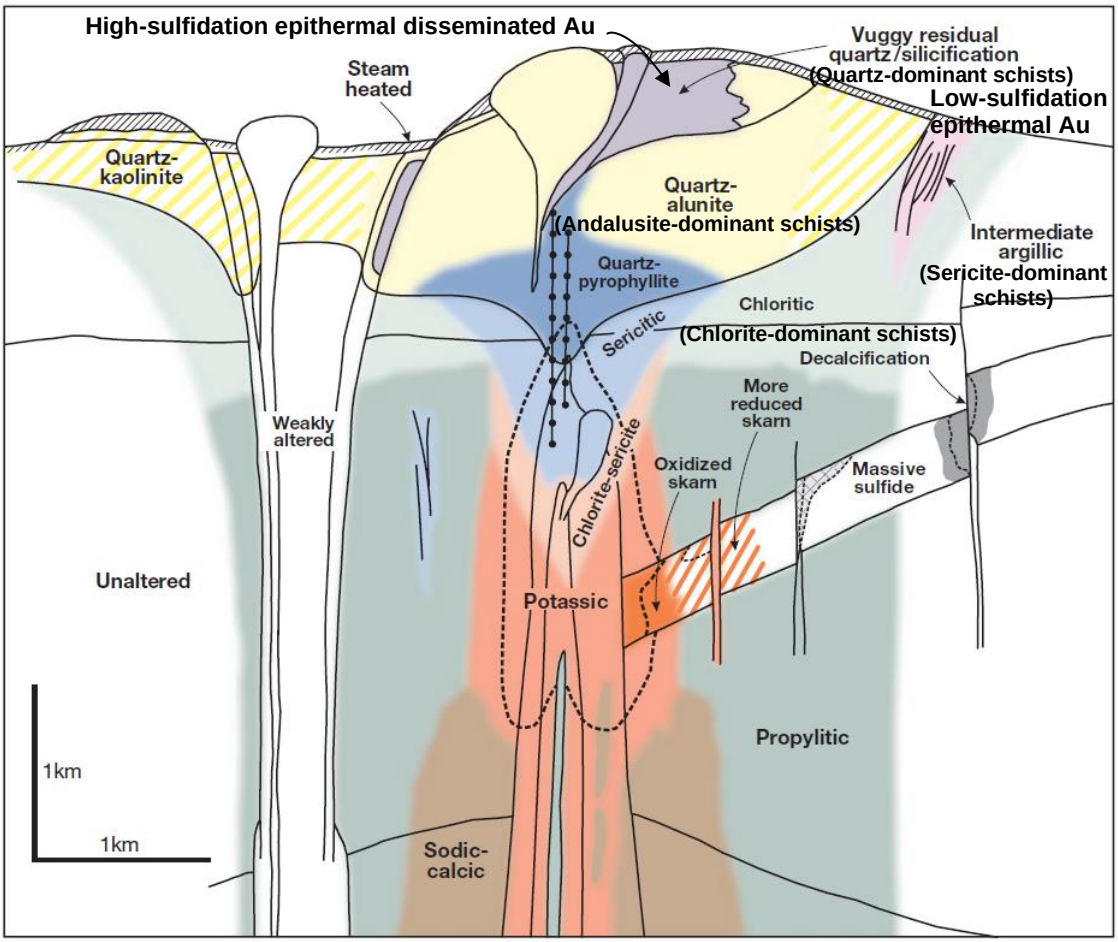

Figure 4. Generalized alteration-mineralization zoning pattern for telescoped porphyry Cu systems (modified after Sillitoe 2010).

2.2.3. Mineralization

The gold mineralization in Kutemajärvi is hosted by the sericite-quartz and quartz schists. The deposit consists of four distinct ore pipes (I–IV) in the hydrothermally altered domain (Poutiainen and Grönholm 1996) that are presented in Figure 5. Kinnunen (2008) reports the presence of a fifth pipe that constitutes the direct downward continuation of the fourth pipe. All pipes share a common volcanoclastic structure with deformed pyro-

clasts and only a minor variation in the percentage of the surrounding matrix. The shape of the ore pipes is lensoid (50–400 m^2) and they extend to more than 400 m below the surface. The only exception is Ore pipe II which occurs at c. 50 m below the surface (Poutiainen and Grönholm 1996, Kinnunen 2008).

Most of the gold of the mineralization occurs as native gold or it is carried by Au-Te tellurides and to a lesser extent by electrum and aurostibite. Native gold is usually fine-grained and almost half of the gold grains are inter-grown with tellurides. A significant proportion of gold grains is confined to gold tellurides, whereas the remaining gold occurs mainly along the boundaries of quartz grains or as inclusions in quartz and in later fractures. Sulfides and arsenides may also contain a small amount of native gold (Poutiainen and Grönholm 1996, Kinnunen 2008).

Tellurides and Te-Bi minerals are the most prominent mineral groups that occur in the ore pipes. Calaverite, montbrayite, kostovite, petzite, sylvanite, and hessite are the most common minerals of this category, along with tellurobismuthite, altaite, melonite, frohbergite, tsumoite, tetradymite, and rucklidgeite. In addition, lesser amounts of joseite, volynskite, tellurantimony, krennerite, and coloradoite have been identified (Luukkonen 1994, Kinnunen 2008). By contrast, sulfides are more commonly found in the alteration halo than in the ore, relative to the tellurides. The most prevalent sulfides are pyrite, chalcopyrite, pyrrhotite, galena, sphalerite, and arsenopyrite and the identified sulfosalts include boulangerite, tetrahedrite, bournonite, and meneghinite (Luukkonen 1994, Kinnunen 2008, Eilu 2015).

2.2.4. Previous isotopic studies of the Kutemajärvi gold deposit

Previous isotopic studies from the Tampere Schist Belt and the Kutemajärvi deposit have revealed variable ages, which are correlated to different events in the tectonometamorphic evolution of the area (Table 1). Kähkönen et al. (1989) have reported a 1904±4 Ma U-Pb age for the Koskuenjärvi formation, based on two zircon samples, derived from a massive stratum of dacitic crystal tuff and pyroclastic rhyolitic stratum. Furthermore, detrital zircons hosted by metasediments yield ages of 1.91–2.0 Ga (Huhma et al. 1991), while the U-Pb ages of the synorogenic granitoids are 1885±2 and 1878±3 Ma (Nironen 1989).

In the Kutemajärvi area, monazite and zircon from the chlorite-schist yield U-Pb ages of 1879±2 Ma and 1808±32 Ma, respectively. The Pb-Pb model age of a galena from the

chlorite-schist is 1888 Ma and is correlated to the culmination of the Svecofennian Orogen. The presence of galena in the chlorite-schist signifies that it was most likely crystallized by hydrothermal fluids, originated from a plutonic source. The same conclusion is drawn by the monazite crystallization age in the same rocks, while the zircon age is associated with later hydrothermal activity (Mänttäri et al. 1997). Isotopic studies have also been conducted in the case of the hypabyssal Pukala intrusion, which is located north of the alteration halo of the hydrothermally altered domain. According to U-Pb zircon dating from the granodiorite, the emplacement age of the intrusion is 1896±3 Ma, whereas the younger titanite age of 1851±5 Ma is interpreted to represent a subsequent local cooling after the peak metamorphism of the region (Talikka and Mänttäri 2005, Talikka 2007). Finally, Kinnunen (2008) has reported U-Pb ages of c. 1.5 Ga for an andalusite-muscovite breccia and c. 1.0 Ga for a muscovite-rich vein that reflect retrograde metamorphic events.

Table 1. Previous age determinations for the Kutemajärvi gold deposit.

Reference	Sample information	Age ± 2σ (Ma)	Comments
Kähkönen et al. (1989)	A385-Koskuenjärvi, Orivesi, rhyolite		analysis by SIMS
	zircon	1904 ± 4	concordia age
Mänttäri et al. (1997)	A1447-Kutemajärvi, Orivesi, chlorite schist		analysis by SIMS
	zircon	1808 ± 32	isochron age
	MON/HF	1850 ± 2	
	MON/abr.	1879 ± 2	
	A1447#1PbS	1889	model age
	A1447#2PbS	1893	model age
	A1447#3PbS	1883	model age
Talikka & Mänttäri (2005)	A1675 Pukala intrusion, granodiorite		analysis by SIMS
	zircon	1896 ± 3	concordia age
	titanite	1851 ± 5	concordia age
Kinnunen (2008)	Andalusite-muscovite breccia		analysis by SIMS
	Thucholite/brannerite	1500	isochron age
	Muscovite-rich vein/fracture fill		analysis by SIMS
	Thucolite/brannerite	1000	isochron age

3. Materials and methods

3.1. Sample material

The sample material consists of 149 polished thin sections from the Kutemajärvi gold deposit and the adjacent mineralization in Sarvisuo that is located northeast of the Orivesi mine. The sample material was provided by Mr. Matti Talikka and includes polished thin sections from rock types, which sprawl southeast of Lake Oriselkä up to Lake Ahvenlammi. The exact location and the rock type of the thin sections was determined by projecting them into the geological map (Figure 6). However, the coordinates for a number of thin sections were unknown. The thin sections are distributed into nine drill cores, but there is also a small number of individual thin sections that do not belong to any drill core. Samples for SEM analysis were selected on the basis of the optical microscopy results. Subsequently, those samples whose SEM analysis showed that contained sufficiently large monazite and zircon grains were used for U-Pb dating. Furthermore, U-Pb dating material includes hand-picked zircon grains of sample A1675 of Talikka and Mänttäri (2005), as well as zircon and monazite grains of sample A1447 of Mänttäri et al. (1997). A detailed catalog of samples that were utilized for each method is presented in the Results section and in the supplementary material.

3.2. Optical microscopy

Samples were examined using an optical microscope at the Department of Geosciences and Geography, University of Helsinki. All the drill core packages, and the individual polished thin sections were studied, in order to define detailed petrography for the host rocks of the Kutemajärvi gold deposit. Nevertheless, the petrographic analysis focused primarily on the identification of accessory minerals suitable for U-Pb age dating, such as zircon, monazite, and xenotime.

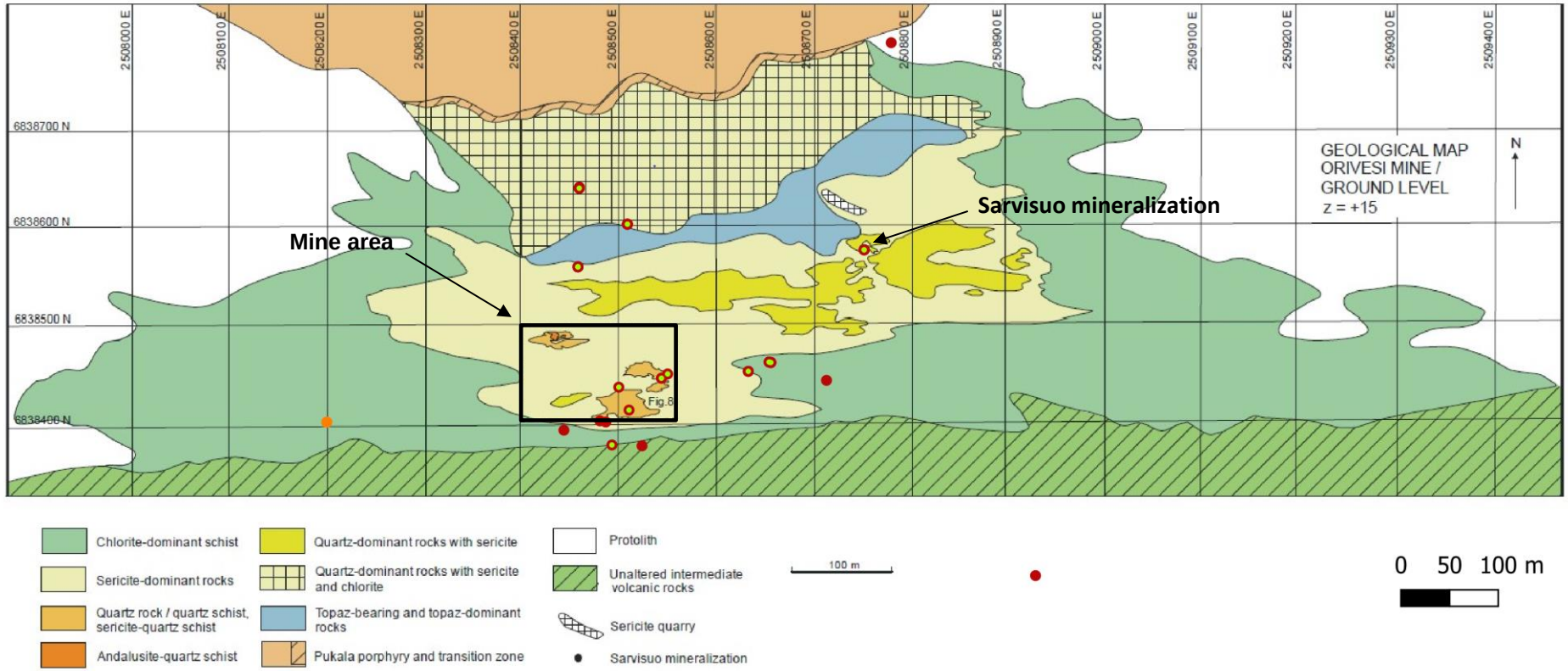

Figure 6. Geological map of the Kutemajärvi area. Scale 1:5000. The samples of this study are marked with red color, whereas the samples of Mänttäri et al. (1997) are depicted with orange color. The samples, marked with yellow color, were selected for SEM analysis (modified after Kinnunen 2008).

3.3. Scanning electron microscopy (SEM)

Scanning electron microscopy (SEM) analysis for accessory minerals was carried out at SEM Laboratory, Geological Survey of Finland, Espoo. Accessory mineral search in polished thin sections was performed using a Scanning Electron Microscope (SEM), model Hitachi SU3900 equipped with an electron dispersive X-ray spectrometer (EDS) X-Max 20 mm^2 (SDD) and INCA Feature phase detection-classification software (Oxford Instruments Ltd). The run conditions were: 20 kV acceleration voltage and 1 nA probe current. INCA Feature phase detection and classification software was used to scan zircon and monazite. The INCA Feature software performs automatic scans over the user-defined sample area and detects the grains using the backscattered electron (BSE) image (recording size, shape, and grey level). Subsequently, the mineral phases are analyzed and classified by chemistry and size using EDS software. The quality of the EDS analyses is semi quantitative and the results are normalized to 100%. The phase identification is based on the numerical elemental composition. The samples were manually analyzed and imagined using INCA Point ID software.

The objective of this technique is to identify accessory mineral phases, suitable for U-Pb dating and characteristic microtextures that may provide valuable information about the ore-forming processes in porphyry-epithermal systems and associated geological settings (Frelinger et al. 2015). These techniques permit high-resolution imaging of the inner structure of the crystals, in order to reveal their internal zonation and distinguish different genetic types. Moreover, high-quality cathodoluminescence (CL) images will assist in the selection of spots in zircon and monazite grains for the U-Pb geochronological analysis (Chen et al. 2015).

3.4. Single collector laser ablation inductively coupled plasma mass spectrometry (SC-LA-ICP-MS)

Zircon and monazite grains for U-Pb dating were selected by hand-picking from the delivered fractions A1447 and A1675. The grains were mounted in epoxy resin and sectioned approximately in half and polished. Back-scattered electron images (BSE) and cathodoluminescence (CL) images were prepared for the grains to target the spot analysis sites.

U-Pb isotope analyses were performed using a Nu Plasma AttoM single collector ICPMS at the Geological Survey of Finland in Espoo connected to a Photon Machine Excite laser ablation system. Samples were ablated in He gas (gas flows = 0.4 and 0.1 l/min) within a HelEx ablation cell (Müller et al. 2009). The He aerosol was mixed with Ar (gas flow= 0.96–0.98 l/min) prior to entry into the plasma. The gas mixture was being optimized daily for maximum sensitivity. Ablation conditions for monazite were as follows. Beam diameter: 15 μm, pulse frequency: 5 Hz, beam energy density: 2.17 J/cm^2. A single U-Pb measurement included a short pre-ablation with a 20 μm laser beam, 10 s of on-mass background measurement, followed by 30 s of ablation with a stationary beam. For zircon, the conditions were otherwise the same, except that the beam diameter was 20 μm and the pre-ablation beam size was 25 μm. ^{235}U was calculated from the signal at mass 238 using a natural ^{238}U/^{235}U=137.88. Mass number 204 was used as a monitor for common ^{204}Pb. The contribution of ^{204}Hg from the plasma was eliminated by on-mass background measurement prior to each analysis. Age-related common lead (Stacey and Kramers 1975) correction was used when the analysis showed common lead contents significantly above the detection limit (i.e., >60 cps). Signal strengths on mass 206 were typically >200000 cps, depending on the uranium content and age of the monazite and zircon.

For zircon, the calibration standard GJ-1 (609 ± 1 Ma, Belousova et al. 2006), and in-house reference samples A382 (1877±2 Ma, Huhma et al. 2012), and A1772 (2712±2 Ma, Huhma et al. 2012) were used. For monazite, in-house reference sample A276 (1915±3 Ma, unpublished) was used as calibration standard and A49 (1874 ± 3 Ma, Salli 1983) and A1326 (2630±2 Ma, Hölttä et al. 2000) were used as reference samples. A block containing these references were run at the beginning and end of each analytical session, and at regular intervals during sessions. Raw data were corrected for the background, laser induced elemental fractionation, mass discrimination, and drift in ion counter gains and reduced to U-Pb isotope ratios by calibration to concordant reference zircons, using the program Glitter (Van Achterberg et al. 2001). Further data reduction including common lead correction and error propagation was performed using excel spreadsheet written by Y. Lahaye and H. O'Brien. Errors include measured within-run errors (SD) and quadratic addition of reproducibility of standard (SE). Estimated errors in the calibration standards were: 0.2% for ^{207}Pb/^{206}Pb, and 2% for both ^{206}Pb/^{238}U and ^{207}Pb/^{235}U. To minimize the effects of laser-induced elemental fractionation, the depth-to-diameter ratio of the ablation pit was kept low, and isotopically homogeneous segments of the time-

resolved traces were calibrated against the corresponding time interval for each mass in the reference zircon. Plotting of the U-Pb isotopic data and age calculations were performed using the Isoplot/Ex 3 program (Ludwig 2003). All the ages were calculated with 2σ errors and without decay constants errors. Data-point error ellipses in the figures are at the 2σ level.

4. Results

4.1. Petrography

4.1.1. Optical Petrography

The results of the petrographic analysis are presented in Table 1. Most of the samples represent drill core 31-0-1 KOH that mainly intersects the sericite-dominant schists. Quartz, sericite, and phlogopite predominate and the chlorite content increases with increasing depth. Samples originating from shallow levels also include kaolinite as an accessory mineral. At a certain depth, chlorite supersedes phlogopite as a main mineral; the latter remains as an accessory mineral, and it appears again as a main mineral at greater depth. Epidote is the most common accessory mineral, along with fluorite and partially tourmaline. Opaque minerals are ubiquitous as accessory minerals in both drill cores. In the 31-0-1 KOH-19 thin section that lies at the bottom of the drill core, carbonates and plagioclase are among the prominent components. Some thin sections contain zircon crystals, enclosed in phlogopite. The thin sections which originate from the 31-0-2 KOH drill core correspond to the quartz-dominant schists with sericite and chlorite. The main recognized minerals are quartz, phlogopite, sericite and kaolinite. Andalusite, chlorite, and epidote are present as either main or accessory minerals, whereas zircon crystals are enclosed by phlogopite grains.

Thin sections of the KU-021 drill core are obtained from the boundary of the quartz-dominant schists with sericite and chlorite, and the topaz-bearing and topaz-dominant rocks. Their mineralogy is similar to those from 31-0-2 drill core, but the former contain pyrophyllite and topaz as main and accessory minerals, respectively. KU-022 drill core originates from the same rock type as 31-0-1 and 31-0-2 drill cores, but contrary to the latter, muscovite coexists with sericite and pyrophyllite constitutes an accessory mineral.

Two of the largest groups of the sample material, namely those from KU-567 and KU-568 drill cores, account for the chlorite-dominant schists. The main minerals include quartz, sericite or muscovite, chlorite, epidote, phlogopite, and usually pyrophyllite and andalusite. Fluorite, zircon, monazite, hematite, and opaque minerals are the typical accessory minerals. A slight difference in mineralogy between the two aforementioned cores and KU-569, which is obtained from the sericite-dominant and chlorite-dominant schists boundary, is manifested by the accessory amounts of chlorite.

Drill core ORV/KU has been drilled in the mine area, proximal to the ore pipes 1 and 3. Sample ORV/KU-559 99-26127 is projected within the pipe 1 and consists of quartz, pyrophyllite and andalusite with minor muscovite, diaspore, rutile, and opaque minerals. Sample ORV/KU-543 anro 99-25453 is located at the boundary of the quartz-rocks/quartz-schists, sericite-quartz schists, and the sericite-dominant schists and as a result it contains sericite as a main mineral and kaolinite in addition to pyrophyllite. Two more samples from the same core exhibit only quartz and sericite.

Samples from the Sarvisuo mineralization (Figure 4) are quartz-dominant schists with sericite in which quartz, pyrophyllite, kaolinite and andalusite are the dominant minerals, whilst rutile, hematite, zircon, and opaque minerals exist in accessory amounts. Finally, the majority of the individual thin sections correspond to the hypabyssal Pukala porphyry intrusion, as well as to mafic and intermediate metavolcanic rocks.

Table 1. Results of optical petrography. The thin sections that were selected for SEM analysis are marked with red color.

Thin section	Depth (m)	Main minerals	Accessory minerals
31-0-1 KOH-1	5.30	quartz, muscovite	opaque, sericite, kaolinite, phlogopite
31-0-1 KOH-2	6.15	quartz, phlogopite, sericite	kaolinite, opaque
31-0-1 KOH-3	8.90	quartz, phlogopite, sericite	kaolinite, opaque
31-0-1 KOH-4	11.45	quartz, sericite, phlogopite	kaolinite, opaque
31-0-1 KOH-5	17.95	quartz, sericite, phlogopite	epidote, opaque
31-0-1 KOH-6	18.80	quartz, sericite	phlogopite, hematite, opaque, zircon
31-0-1 KOH-7	58.00	quartz, chlorite, sericite, phlogopite	zircon, opaque
31-0-1 KOH-8	79.60	quartz, sericite, chlorite	opaque
31-0-1 KOH-8	85.00	quartz, chlorite, sericite	opaque, tourmaline, epidote
31-0-1 KOH-8	85.30	quartz, chlorite, sericite	opaque, tourmaline
31-0-1 KOH-8	85.80	quartz, sericite, chlorite	opaque, epidote
31-0-1 KOH-8	89.60	quartz, sericite, chlorite	opaque, fluorite, phlogopite, hematite, epidote
31-0-1 KOH-8	90.70	quartz, sericite	chlorite, opaque, fluorite, epidote
31-0-1 KOH-8	91.10	quartz, chlorite, sericite	opaque, phlogopite, epidote
31-0-1 KOH-8	93.60	quartz, sericite, chlorite, phlogopite	opaque, fluorite, epidote
31-0-1 KOH-8	94.80	quartz, chlorite, sericite	opaque, tourmaline, fluorite
31-0-1 KOH-8	95.20	quartz, sericite, chlorite	opaque, fluorite, tourmaline, epidote
31-0-1 KOH-9	98.20	quartz	sericite, phlogopite
31-0-1 KOH-10	116.70	quartz, sericite, phlogopite, plagioclase	opaque, zircon
31-0-1 KOH-11	123.75	biotite, epidote, quartz	opaque, chlorite
31-0-1 KOH-12	126.25	quartz, sericite, phlogopite	opaque, kaolinite
31-0-1 KOH-13	131.70	quartz, sericite, phlogopite	opaque, epidote
31-0-1 KOH-14	143.80	quartz, sericite	kaolinite, fluorite
31-0-1 KOH-14	144.50	quartz, sericite	fluorite, hematite
31-0-1 KOH-14	145.50	quartz, sericite	opaque
31-0-1 KOH-15	146.20	quartz, phlogopite, andalusite	opaque, hematite, sericite
31-0-1 KOH-15	146.50	quartz, sericite	epidote, fluorite, chlorite

31-0-1 KOH-15	148.20	quartz, sericite	chlorite, epidote
31-0-1 KOH-15	149.30	quartz, sericite	epidote, kaolinite, fluorite
31-0-1 KOH-15	149.50	quartz, sericite, phlogopite	opaque, chlorite, fluorite, kaolinite
31-0-1 KOH-16	154.35	quartz, sericite, muscovite, opaque, phlogopite	hematite, fluorite
31-0-1 KOH-17	163.00	quartz, sericite, phlogopite	fluorite, hematite, opaque, epidote
31-0-1 KOH-18	166.00	quartz	chlorite, muscovite, fluorite, opaque, epidote
31-0-1 KOH-19	213.00	quartz, chlorite, sericite, plagioclase, carbonates	epidote, opaque, titanite
31-0-2 KOH-20x	3.50	quartz, sericite, phlogopite	andalusite, chlorite, biotite, fluorite, zircon
31-0-2 KOH-21x	9.80	quartz, sericite, phlogopite, andalusite, kaolinite	chlorite
31-0-2 KOH-22x	21.00	quartz, sericite, phlogopite, kaolinite	chlorite, zircon, epidote, opaque
31-0-2 KOH-23x	28.15	Sericite, quartz, phlogopite	zircon, andalusite, opaque
31-0-2 KOH-24x	35.70	andalusite, biotite, kaolinite, quartz, sericite	zircons, phlogopite, epidote
31-0-2 KOH-25x	48.30	sericite, kaolinite, quartz	fluorite, zircon
31-0-2 KOH-26x	81.00	quartz, sericite, phlogopite, kaolinite	zircon, andalusite, opaque, fluorite, hematite
31-0-2 KOH-27x	83.45	quartz, sericite, andalusite, kaolinite	phlogopite, hematite
31-0-2 KOH-28x	88.10	phlogopite, quartz, kaolinite, andalusite	sericite
31-0-2 KOH-29x	96.50	phlogopite, quartz, kaolinite	sericite, andalusite
KU 021-3		quartz, sericite, phlogopite	opaque, hematite
KU 021-4B		kaolinite, epidote, opaque, hematite	quartz, sericite, phlogopite, rutile
KU 021-6A		quartz, kaolinite, phlogopite, sericite	chlorite, opaque, hematite, rutile
KU 021-6B		quartz, sericite, phlogopite	kaolinite, opaque, hematite, rutile
KU 021-7		quartz, sericite	opaque, kaolinite
KU 021-11		quartz, sericite, phlogopite, kaolinite	opaque, hematite
KU 021-12		quartz, sericite	opaque
KU 021-13		quartz, sericite	opaque, kaolinite
KU 021-14B		quartz, sericite, pyrophyllite, kaolinite, epidote, andalusite	opaque, hematite
KU 021-15B		quartz, phlogopite, chlorite	opaque, hematite
KU 021-17		quartz, sericite, kaolinite	opaque, hematite
KU 021-18		quartz, pyrophyllite, muscovite/sericite, phlogopite	opaque, hematite

KU 021-19		quartz, hematite, sericite, phlogopite	opaque, rutile
KU 021-20A		quartz, pyrophyllite, muscovite/sericite	opaque
KU 021-21		quartz, sericite	zircon
KU 022-2		quartz, sericite, phlogopite, chlorite	opaque
KU 022-III		phlogopite, opaque, hematite, pyrophyllite	-
KU 022-5B		phlogopite, muscovite/sericite, kaolinite	hematite, opaque
KU 022-6		muscovite/sericite, chlorite, kaolinite	opaque, hematite, rutile
KU 022-7		quartz, phlogopite	-
KU 022-9		quartz, sericite	opaque, hematite
KU 149-2		quartz, phlogopite, muscovite, plagioclase, epidote, alk. fs., kaolinite	opaque
KU 174-1		quartz, chlorite, sericite, kaolinite, carbonates	opaque
KU 182-1		quartz, phlogopite, sericite, hematite, chlorite, kaolinite	opaque
KU 208		quartz, phlogopite, plagioclase, chlorite, kaolinite	opaque, hematite, rutile
KU 212-1B		chlorite, phlogopite, quartz	opaque, zircon, rutile
KU-567	27.00	quartz, sericite, biotite, phlogopite, chlorite, kaolinite	opaque, zircon, andalusite
KU-567	34.20	quartz, phlogopite, epidote, chlorite, kaolinite	opaque, rutile
KU-567	132.50	quartz, kaolinite, sericite	opaque
KU-567	202.40	andalusite, kaolinite, pyrophyllite	hematite, opaque
KU-567	231.40	quartz, sericite, kaolinite, pyrophyllite, andalusite	opaque
KU-567	232.80	quartz, muscovite, kaolinite	opaque
KU-567	243.20	quartz, sericite/muscovite, phlogopite, andalusite	opaque, zircon, monazite
KU-567	261.80	quartz, sericite, andalusite, kaolinite	opaque
KU-567	264.70	quartz, muscovite	opaque, rutile
KU-567	282.20	quartz, sericite, andalusite	opaque
KU-567	338.50	quartz, sericite/muscovite, pyrophyllite, kaolinite, andalusite	opaque
KU-567	382.70	quartz, sericite/muscovite, phlogopite, plagioclase	opaque, zircon, rutile
KU-567	397.80	quartz, sericite, phlogopite	opaque, zircon, rutile
KU-568	59.80	quartz, sericite, kaolinite, pyrophyllite	opaque, monazite
KU-568	78.80	quartz, epidote, andalusite	opaque

KU-568	201.40	quartz, sericite/muscovite, andalusite, pyrophyllite, kaolinite	opaque
KU-568	209.30	quartz, andalusite, muscovite, kaolinite	opaque
KU-568	236.40	quartz, sericite/muscovite, kaolinite	opaque, rutile
KU-568	291.20	quartz, muscovite/sericite, phlogopite, andalusite	opaque, kaolinite
KU-568	295.50	quartz, sericite, andalusite, kaolinite	opaque
KU-568	399.05	quartz, sericite, phlogopite, chlorite	opaque, monazite, apatite
KU-568	403.90	quartz, phlogopite, sericite, plagioclase, kaolinite	opaque, chlorite, fluorite
KU-569	308.80	quartz, phlogopite, sericite	opaque, chlorite, monazite
KU-569	394.40	quartz, sericite, kaolinite, phlogopite, plagioclase	opaque
KU-569	397.50	quartz, phlogopite, plagioclase, sericite, kaolinite	opaque
KU-741	476.65	quartz, biotite, phlogopite, chlorite, andalusite	zircon
KU-797 GRA	16.8	quartz, sericite, phlogopite, biotite, chlorite, andalusite, kaolinite	opaque, hematite, zircon
2128001		quartz, phlogopite, plagioclase, kaolinite	hematite
2128002		quartz, alk. fs./plagioclase, phlogopite/biotite, epidote, chlorite	opaque, fluorite
2128003		quartz, epidote, phlogopite, plagioclase, kaolinite	hematite
2128004		quartz, plagioclase, phlogopite, kaolinite, epidote	zircon
2128005		quartz, plagioclase, phlogopite, kaolinite, epidote	opaque, fluorite, hematite
2128006		quartz, plagioclase, kaolinite, phlogopite	chlorite, epidote
2128007		epidote, quartz, biotite	hematite
2128008		quartz, biotite, plagioclase, kaolinite, chlorite	epidote, opaque, hematite
2128009		quartz, biotite, kaolinite, chlorite	hematite
2128010		quartz, plagioclase, phlogopite/biotite, kaolinite, chlorite	opaque, epidote
ORV/KU-453	46.90	quartz, sericite/muscovite	-
ORV/KU-543 anro 99-25453	36.75	quartz, sericite, kaolinite, andalusite, pyrophyllite, apatite	opaque
ORV/KU-559 99-26125	43.00	quartz, sericite	opaque
ORV/KU-559 99-26127	46.10	quartz, pyrophyllite, andalusite	muscovite, diaspore, opaque, rutile
ORVKU-582 99-26237	66.00	quartz, sericite	-
Sarvisuo IA		quartz, pyrophyllite, kaolinite, andalusite	opaque, rutile, hematite
Sarvisuo IB		quartz, pyrophyllite, andalusite, kaolinite	opaque

Sarvisuo IC		quartz, pyrophyllite, andalusite, kaolinite	opaque, hematite
Sarvisuo IIA		quartz, kaolinite, pyrophyllite, andalusite	opaque, zircon
Sarvisuo IIB		quartz, pyrophyllite, kaolinite, andalusite	opaque, muscovite, hematite
Sarvisuo IIC		quartz, kaolinite, pyrophyllite, andalusite	opaque, hematite
Sarvisuo IIIA		quartz, kaolinite, pyrophyllite, andalusite	opaque
Sarvisuo IIIB		quartz, pyrophyllite, kaolinite, andalusite	opaque
Sarvisuo IIIC		quartz, kaolinite, pyrophyllite, andalusite	opaque
+470 Lp3 672	35.20	quartz, sericite/muscovite	opaque, rutile
+490 Lp51 696	2-10	pyrophyllite, diaspore, andalusite, apatite	-
+490 Lp51, 696	2-10	sericite, kaolinite, muscovite	apatite, opaque
PU-5A		quartz, kaolinite, plagioclase, biotite, epidote	opaque, hematite, zircon
PU-5B		quartz, biotite, epidote	opaque, hematite, chlorite
PU-6		quartz, kaolinite, chlorite	opaque, zircon, epidote
PU-14		quartz, plagioclase, biotite, kaolinite	opaque, epidote, rutile, zircon
PU-15		quartz, biotite, plagioclase, epidote, kaolinite	opaque, hematite, chlorite
PU-18		quartz, plagioclase, biotite, chlorite	hematite, opaque, zircon
MTT-244-02		quartz, biotite, plagioclase, chlorite, epidote	opaque, zircon, fluorite
MTT-250-02		quartz, kaolinite, epidote, chlorite	opaque, rutile, zircon
MTT-255-02		quartz, biotite, plagioclase	opaque, rutile, chlorite
220		quartz, plagioclase, phlogopite	epidote, chlorite, zircon
229		quartz, biotite, kaolinite, plagioclase	chlorite, opaque, zircon
335		quartz, kaolinite, plagioclase, chlorite, biotite	opaque, zircon, rutile
349		quartz, biotite, kaolinite, plagioclase	chlorite, zircon
409		quartz, biotite, plagioclase, sericite	opaque, chlorite, zircon
441		quartz, plagioclase, kaolinite, phlogopite, muscovite	opaque
Tutk.oja "Transition zone"		quartz, biotite, plagioclase, kaolinite, chlorite	opaque, zircon
Pukalan porfyyri		quartz, biotite, plagioclase, kaolinite, sericite	opaque, zircon, chlorite
RATA		quartz, epidote, plagioclase, kaolinite, chlorite	opaque, phlogopite, zircon
K1A		quartz, chlorite, plagioclase, kaolinite	opaque, zircon, hematite

K1B	quartz, biotite/phlogopite, chlorite, plagioclase, kaolinite	opaque, zircon
98 31770	opaque, quartz, muscovite	-
98 31764	quartz, sericite, chlorite	phlogopite, fluorite, epidote
98 31768	opaque, quartz, muscovite, sericite	hematite, kaolinite
98 31782	quartz, epidote, chlorite	-
N. COMBLAYER	quartz, sericite, kaolinite, plagioclase, chlorite	hematite

4.1.2. SEM mineral identification and mapping

The results of SEM mineral identification and mapping revealed ample monazite and zircon grains that are presented in Table 2. Monazite grains were detected in 12 thin sections that are divided into two categories based on their textural setting (Table 3). The first category includes metamorphic grains, which display strain shadow around them, in such a way that the background minerals that comprise the main foliation appear to be rotated and the created gaps across the rotation axis of the grains are filled by quartz, sericite, biotite, and chlorite (Figure 7A). The second type involves hydrothermal grains that are characterized by a markedly large number of inclusions either in the interior or in the rim (Figure 7B). Metamorphic monazite may also exhibit a small number of inclusions that are less rounded compared to the hydrothermal monazite. In sample KU-569 308.80 one grain was falsely detected as xenotime, but the lack of Y and the presence of La, Ce, and Nd point towards a monazite composition. This monazite crystal belongs to both types, given that it displays both strain shadow and inclusions, and its corroded part has been filled by a different crystal, possibly zircon (Figure 7C). The only xenotime crystal was detected in the same sample and it is inferred to be of hydrothermal origin on the grounds that it is highly corroded and hosts inclusions. Zonation in monazite was generally absent, but where observed, such as in sample ORV KU-582, it was subtle.

The majority of zircon grains, which were detected in 14 thin sections, are homogeneous or exhibit subtle zonation and therefore their classification is somewhat problematic. However, where it was possible, they were also divided to magmatic, metamorphic, and hydrothermal zircon. Metamorphic zircon is characterized by the presence of a strain shadow, similarly to metamorphic monazite, and may be polycrystalline with recrystallized parts that alter the primary internal structure (Figure 7D), whereas magmatic zircon is euhedral to subhedral and show characteristic concentric oscillatory zonation (Figure 7E). Hydrothermal zircon is usually anhedral and corroded with inclusions either in the core or in the rim (Figure 7F). Overall, the classification criteria are to some extent equivocal, as some grains demonstrate multiple features, whilst others cannot be easily subsumed in one of the aforementioned categories. Thus, more detailed microtectonic and chemical composition analyses are required to determine the textural nature of zircon, monazite and xenotime.

Table 2. Results of SEM mineral identification and mapping.

Thin section	Depth	Number of monazite grains	Number of zircon grains	Number of xenotime grains
31-0-1 KOH-8	95.20	16	2	-
31-0-1 KOH-15	146.20	3	2	-
31-0-2 KOH-24x	35.70	15	1	-
KU 021-6A	-	1	6	-
KU-174	-	-	6	-
KU-567	243.20	13	4	-
KU-568	59.80	10	29	-
KU-568	399.05	-	5	-
KU-569	308.80	4	2	1
ORV/KU-453	46.90	-	10	-
ORV/KU-543 anro 99-25453	36.75	9	3	-
ORV/KU-582 99-26237	66.00	7	1	-
ORV/KU-559 99-26127	46.10	3	4	-
Sarvisuo IA	-	7	-	-
Sarvisuo IIA	-	40	1	-

Table 3. Classification of monazite grains based on textural setting.

Thin section	Depth	Number of strain shadow type (metamorphic) monazite grains	Number of spongy type (hydrothermal) monazite grains	Number of monazite grains belonging to both types	Number of monazite grains for which textural setting type is ambiguous
31-0-1 KOH-8	95.20	3	7	3	3
31-0-1 KOH-15	146.20	-	-	-	3
31-0-2 KOH-24x	35.70	-	4	-	11
KU 021-6A	-	-	-	-	1
KU-174	-	-	-	-	-
KU-567	243.20	2	4	1	6
KU-568	59.80	1	4	-	5
KU-568	399.05	-	-	-	-
KU-569	308.80	1	1	2	-
ORV/KU-453	46.90	-	-	-	-
ORV/KU-543 anro 99-25453	36.75	-	8	-	1
ORV/KU-582 99-26237	66.00	-	7	-	-
ORV/KU-559 99-26127	46.10	-	3	-	-
Sarvisuo IA	-	-	4	1	2
Sarvisuo IIA	-	-	30	-	10

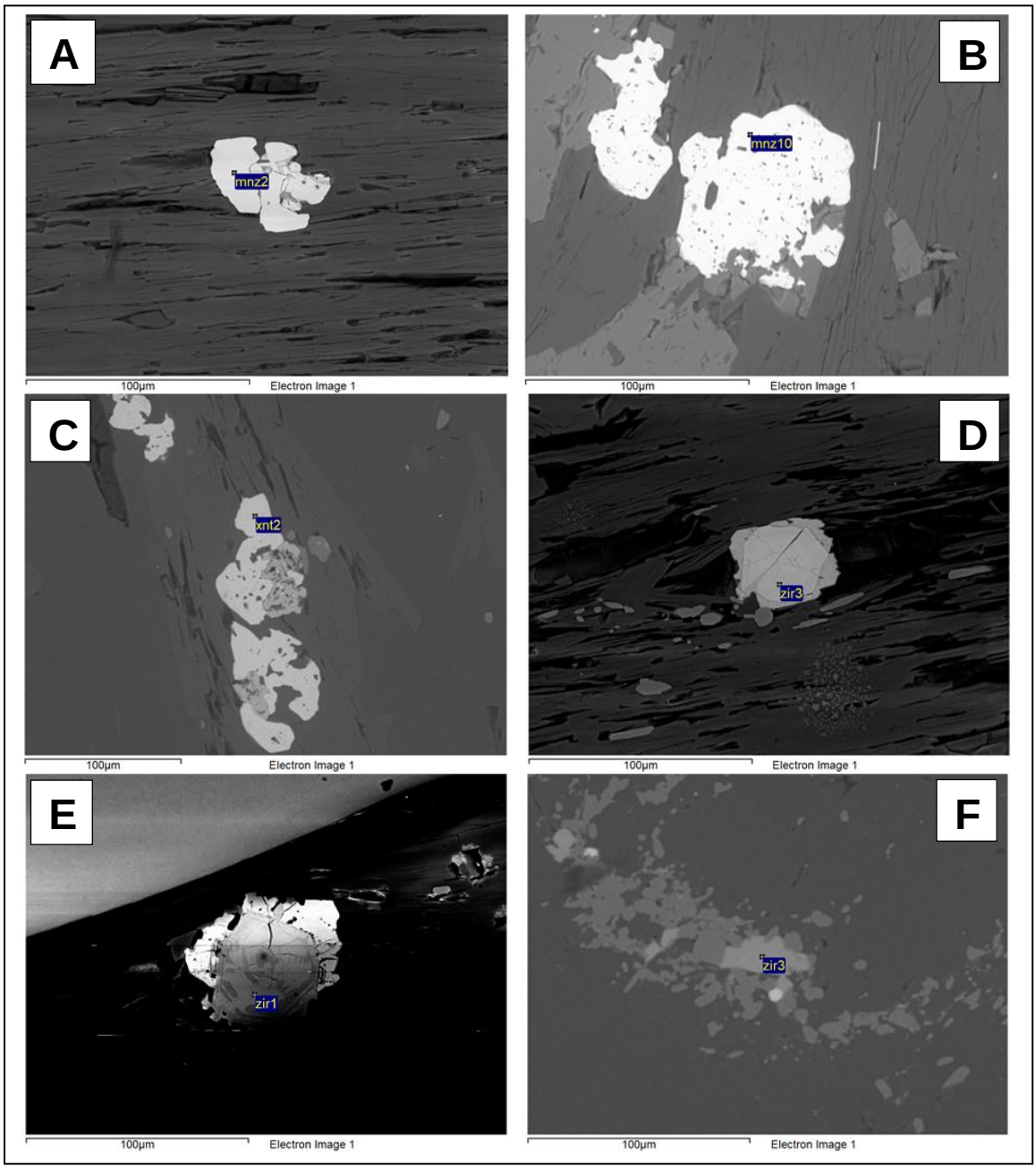

Figure 7. SEM-BSE images of the textural settings and types of monazite and zircon grains. A – Strain shadow type metamorphic monazite from the chlorite-dominant schist sample KU-568 59.80. B – Spongy type hydrothermal monazite grain from the sericite-dominant schist KOH-8 95.20. C – A monazite grain from sample KU-569 308.80, at the contact between sericite-dominant and chlorite-dominant schists, exhibiting characteristics of both types. The main foliation appears to be diverted and a secondary mineral has filled parts of the corroded surfaces of the monazite grain. D – A metamorphic zircon from the chlorite-dominant schist sample KU-568 59.80 with a rim filled by a secondary mineral. E – A magmatic zircon from the chlorite-schist sample KU-568 59.80, displaying subtle oscillatory zonation, around which a hydrothermal monazite grain has been deposited. F – An anhedral hydrothermal zircon grain from the quartz schist sample ORV KU-559 of the Kutemajärvi gold deposit.

4.2. Isotope dating

The results of U-Pb dating of monazite and zircon are listed in the supplementary material. The majority of the results are concordant, but there are also some discordant results, which produce inconsistent age data, and thus, they were not considered for further evaluation. Albeit plethora of zircons were identified during SEM analysis, only four thin sections contained grains whose size was appropriate for U-Pb dating. Monazite grains can be divided to one or two populations on the basis of the U-Pb concordia diagrams, as well as of the textural and mineralogical settings. Similar observations can be made with respect to zircon despite the lower number of dated grains. In both cases, the results are most coherent where a large number of grains has been analyzed. Furthermore, the concordia diagrams of the samples were compared to the $^{207}Pb/^{206}Pb$ ages of individual grains. The $^{207}Pb/^{206}Pb$ ages of the analyzed grains of each sample, as well as of the ready-picked analyzed grains of the samples A1675 and A1447, are included in the supplementary material. These ages were filtered, according to the procedure described in the following section, to ensure that only the most meaningful results would be utilized to draw conclusions about the tectonometamorphic history of the region. Finally, U-Pb dating results are presented for each sample separately with a short description and photos of the textural setting of the individual grains.

Sample 31-0-1 KOH-8 95.20

Sample 31-0-1 KOH-8 95.20 contains 16 monazite grains and 2 zircon grains in total. Three monazite grains exhibit characteristics of both types (Figure 8A). Strain shadow type monazite is represented by 3 grains (Figure 8B), whilst 7 monazite grains belong to the spongy type (Figure 8C). The textural setting of the 3 remaining monazite grains is ambiguous (Figure 8D). The calculated concordia age of 1870.3±3.0 Ma represents a well-documented monazite population of 12 grains (Figure 9). Three discordant monazite grains yield $^{207}Pb/^{206}Pb$ ages of c. 1780-1800 Ma. The textural setting of two of the discordant grains is ambiguous, while the third grain belongs to the spongy type. However, it is likely that the discordant grains belong to the main population, but mobilization of Pb and U resulted in higher $^{206}Pb/^{238}U$ and lower $^{207}Pb/^{235}U$ ratios.

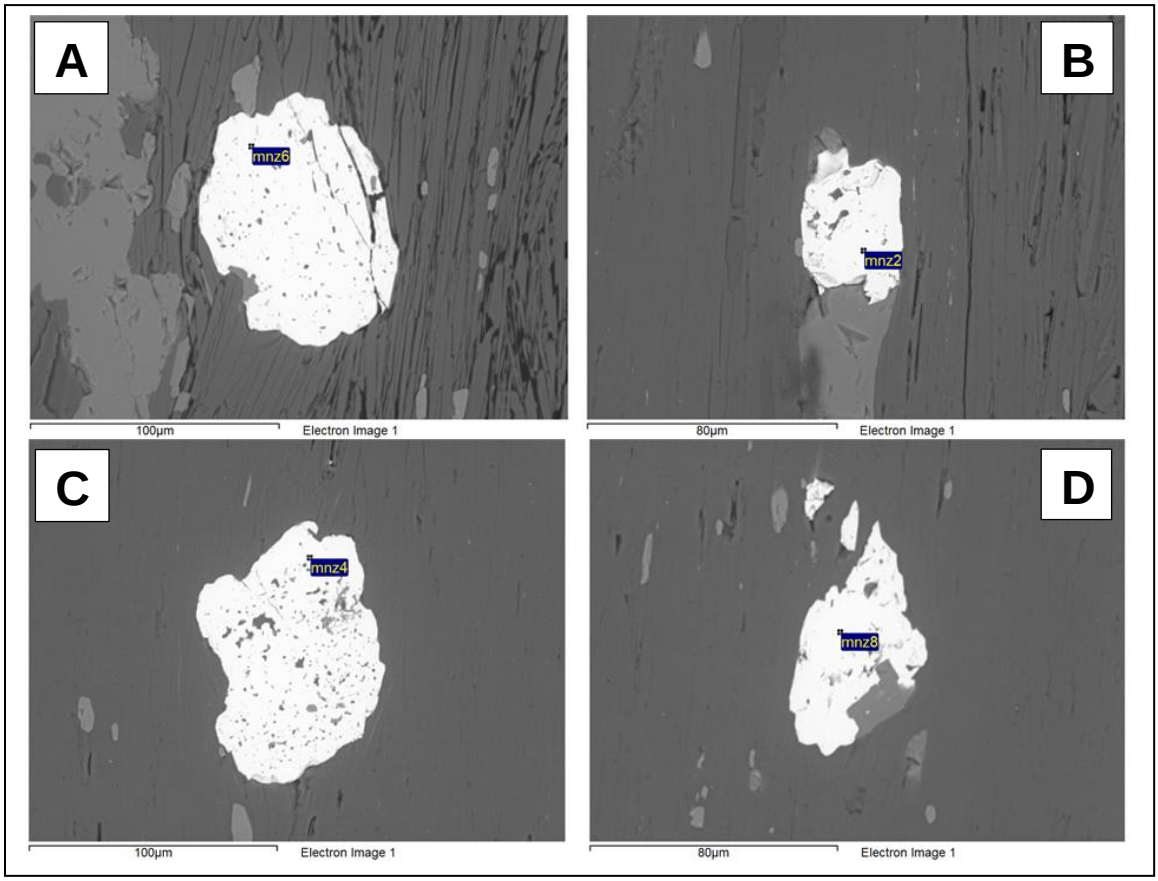

Figure 8. Texture observed in the monazite grains (SEM-BSE images) of sample 31-0-1 KOH-8 95.20. A – Monazite grain exhibiting features of both types. B – Strain shadow (metamorphic) monazite. C – Spongy type (hydrothermal) monazite. D – Monazite with ambiguous textural setting.

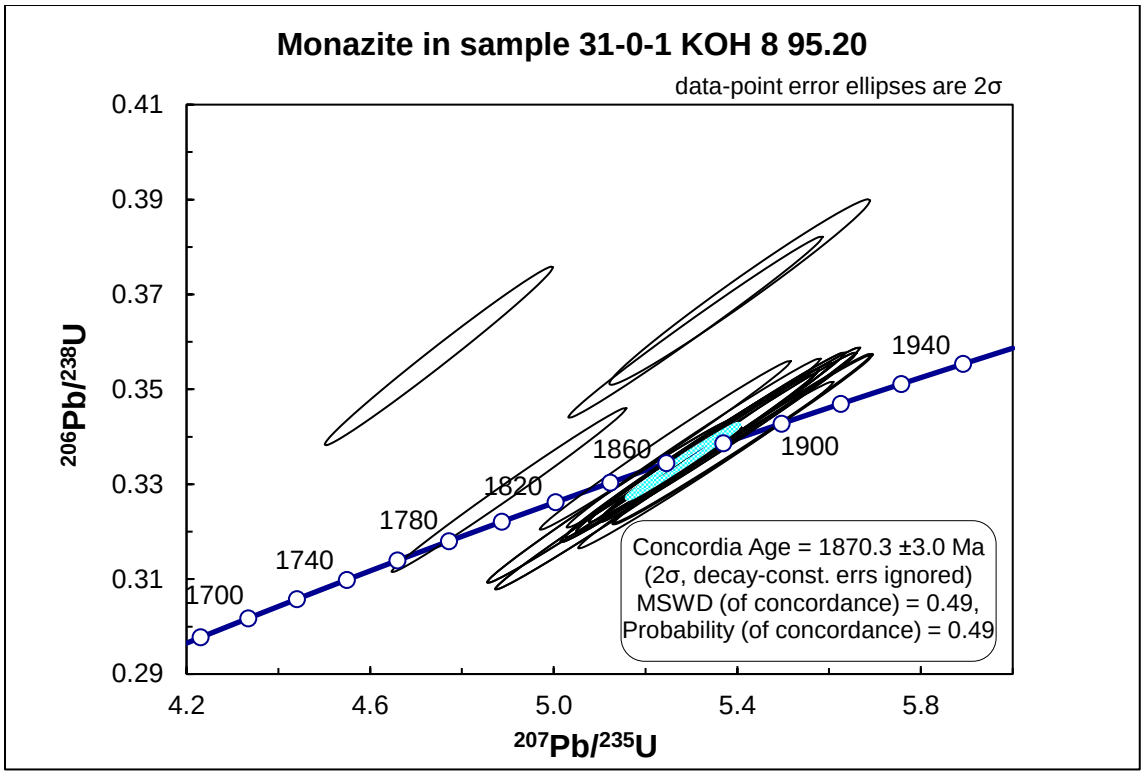

Figure 9. U-Pb concordia diagram for monazite in sample 31-0-1 KOH 8 95.

Sample 31-0-1 KOH-15 146.20

Sample 31-0-1 KOH-15 146.20 consists of three monazite grains of ambiguous textural setting and 2 zircon grains (Figures 10A-B). Two of these grains are concordant whose $^{207}Pb/^{206}Pb$ ages are 1894±12 Ma, 1866±12 Ma, whereas there is also a discordant grain with a 1732±12 Ma $^{207}Pb/^{206}Pb$ age (Figure 11).

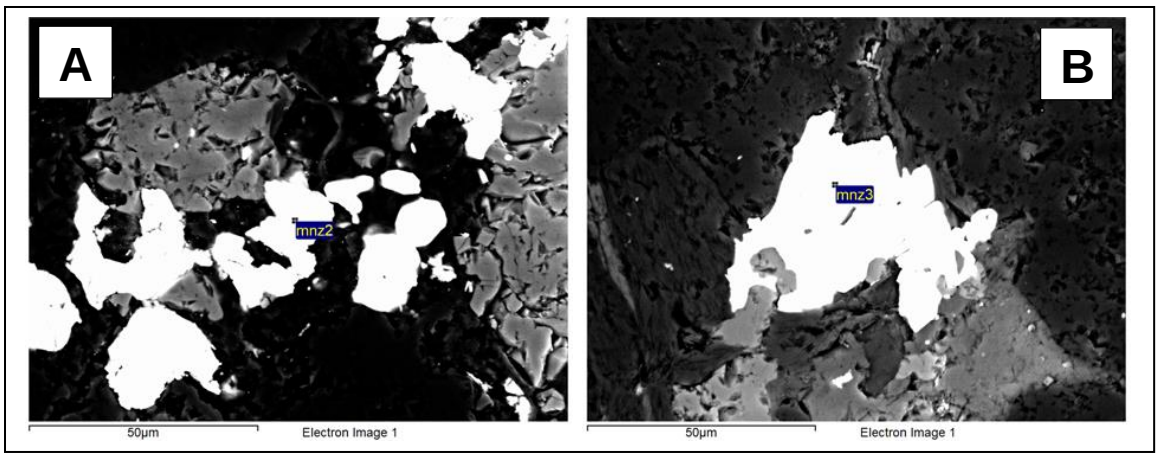

Figure 10. Texture of monazite grains (SEM-BSE images) of sample 31-0-1 KOH-15 146.20.

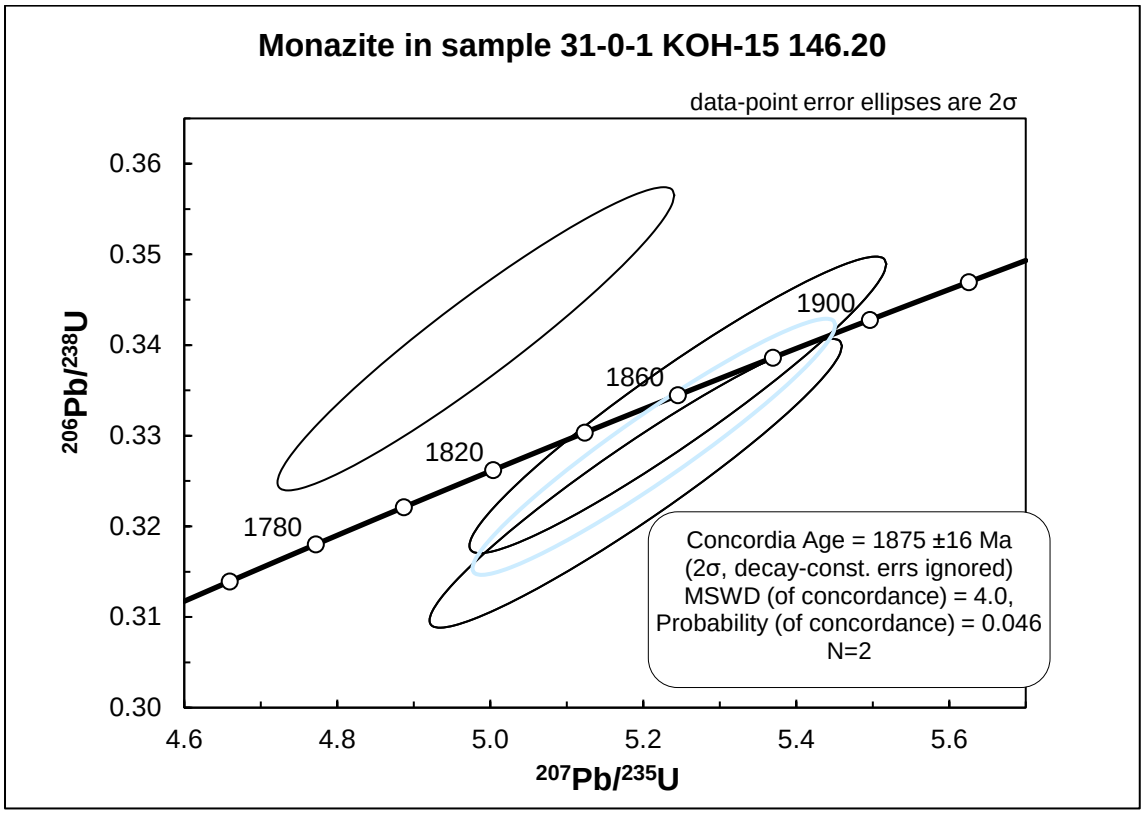

Figure 11. U-Pb concordia diagram for monazite in sample 31-0-1 KOH-15 146.20.

Sample 31-0-1 KOH-24x

Sample 31-0-1 KOH-24x is composed of 15 monazite grains and 1 zircon crystal. The textural setting for the majority of monazite grains remains unidentified, but four grains display spongy type features. Two spongy type grains are presented in Figures 12A-B. In the U-Pb concordia diagram (Figure 13), four monazite grains define a discordia line with a forced upper intercept of 1679±15 Ma, whereas there is a notable cluster of discordant monazite grains with higher $^{206}Pb/^{238}U$ and $^{207}Pb/^{235}U$ ratios. However, filtering of the data, reveals only one grain with a geologically meaningful $^{207}Pb/^{206}Pb$ age of 1834±13 Ma.

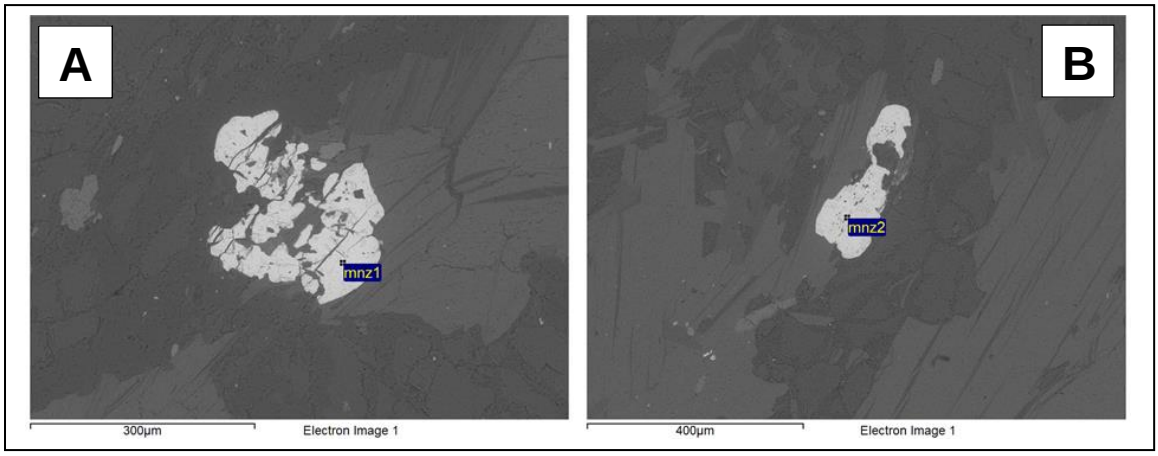

Figure 12. Two spongy type monazite grains (SEM-BSE images) of sample 31-0-1 KOH-24x.

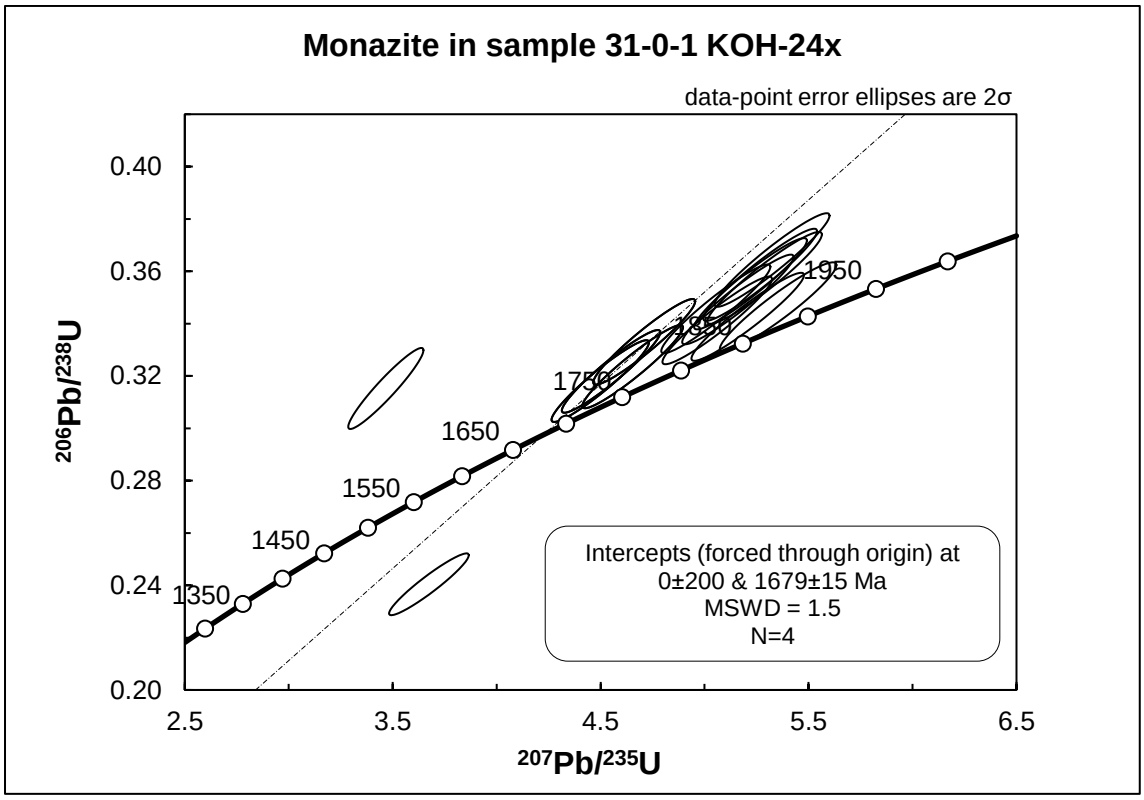

Figure 13. U-Pb concordia diagram for monazite in sample 31-0-1 KOH-24x.

Sample KU 021-6A

Sample KU 021-6A includes 4 zircons (Figures 14A-D) and 1 monazite which texture could not be specified. The majority of zircon analyses fall out of the limits that are set for the concordance, except for one grain with a $^{207}Pb/^{206}Pb$ age of 1950±9 Ma.

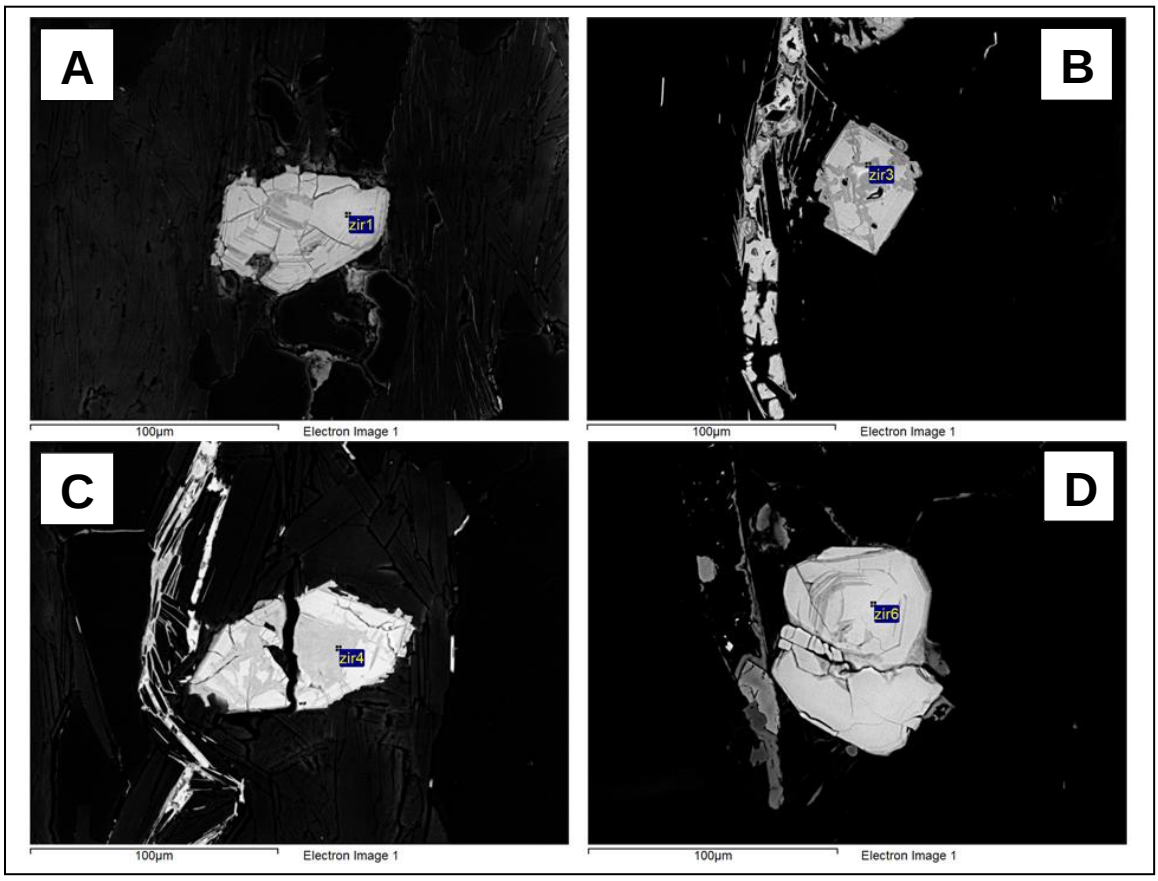

Figure 14. Zircon textures (SEM-BSE images) of sample KU 021-6A with characteristic oscillatory zoning.

Sample KU-174

Sample KU-174 is made up of 6 zircon grains, which appear corroded and fragmented, but features of their internal structures could not be recognized (Figures 15A-B). Five zircon grains produce a discordia line with an upper intercept of 1850.0±8.8 Ma. The remaining discordant zircon grain, which falls out of the discordia, possibly belongs to the same population, but is characterized by a lower $^{206}Pb/^{238}U$ ratio due to either loss of Pb or addition of U (Figure 16).

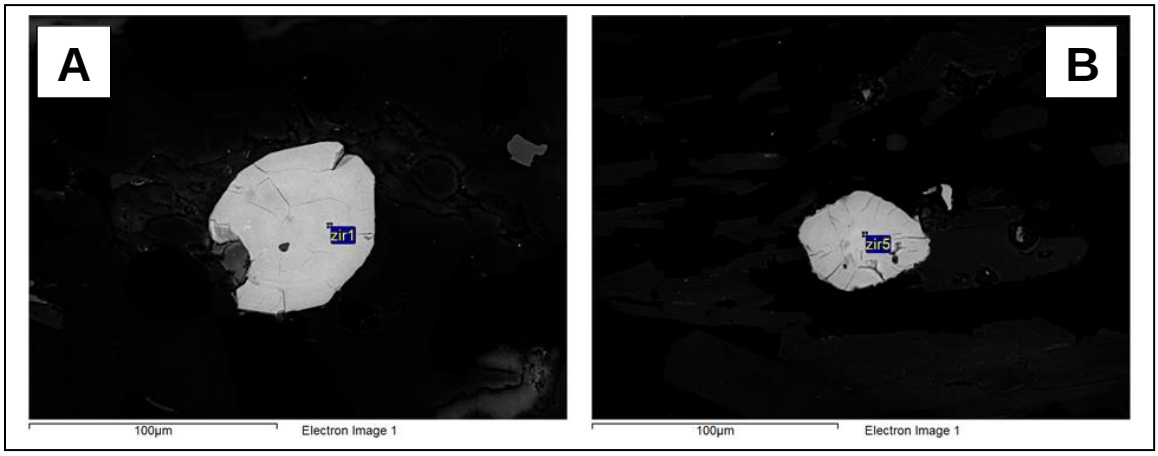

Figure 15. Zircon textures (SEM-BSE images) of sample KU-174.

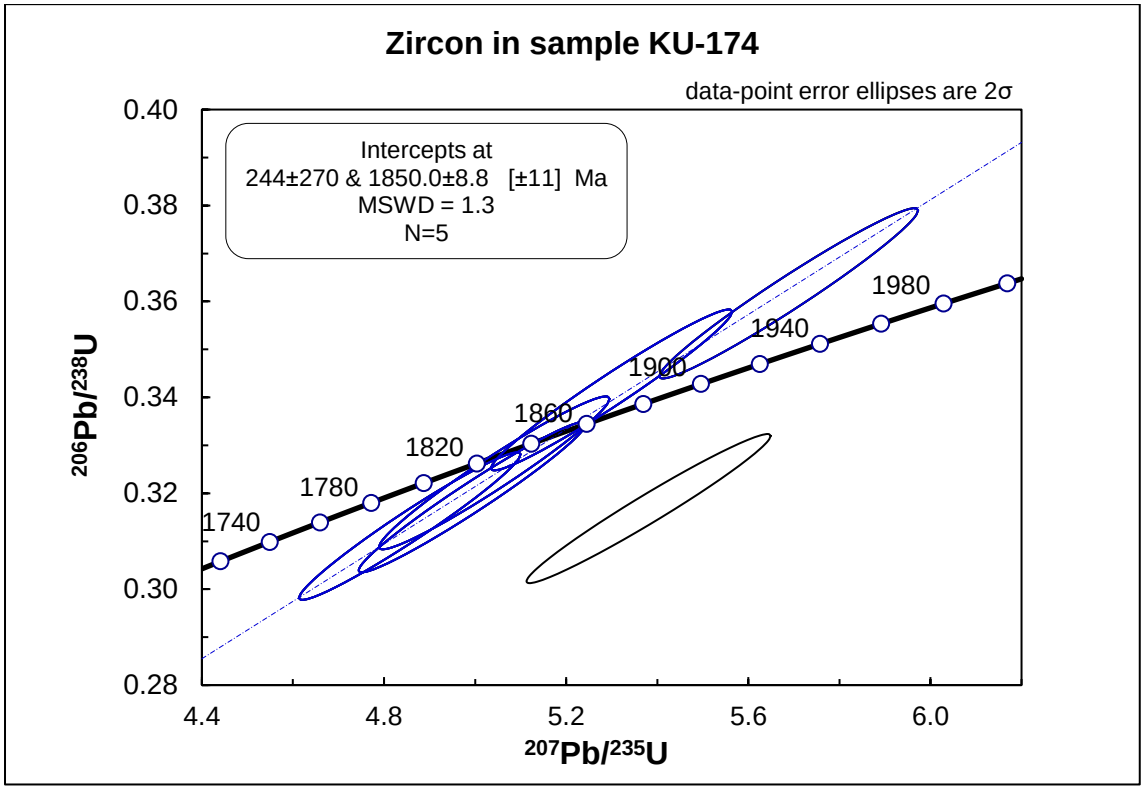

Figure 16. U-Pb concordia diagram for zircon in sample KU-174.

Sample KU-567 243.20

Thirteen monazite and 4 zircon grains were identified in sample KU-567 243.20. Monazite is divided into 2 strain shadow and 4 spongy type grains, whereas 1 grain belongs to both types and the remaining 6 grains cannot not be classified in one of the above types (Figures 17A-D). Zircon crystals are subhedral to anhedral, but their internal structure is not visible. Two concordant monazite grains have $^{207}Pb/^{206}Pb$ ages of 1894±4 Ma and 1866±4 Ma, in addition to a discordant population with a mean $^{207}Pb/^{206}Pb$ age of c. 1750 Ma that was filtered out, during data processing. The fact that both the discordant and the concordant monazites evidence similar $^{207}Pb/^{235}U$ ratio, but slightly elevated $^{206}Pb/^{238}U$ ratio, indicates that these grains constitute a single population (Figure 18).

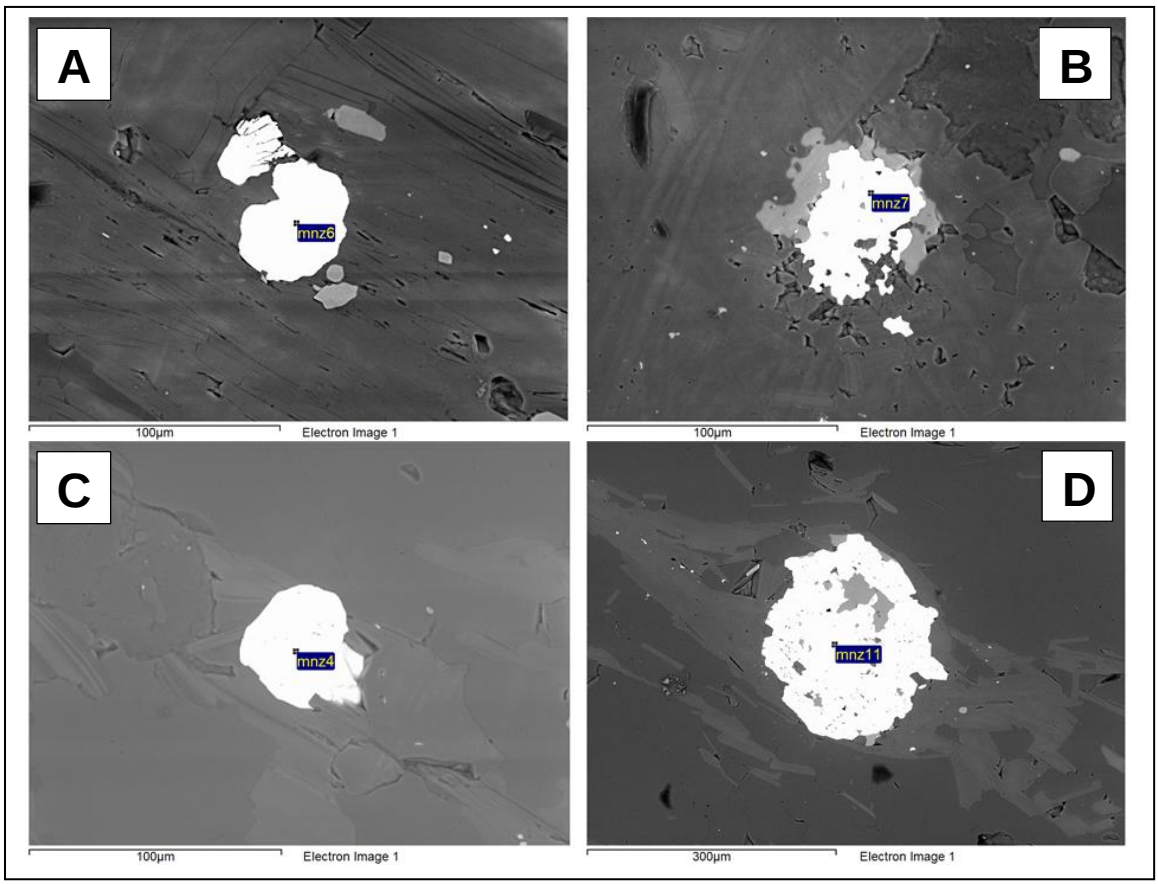

Figure 17. Texture of monazite grains (SEM-BSE images) of sample KU-567 243.20. A – Strain shadow (metamorphic) monazite. B – Spongy type (hydrothermal) monazite. C – Monazite which ambiguous textural monazite. D – Monazite grain exhibiting features of both types.

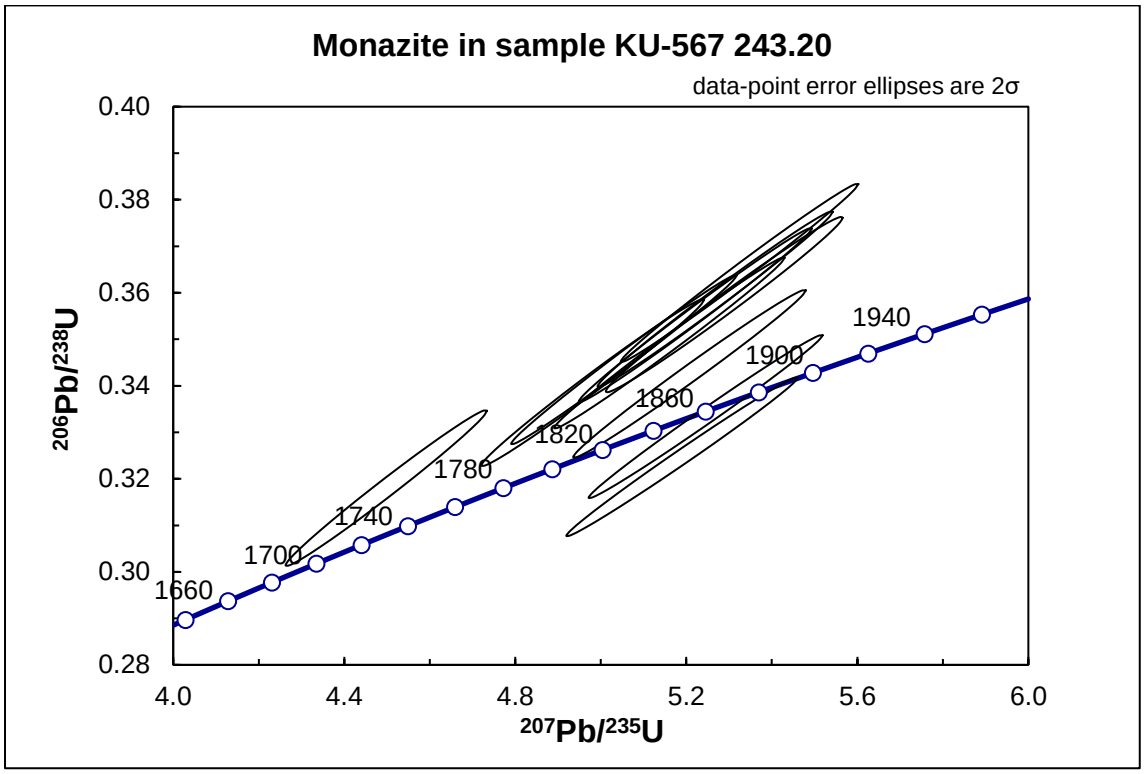

Figure 18. U-Pb concordia diagram for monazite in sample KU-567 243.20.

Sample KU-568 59.80

Sample KU-568 59.80 accommodates 10 monazite and 29 zircon grains. Monazite is characterized by anhedral and corroded grain boundaries and is distributed into 1 strain shadow type, 4 spongy type, and 5 ambiguous type grains (Figures 19A-B). Zircon includes mostly anhedral to subhedral crystals, several of which demonstrate oscillatory zoning, whilst others are enclosed by secondary material that is deposited around their rim (Figures 19C-F). Sample KU-568 59.80 is dominated by a cluster of slightly discordant monazite grains, plotted at around 1700 Ma (Figure 20), but after data filtering, the only reliable age is the $^{207}Pb/^{206}Pb$ age of 1834±7 Ma. With respect to zircon, U-Pb dating has revealed discordant grains (Figure 21) that can be separated into two groups, yielding mean $^{207}Pb/^{206}Pb$ ages of c. 1860 Ma and c. 1770 Ma.

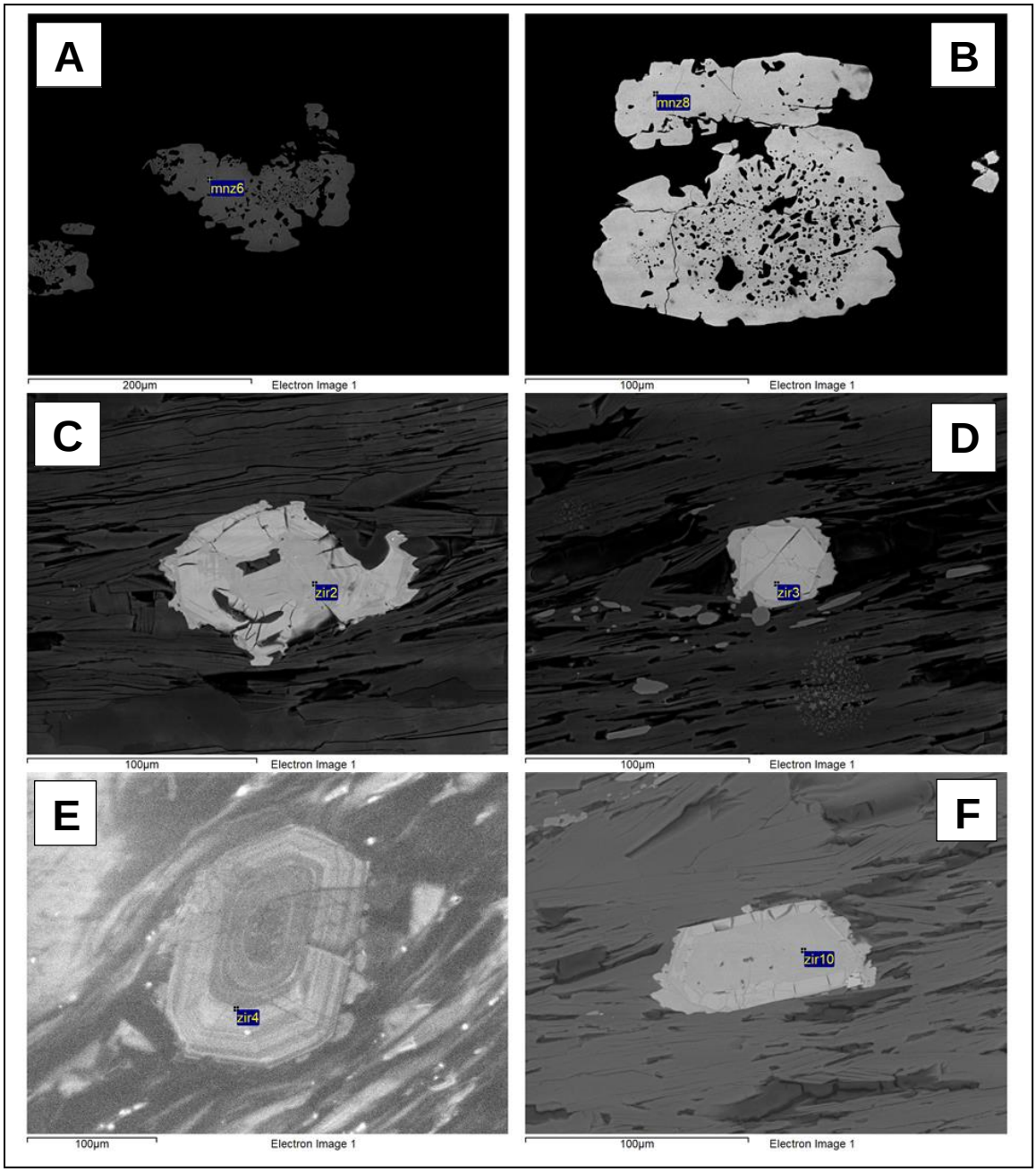

Figure 19. Textural settings and types of monazite and zircon grains (SEM-BSE images) of sample KU-568 59.80. A – Spongy type hydrothermal monazite grain. B – Spongy type hydrothermal monazite, marked by a core with a large number of inclusions. C –Corroded zircon grain around which the main foliation appears to be diverted. D – Euhedral zircon with distinctive strain shadow which is encompassed by a secondary mineral. E – Magmatic zircon with characteristic oscillatory zonation. F – Euhedral zircon grain in which a distinct rim zone is delineated.

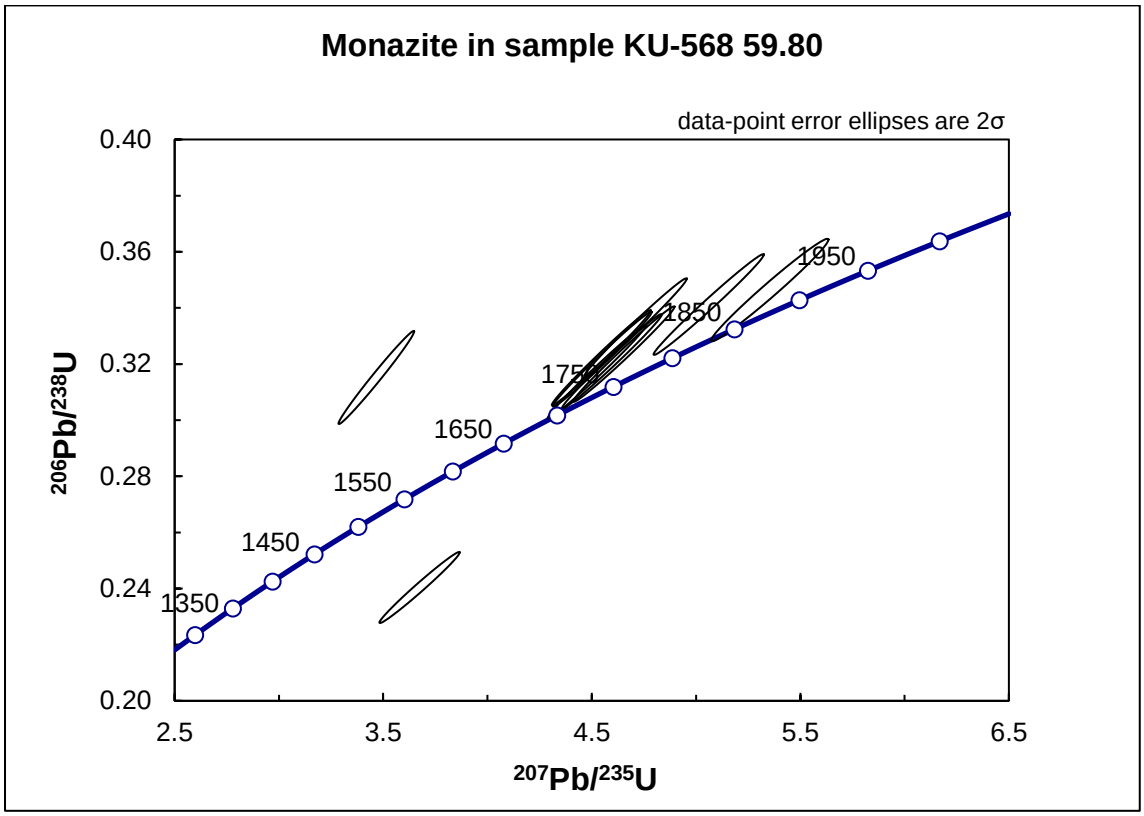

Figure 20. U-Pb concordia diagram for monazite in sample KU-568 59.80.

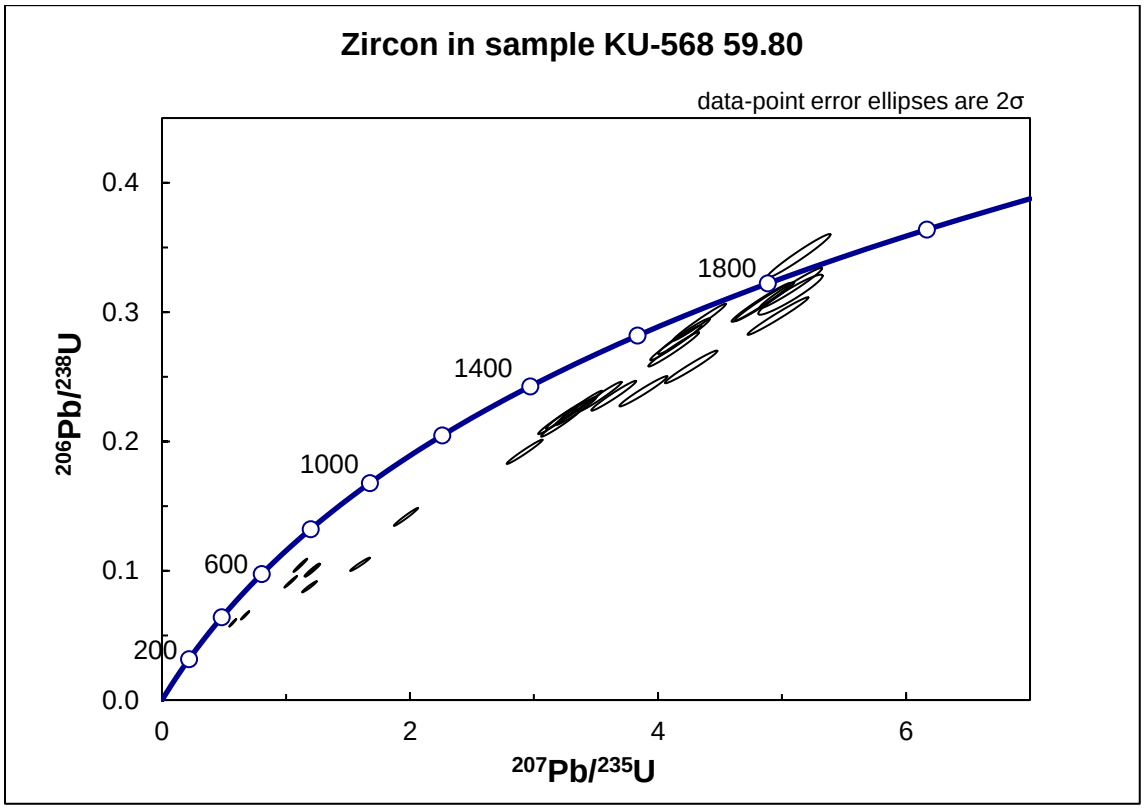

Figure 21. U-Pb concordia diagram for zircon in sample KU-568 59.80.

Sample KU-568 399.05

This sample has only 5 zircon grains, which are mostly rounded, with no special features.

Sample KU-569 308.80

Sample KU-569 308.80 hosts 4 monazite and 2 zircon grains, as well as the only detected xenotime crystal. Monazite is anhedral with corroded surfaces and is divided into 2 grains, which exhibit both strain shadow and inclusions, 1 strain shadow type grain and 1 grain with unspecified texture (Figures 22A-C). Zircon is euhedral and anhedral and exhibits strain shadow. All zircon ages have been filtered out, whereas in the case of monazite, two grains yield an Archean $^{207}Pb/^{206}Pb$ age of 2642 ± 11 Ma and a Paleoproterozoic $^{207}Pb/^{206}Pb$ age of 1917 ± 12 Ma.

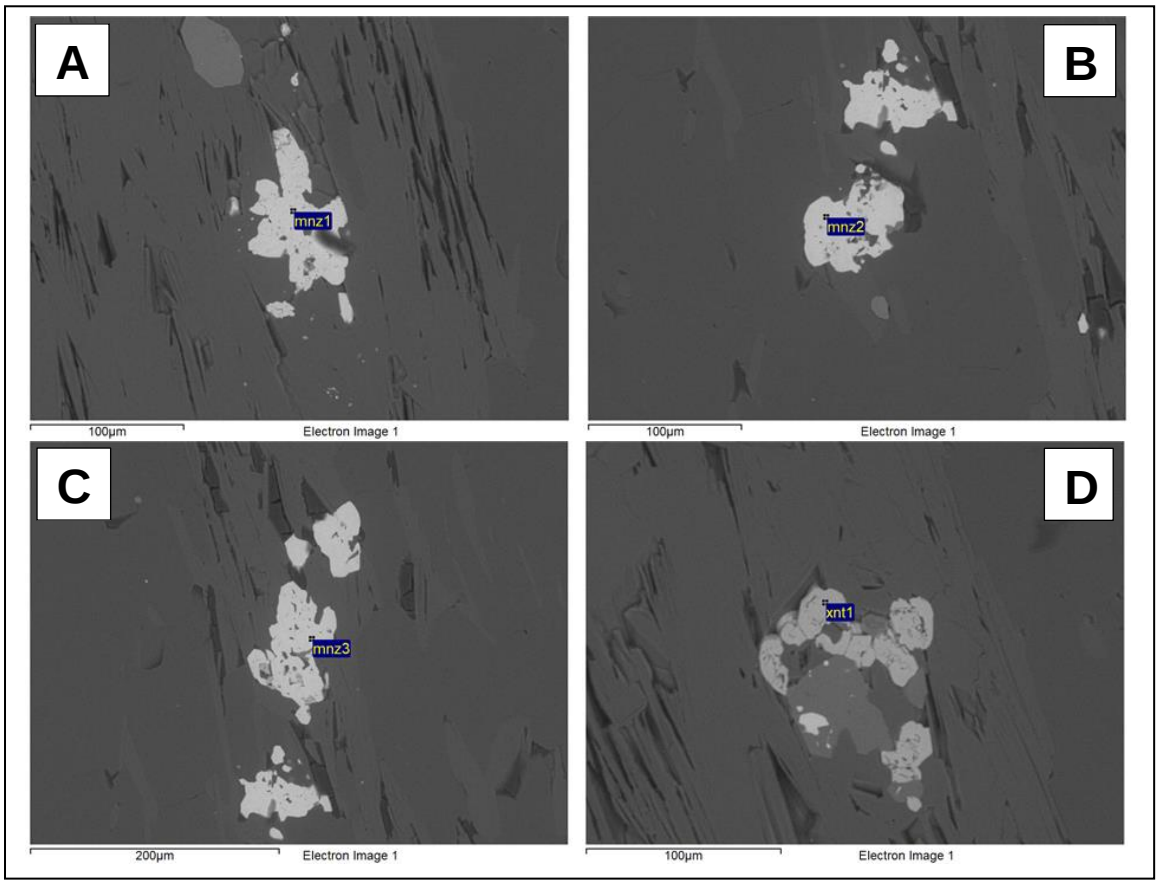

Figure 22. Texture of monazite and xenotime grains (SEM-BSE images) of sample KU-569 308.80. A – Strain shadow (metamorphic) monazite. B – Monazite grain with ambiguous textural setting. C – Monazite grain that exhibits features of both types. D – Spongy type (hydrothermal) xenotime grain.

Sample ORV/KU-453

Sample ORV/KU-453 consists of ten zircon grains, mainly of magmatic origin, in which oscillatory zonation can be observed. Grain boundaries range from euhedral to subhedral, but some anhedral grains with fragmented core and corroded rim also exist (Figures 23A-F). As it can be clearly seen from the U-Pb concordia diagram, there are three concordant grains and one discordant population (Figure 24). The latter is represented by four zircon ages that display $^{207}Pb/^{206}Pb$ ages that span between c. 1860 Ma and c. 1900 Ma.

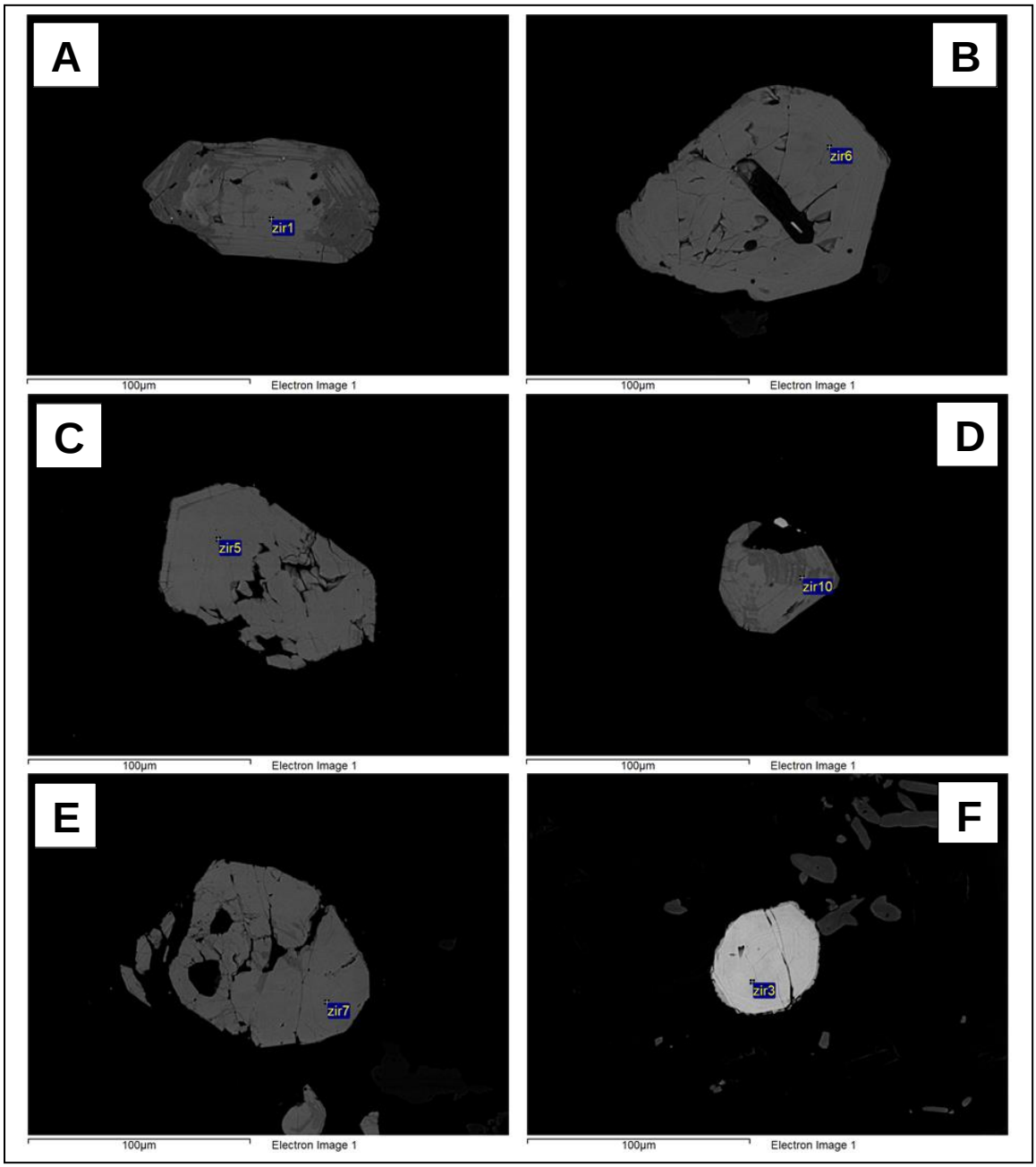

Figure 23. Texture of zircon grains (SEM-BSE images) of sample ORV/KU-453. A–B Euhedral grains. C–D Subhedral grains. E–F Anhedral grains.

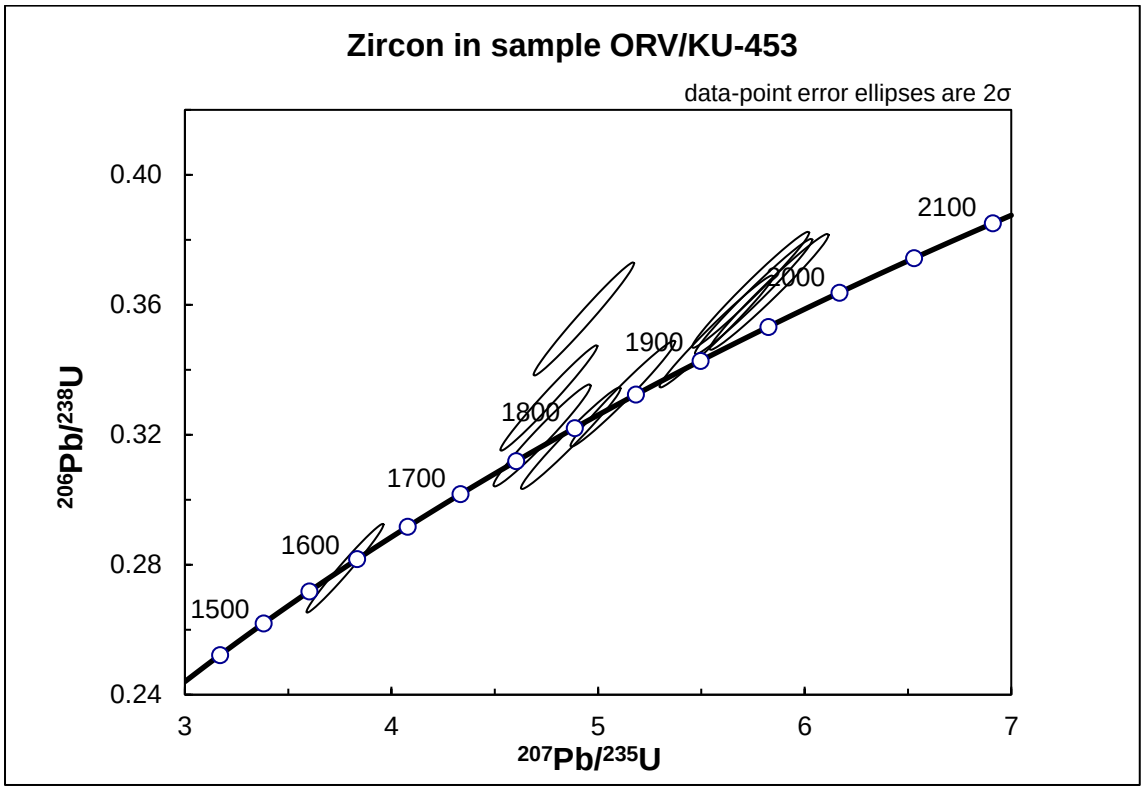

Figure 24. U-Pb concordia diagram for zircon in sample ORV KU-453.

Sample ORV/KU-543 anro 99-25453

Sample ORV/KU-543 contains 9 monazite and 3 zircon grains whose size was too small and therefore they were not used for U-Pb dating. Monazite is entirely anhedral and apart from one grain with ambiguous texture, the rest belong to the spongy type (Figures 25A-D). All $^{207}Pb/^{206}Pb$ ages are consistent and two grain populations can be discerned on the basis of the U-Pb concordia diagram (Figure 26). The first monazite population includes concordant grains that yield an age of 1877.6±4.0 Ma, whereas the second population is composed of discordant grains with $^{207}Pb/^{206}Pb$ ages that range between c. 1730 Ma and c. 1770 Ma. However, as it has been noted in previous samples, the discordant population demonstrates identical $^{207}Pb/^{235}U$ ratio, but somewhat increased $^{206}Pb/^{238}U$ ratio. As a result, it can be hypothesized that discordant grains represent concordant grains that experienced Pb loss or U addition.

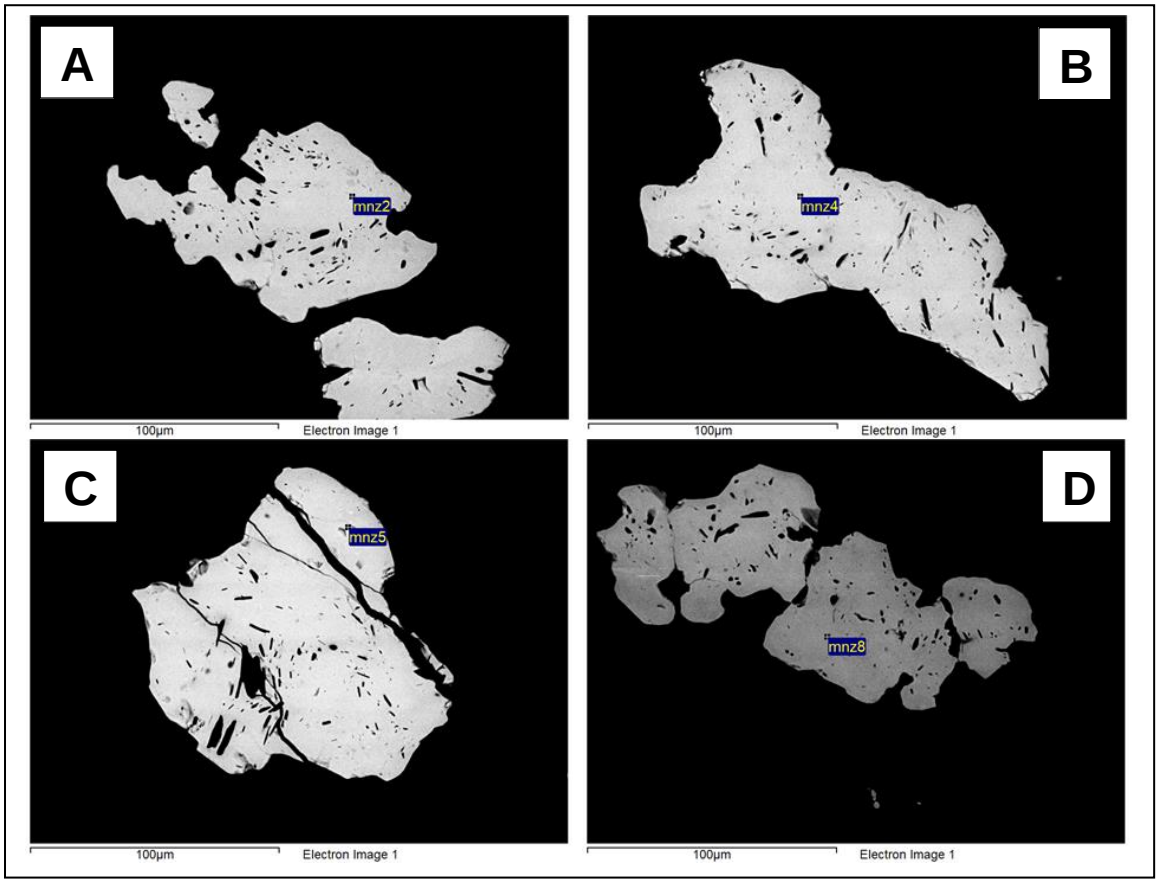

Figure 25. A-D SEM-BSE images of spongy type monazite grains of sample ORV/KU-543 anro 99-25453.

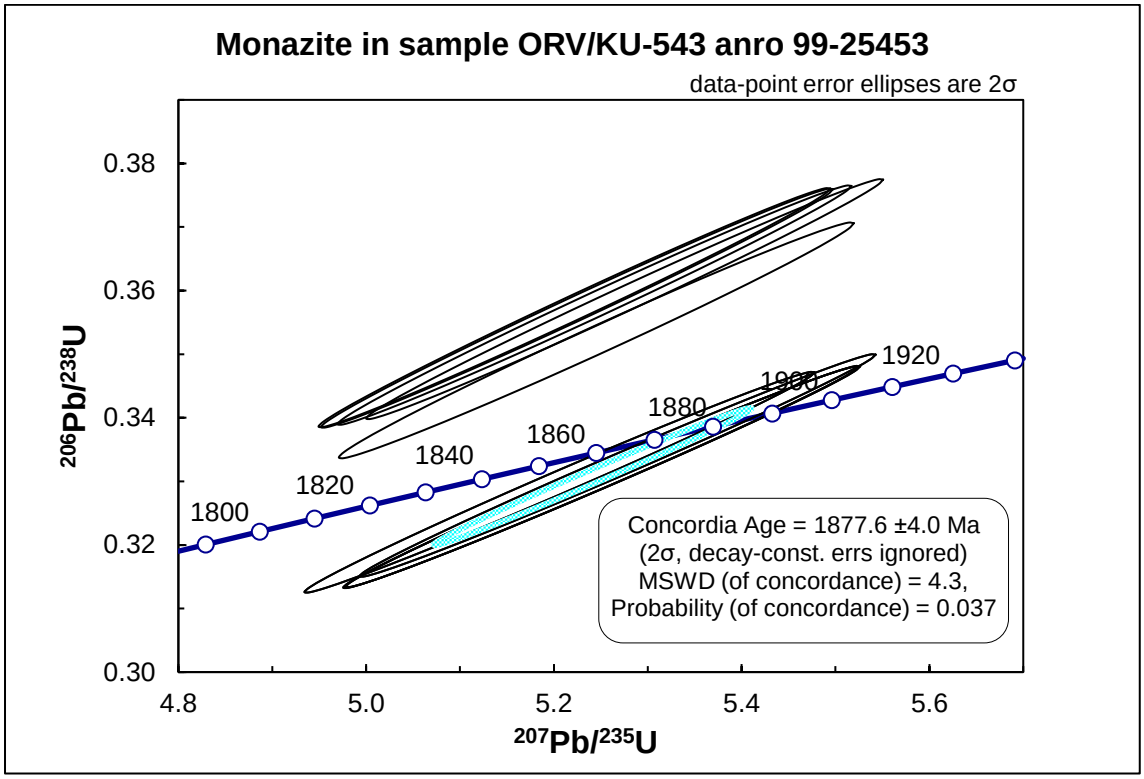

Figure 26. U-Pb concordia diagram for monazite in sample ORV/KU 543 anro 9925453.

Sample ORV/KU-582 99-26237

Sample ORV/KU-582 is constituted by 7 monazite grains and 1 zircon crystal that was excluded from the U-Pb dating process, owing to its inappropriate size. All monazite crystals have anhedral boundaries and correspond to the spongy type (Figures 27A-B). Overall, $^{207}Pb/^{206}Pb$ ages are considered imprecise with overly large 1σ errors (>20 Ma). Three grains are characterized by spurious $^{207}Pb/^{206}Pb$ ages of c. 5000 Ma. In the case of two grains, dating was unsuccessful, possibly, due to the large number of inclusions. The two remaining grains yield $^{207}Pb/^{206}Pb$ ages of 1916±24 Ma and 1599±29 Ma.

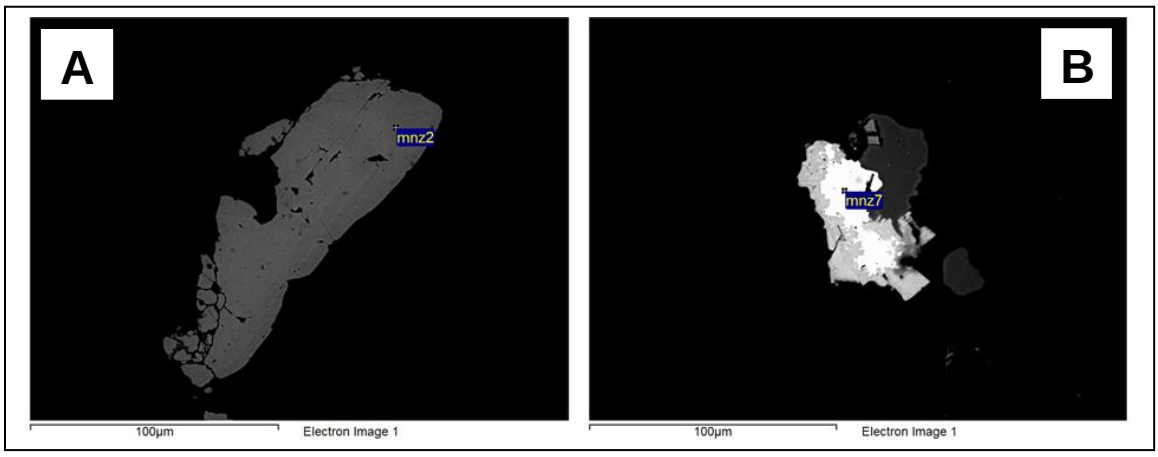

Figure 27. A-B SEM-BSE images of spongy type monazite grains of sample ORV/KU-582 anro 99-26237.

Sample ORV/KU-559 99-26127

SEM analysis detected 3 monazite and 4 zircon grains in sample ORV/KU-559 99-26127. Monazite is anhedral with corroded boundaries, which points to a spongy type textural setting (Figures 28A-B). Apart from one zircon that is euhedral, the remaining three grains are anhedral, and crystal #3 is of hydrothermal origin, as it has been depicted in Figure 7F. The three analyzed monazite grains are concordant (Figure 29) with $^{207}Pb/^{206}Pb$ ages of 1948±24 Ma, 1910±24 Ma and 1816±25 Ma. Given the lack of sufficient number of dated monazite grains, it cannot be explicitly stated that the three crystals form a population. Nonetheless, the 1σ error of the $^{207}Pb/^{206}Pb$ ages is high and similar for the three grains, and thus, it is plausible that they may constitute a grain population that was subjected to hydrothermal processes to different degrees.

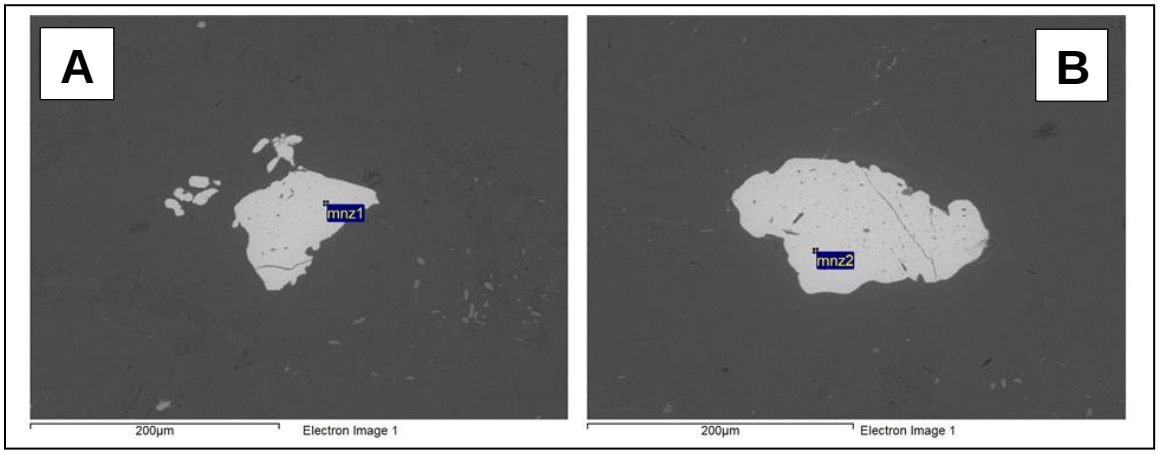

Figure 28. A-B SEM-BSE images of spongy type monazite grains of sample ORV/KU-559 anro 99-26127.

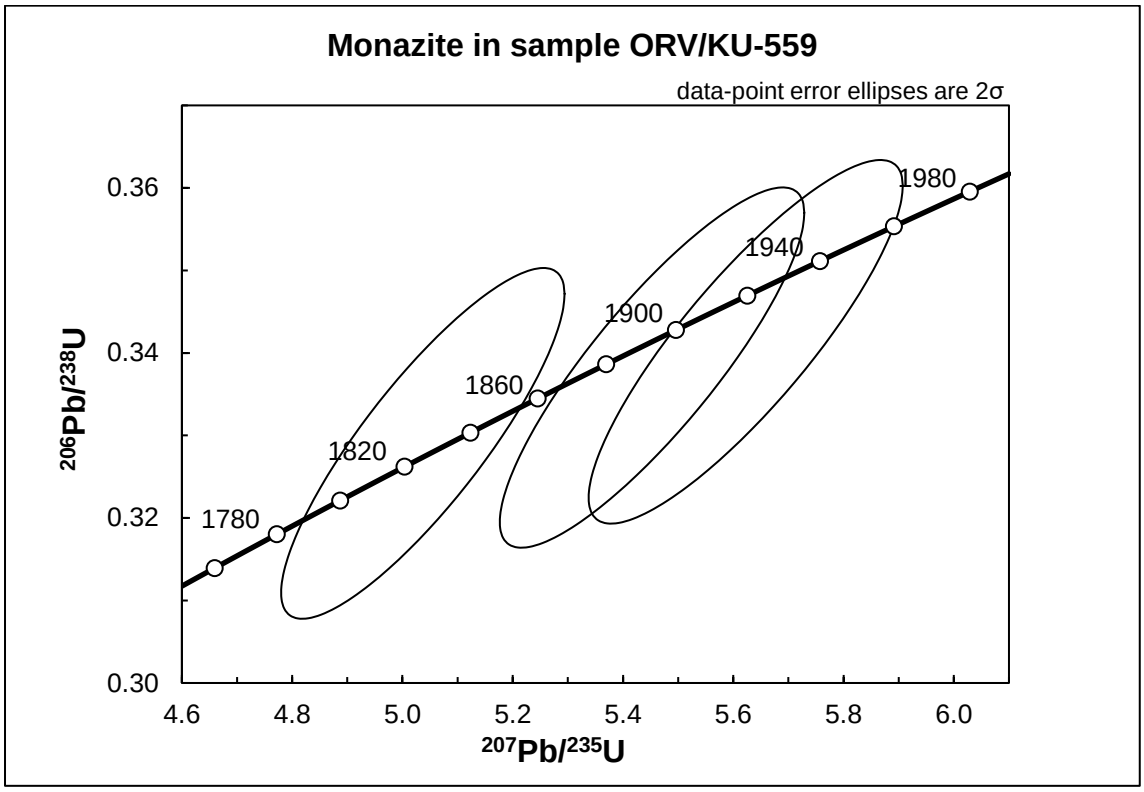

Figure 29. U-Pb concordia diagram for monazite in sample ORV/KU-559.

Sample Sarvisuo IA

Sample Sarvisuo IA is composed of 7 anhedral monazite grains. With respect to the textural setting, 4 grains correspond to the spongy type, one grain exhibits characteristics of both types, while two grains are classified as ambiguous (Figures 30A-F). In the U-Pb

concordia diagram (Figure 31), there are 4 concordant and three slightly discordant grains. Considering the similar texture, the $^{207}Pb/^{206}Pb$ ages, in spite of the high 1σ errors (>20 Ma), and their position in the concordia, all monazite grains may comprise a single population that underwent different degrees of Pb loss or U addition.

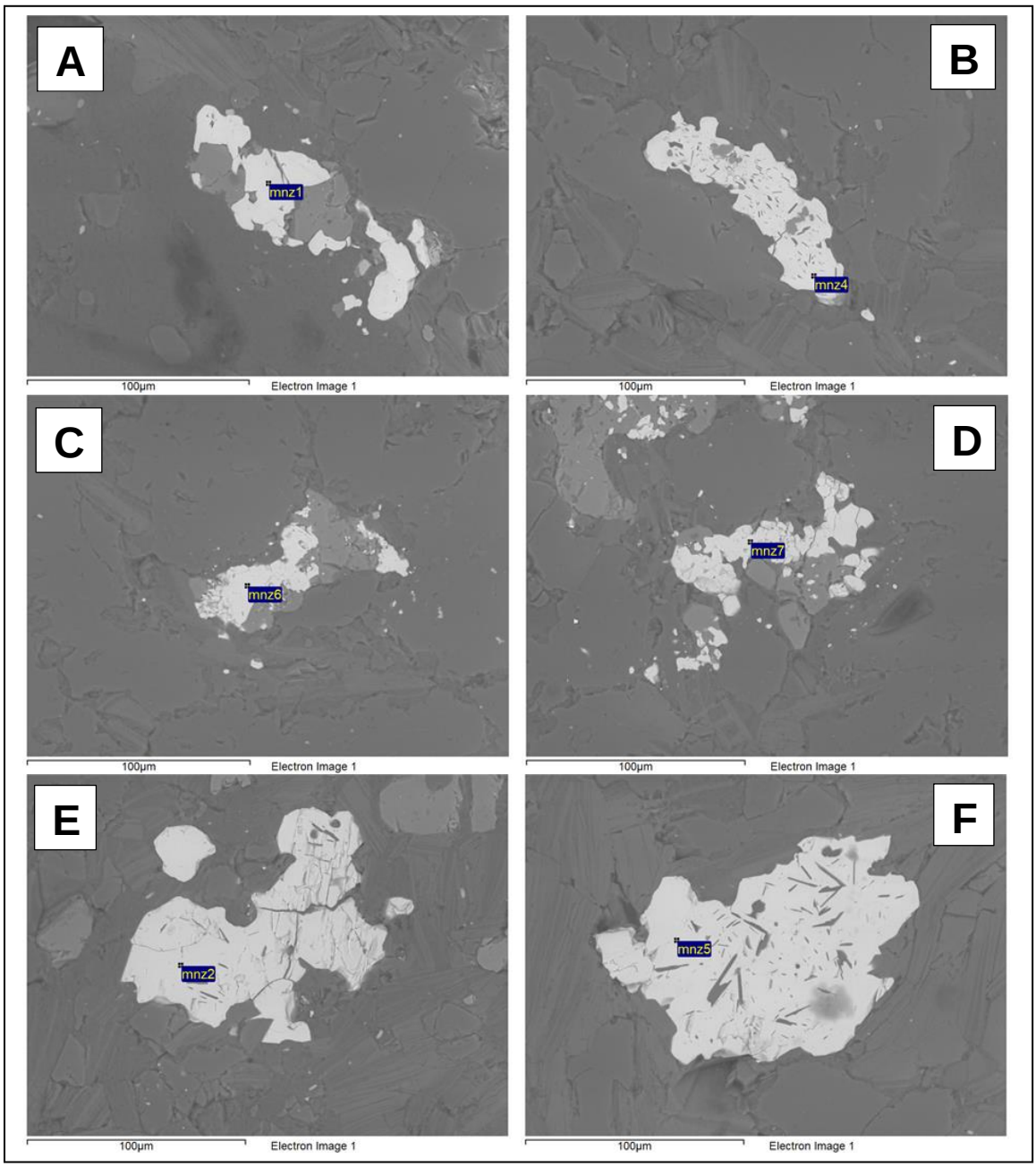

Figure 30. Texture of monazite grains (SEM-BSE images) of sample Sarvisuo IA. A–D Spongy type (hydrothermal) monazite grains. E – Monazite grain with ambiguous textural setting. F – Monazite grain that exhibits features of both types.

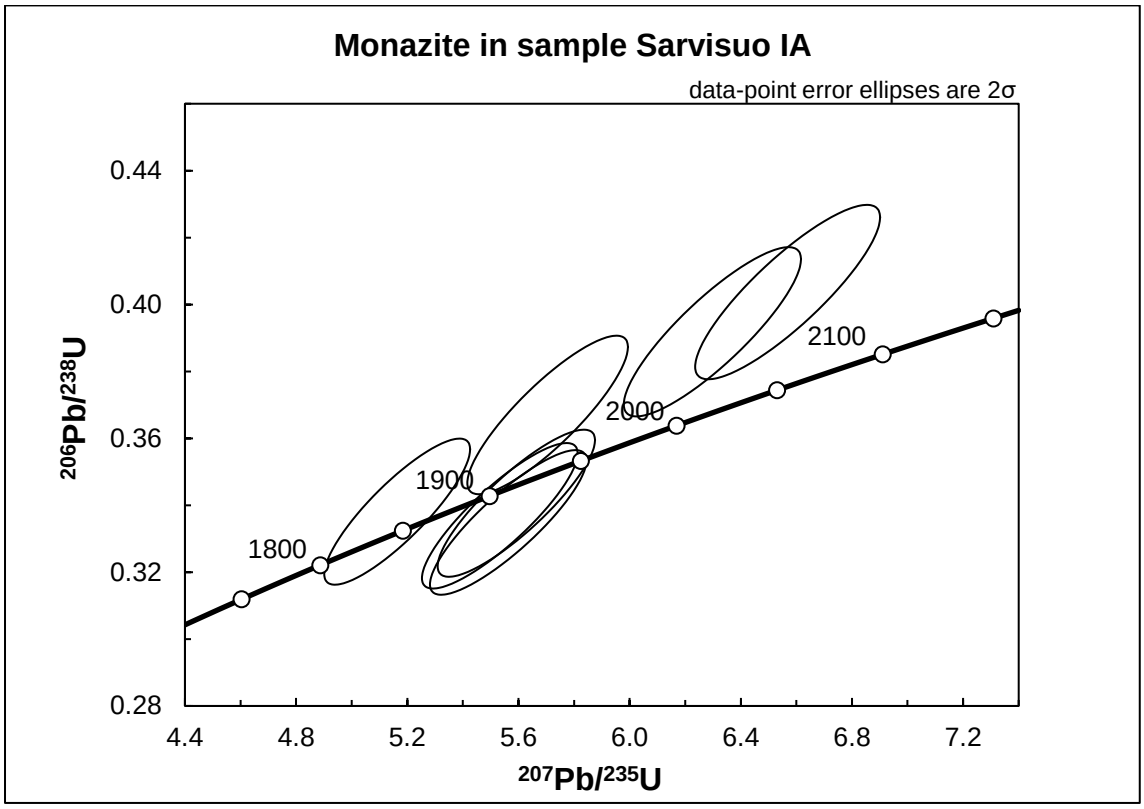

Figure 31. U-Pb concordia diagram for monazite in sample Sarvisuo IA.

Sample Sarvisuo IIA

SEM analysis yielded 40 monazite grains and 1 small zircon crystal that was excluded from U-Pb dating. All monazite grains are anhedral and based on their textural setting, they can be compartmentalized into two categories (Figures 32A-F). The first set includes spongy type grains of hydrothermal origin, which are distinguished on account of their highly corroded surfaces. The shape of the crystals is irregular and they have been partly replaced by secondary minerals, although the original boundaries can be easily demarcated. The second category of monazite involves grains of ambiguous texture, as no internal features are manifested. U-Pb results are coherent and even after filtering of the data, $^{207}Pb/^{206}Pb$ ages are accordant in most cases, despite the large 1σ error (>20 Ma). In the U-Pb concordia diagram (Figure 33), the majority of monazite grains are projected in the area between 1800 Ma and 2000 Ma. Three grains are plotted close to the well-defined cluster and display Archean ages, but the similar textural features denote that they belong to the same population of grains. However, monazite grains can be further divided

into two populations, on the basis of the $^{207}Pb/^{206}Pb$ ages of the filtered data. The first cluster of grains defines a concordia age of c. 1870 Ma, whereas a second cluster produces a c. 1830 Ma age. Two grains stand out as their much older ages suggest that they cannot be classified to neither of the two groups.

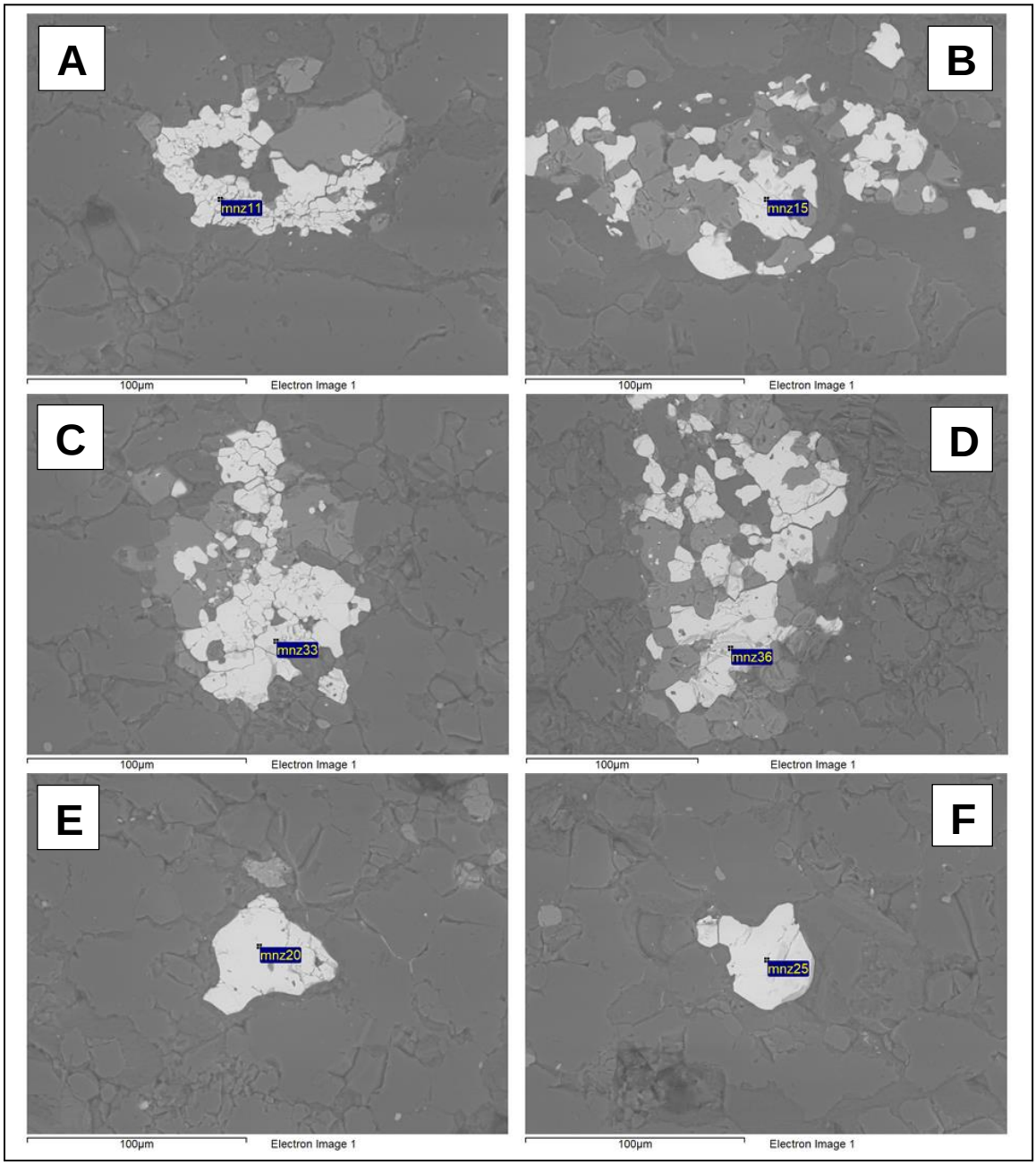

Figure 32. Texture of monazite grains (SEM-BSE images) of sample Sarvisuo IIA. A–D Spongy type (hydrothermal) monazite grains with corroded surfaces and secondary material deposited around the edges. E–F Monazite grains with ambiguous textural setting.

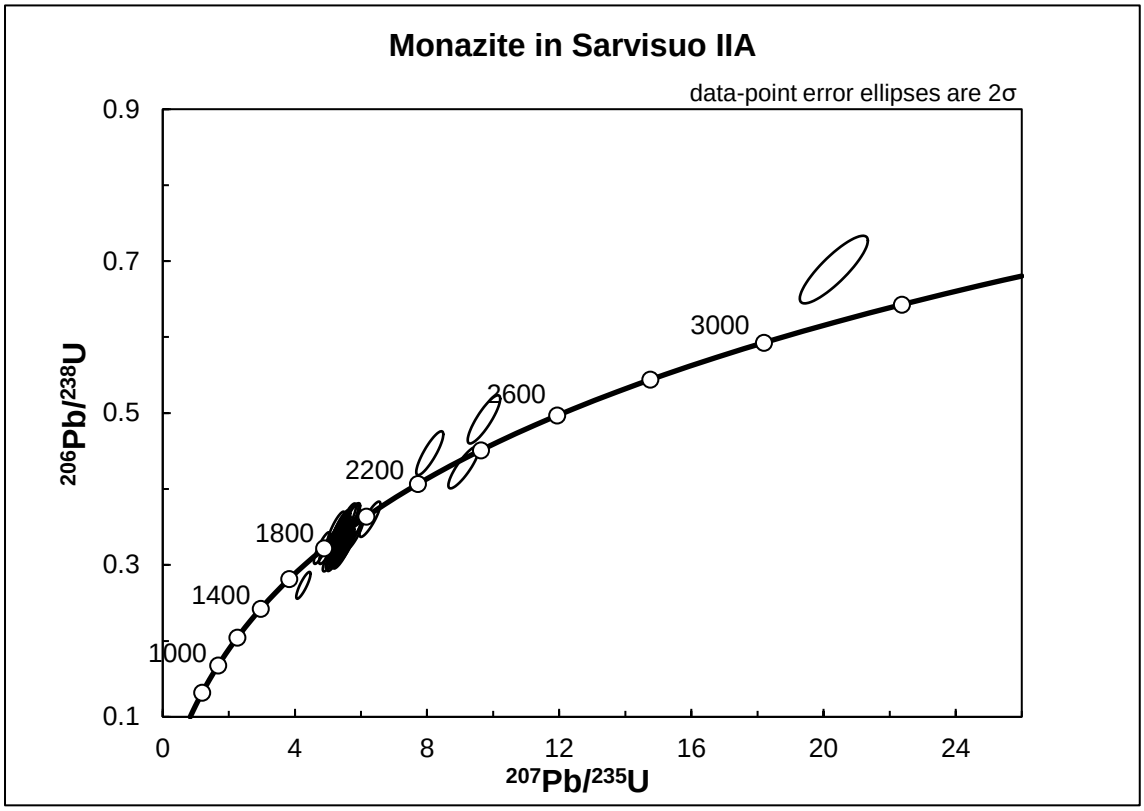

Figure 33. U-Pb concordia diagram for monazite in sample Sarvisuo IIA.

Sample A1447

Sample A1447 of Mänttäri et al. (1997) is a chlorite schist, comprised of hand-picked monazite and zircon grains. In total, 28 monazite and 45 zircon grains were selected for U-Pb dating. After filtering, the remaining data includes 20 monazite and 26 zircon grains. Both unfiltered and filtered data are characterized by congruity and despite the large 1σ errors (>15 Ma in most cases), safe conclusions can be drawn with reference to $^{207}Pb/^{206}Pb$ ages. The U-Pb diagrams for monazite and zircon are presented in Figures 34 and 35, respectively. Most monazite crystals are concordant and can be divided into two groups, based on their $^{207}Pb/^{206}Pb$ ages. The first group yields a concordia age of 1840.2±8.3 Ma, whilst the 1767 Ma concordia age of the second group is largely imprecise, owing to its large error of 32 Ma. The weighted mean $^{207}Pb/^{206}Pb$ age of sample A1447, which was calculated using the data from both populations, is 1816±23 Ma. The zircon grains of sample A1447 are distributed, on the basis of their $^{207}Pb/^{206}Pb$ ages, into two distinct clusters that intercept the concordia at 1895±11 Ma and 1873.8±8.9 Ma, respectively. The weighted mean $^{207}Pb/^{206}Pb$ age of sample A1447, which was produced

using the concordant and nearly concordant data, is 1869±13 Ma.

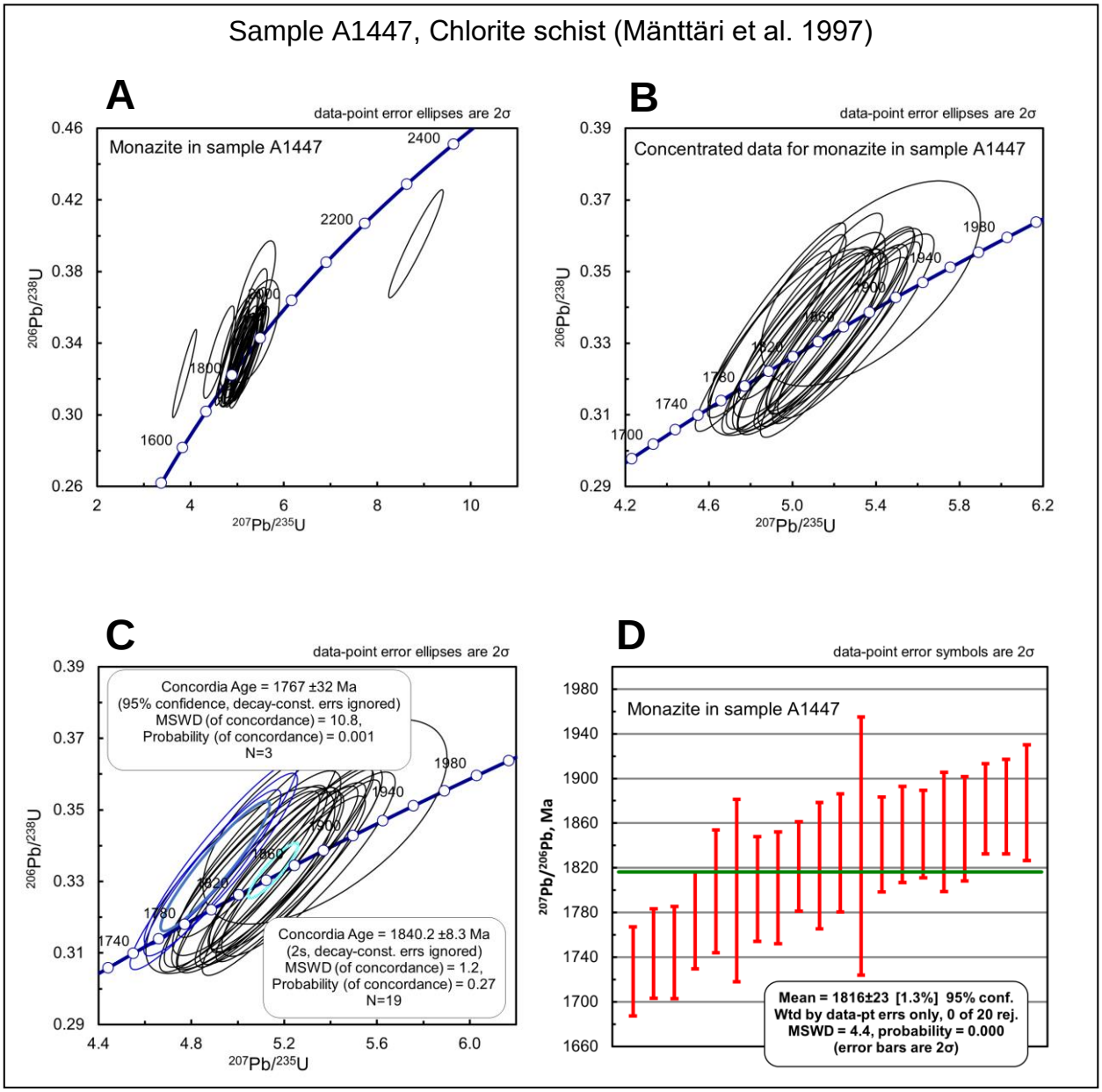

Figure 34. A – U-Pb concordia diagram for monazite in sample A1447. B – U-Pb concordia diagram of the concentrated data for monazite in sample A1447. C – U-Pb concordia diagram of the provisional ages for monazite in sample A1447. D – Individual $^{207}Pb/^{206}Pb$ concordant monazite data used in calculation of weighted mean age of sample A1447.

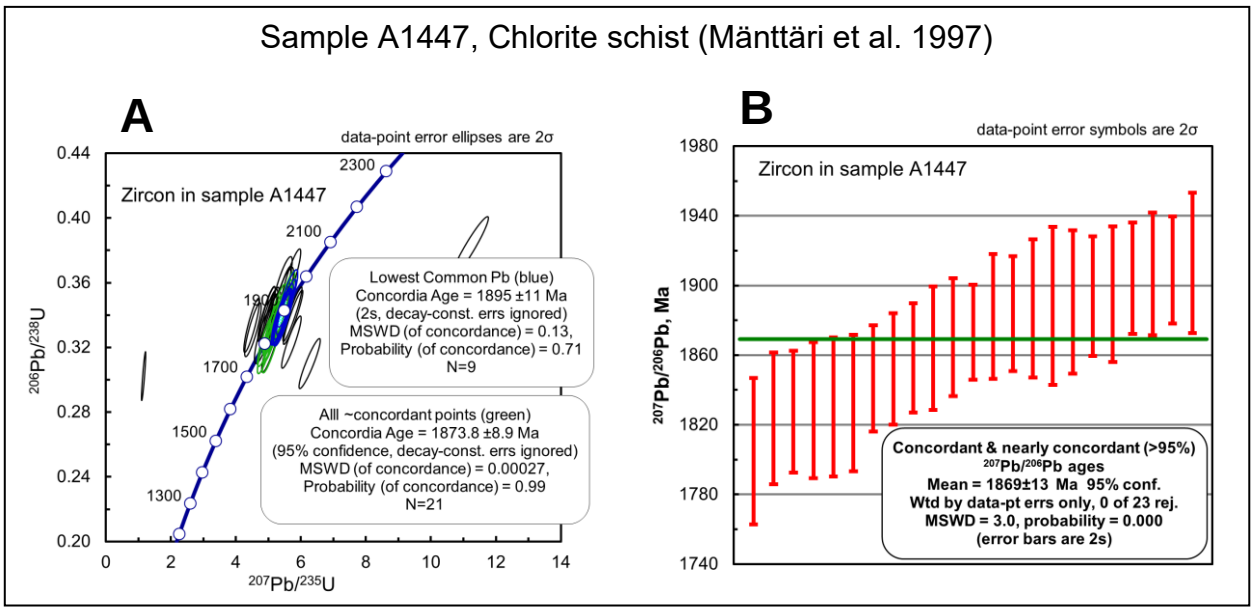

Figure 35. A – U-Pb concordia diagram for zircon in sample A1447. B – Individual $^{207}Pb/^{206}Pb$ concordant zircon data used in calculation of weighted mean age of sample A1447.

Sample A1675

Sample A1675 of Talikka and Mänttäri (2005) is a granodiorite from the hypabyssal Pukala intrusion, which consists of hand-picked zircon grains. U-Pb dating was conducted for 44 selected zircon grains. Filtered data includes 35 zircon grains whose $^{207}Pb/^{206}Pb$ ages are uniform, albeit with large 1σ errors (c. 20 Ma), and range from 1862 Ma to 1928 Ma. U-Pb dating yields a single population of zircon grains with an upper intercept age of 1890.1±6.0 Ma (Figure 36). Nevertheless, comparison and sorting of $^{207}Pb/^{206}Pb$ ages of both unfiltered and filtered data reveals that there are two grain populations at c. 1890–1900 Ma and c. 1870–1890 Ma, alongside some scattered older and younger ages.

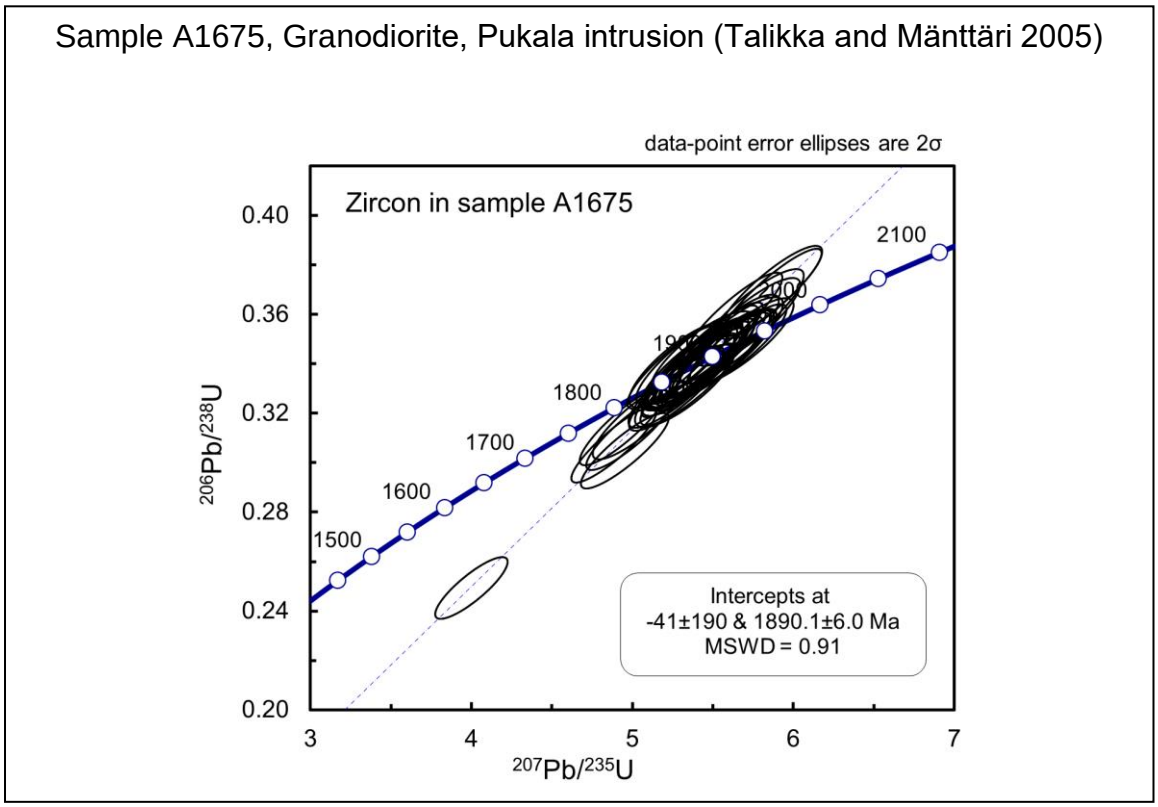

Figure 36. U-Pb concordia diagram for zircon in sample A1675.

5. Discussion

5.1. Interpretation of age data and radiogenic isotope compositions

The majority of the individual analytical spots in monazite and zircon from the Kutemajärvi deposit provides concordant U-Pb data. The limit of the acceptable concordance has been set between 95 and 105%, in order to filter the data and present the most meaningful results. The setting of this limit is arbitrary and differs for every laboratory, depending on the analytical methods, the data processing techniques and the nature of the studied geological problem (Molnar et al. 2018). In the U-Pb concordia diagrams, filtering of the data was not applied, resulting in a great variability with regard to the position of monazite and zircon relative to the concordia. The incongruity of the discordant data is a consequence of U and Pb losses during metamorphism and alteration events, as well as of the involvement of inclusions in the interior of the grains.

After filtering, $^{207}Pb/^{206}Pb$ monazite ages were sorted on the basis of the textural setting of the individual analyzed grains. However, this classification method did not produce a good correlation between ages and texture, as several grains with similar ages were characterized by different texture. By contrast, sorting of the $^{207}Pb/^{206}Pb$ ages for monazite with reference to the mineralogy of each sample separately revealed distinct populations of grains, which in many cases were identical to those of the U-Pb concordia diagrams. The latter approach was also preferred for the $^{207}Pb/^{206}Pb$ ages of zircon grains. Moreover, the sorted data for both monazite and zircon were compared to the major tectonometamorphic events of the Kutemajärvi gold deposit, the Tampere Schist Belt, as well as of the Central and Southern Svecofennian Arc Complexes and were further categorized to four distinct stages of geodynamic evolution as they are described in the next section.

Monazite isotope composition results produced by SEM analysis showed only minor discrepancies in the REE content that could not be utilized to classify the grains to different types. Overall, SEM analysis is considered to be an inaccurate method, as opposed to other analytical techniques, such as Electron Probe Microanalysis (EPMA) and X-Ray Fluorescence (XRF), which are extensively employed to determine the geochemical composition of a sample. The diversity of monazite geochemistry can be explained by various processes, which also have a profound effect in the texture and the obtained U-Pb ages of the analyzed grains.

As a REE-phosphate mineral, monazite is highly resistant to alteration and along with zircon, it abounds in metamorphic, magmatic as well as in sedimentary rocks as a detrital mineral (Van Emden et al. 1997, Roy 1999). Nonetheless, numerous studies have demonstrated that U-Th-Pb monazite systematics can be strongly disarrayed by fluids, accompanied by addition or depletion of one or more of these components and produce spurious ages. According to Ayers et al. (2004), monazite solubility is low in near-neutral pH aqueous fluids but increases in acidic and alkaline fluids. Dissolution of monazite increases as the fluid composition is shifted to the acidic or the alkaline field of the pH scale, and the rates of solubility and dissolution of REE-phosphates in brines increases with increasing temperature (Oelkers and Poitrasson 2002, Hetherington et al. 2010). The partitioning character or REE, U, Th and Pb is critically dependent on fluid composition, pH, availability of ligand species, REDOX conditions, and temperature (Hetherington et al. 2010). It has been arguably shown (Wood 1990a, 1990b, Hetherington et al. 2010) that

monazite becomes overly dissolved in fluids, in which strong anions [(F, Cl, $(SO_4)^{2-}$)] predominate, and precipitates elsewhere as a result of its changing solubility, caused by changes of the physical or chemical parameters of the fluid (P, T and composition). This fluid-related coupled dissolution-reprecipitation process can induce alteration of monazite composition and takes place at temperatures below the diffusional closure temperatures. In addition to monazite modification, this process often involves partial removal of Pb, resulting in resetting of monazite ages that justifies the apparent age discrepancies. Fluid-monazite interaction also causes characteristic concomitant textures such as, skeletal monazite, growth of precipitated monazite around grain boundaries, precipitation and growth of secondary monazite and REE-bearing phases (Rasmussen and Muhling 2007, Berger et al. 2008). Consequently, identification of monazite textures is of paramount importance, in order to discriminate altered from unaltered domains, which can reveal information about the age of fluid-aided recrystallization and the age of earlier magmatic or metamorphic events (Williams et al. 2011, Seydoux-Guillaume et al. 2012).

5.2. Implications of results for the tectonometamorphic evolution of the Kutemajärvi gold deposit

5.2.1. Pre-collision events

Samples KU-569 308.80 and ORV KU-559 of this study produce slightly older U-Pb monazite ages of 1917±12 Ma and 1910±24, respectively, which together with other monazite and zircon grains that yield even older ages, predate the emplacement ages of both the Koskuenjärvi formation and the Pukala intrusion. Based on their textural setting, sample KU-569 308.80 is characterized by spongy and strain shadow type textures, whereas only spongy type texture has been identified in sample ORV KU-559. The models for the geodynamic evolution of Tampere Schist Belt, proposed by Lahtinen et al. (2009), Kalliomäki et al. (2014), and Kara et al. (2021), suggest that collision between the Karelian craton and the western continental mass, comprised of the Keitele, Bergslagen and Norbotten microcontinents, initiated at 1.92 Ga. Rifting along the southern margin of the composite continental mass led to the formation of the Tampere basin and the deposition of the rift-related E-MORB Haveri-type mafic volcanics due to

melting of the subcontinental lithospheric mantle. The Haveri formation is poorly constrained, but according to these studies it is reputed to have been deposited prior to 1.91 Ga and its geochemical affinities point to a back-arc or marginal basin that evolved to a mature basin with N-MORB volcanics. Therefore, the monazite and zircon ages of these samples may represent inherited cores of detrital material, formed in a continental rift zone and denote the existence of evolved crust, older than 1.91 Ga, affiliated to prior Paleoproterozoic orogenic events (Huhma et al. 1991, Lahtinen and Huhma 1997, Lahtinen et al. 2009, Kara et al. 2021).

5.2.2. Early-collision events

The $^{207}Pb/^{206}Pb$ age of 1890.1±6.0 Ma, derived from the reanalyzed granodiorite sample A1675 of the Pukala intrusion, concurs with the multi-grains TIMS age of 1896±3 Ma of Talikka and Mänttäri (2005). The Pukala intrusion is situated in the eastern side of the Tampere Schist Belt in the contact zone between the Central Finland Granitoid Complex to the north and the Tampere Schist Belt to the south. Its geochemical and tectonic features suggest that it was emplaced in an island-arc or fore-arc setting during the early stages of the Svecofennian orogeny at c. 1.89 Ga, before the main regional metamorphic peak that occurred at c. 1.88 Ga (Kähkönen 1989, Kilpeläinen et al. 1994, Kilpeläinen, 1998, Talikka and Mänttäri 2005, Talikka 2007). Occurrence of textures, such as “unidirectional solidification textures” indicate that fluid phase separation took place during the time of emplacement and solidification of the intrusion. Thus, it is presumed that a magmatic-hydrothermal system coexisted with the emplacement of the intrusion at epithermal depths (1.5–2.5 km) at c. 1.89 Ga (Talikka and Mänttäri 2005).

Sample A1447 is a chlorite schist, derived from the Kutemajärvi gold deposit, with a Pb-Pb isochron age of 1808±32 Ma (Mänttäri et al. 1997). However, U-Pb results of the current study for the zircon of the reanalyzed sample A1447 show that one population yields a 1895±11 Ma magmatic age. In addition, samples 31-0-1 KOH-15 146.20 (quartz-dominant schist with topaz and andalusite) and KU-567 243.20 (chlorite-dominant schist) yielded equal U-Pb monazite ages of 1894±12 Ma and 1894±4 Ma, respectively. Therefore, hydrothermal monazite ages from altered host rock of the intrusion are within error to the age of the Pukala intrusion, affirming that hydrothermal activity was indeed associated with the intrusion of the Pukala pluton. This age also corresponds to the depositional ages of volcanic and plutonic rocks from the Tampere Schist Belt (Kähkönen

et al. 1989). According to Kähkönen et al. (1989), the U-Pb zircon age of the Koskuenjärvi formation that hosts the Kutemajärvi gold deposit is 1904±4 Ma, whereas similar ages are reported from the Ylöjärvi samples from the Lower Volcanic Unit (1898±4 Ma) and the Upper Volcanic Unit (1889±5 Ma), two feldspar porphyries (1891±16 Ma and 1889±19 Ma) and the Värmälä granitoid (1901±28 Ma). The Rb-Sr whole-rock ages of the volcanics, in spite of the large errors, were in concordance with the U-Pb zircon ages. It is obvious that a clear correlation can be established between the results of this study and those of Kähkönen et al. (1989) and Talikka and Mänttäri (2005). In consequence, it is inferred that Koskuenjärvi volcanics formed at c. 1.90 Ga in an island-arc or fore-arc setting (Kähkönen et al. 1989), followed by the emplacement of Pukala intrusion c. 1.89 Ga, during subduction or at the early stages of collision between island-arcs or an island-arc and a continental margin, causing hydrothermal alteration of the rocks at Kutemajärvi (Talikka and Mänttäri 2005, Talikka 2007).

The timing of hydrothermal alteration caused by the emplacement of the Pukala intrusion is also consistent with the average model age of a galena (1888 Ma) from sample A1447 (Mänttäri et al. 1997). The Pukala intrusion is viewed as the putative source of metals and hydrothermal fluids that induced the formation of the Kutemajärvi epithermal gold deposit. This is corroborated by the presence of comb quartz in the contact of the intrusion and the altered rocks, the ubiquitous presence of F-rich minerals, especially fluorite and topaz, as well as the pervasively intense chlorite, sericite, and quartz ± advanced argillic alteration that necessitates the existence of a magmatic source at depth, capable of sustaining an extensive hydrothermal system (Eilu 2003, Talikka and Mänttäri 2005, Talikka 2007, Kinnunen 2008). This supposition, nevertheless, comes into conflict with the model presented by Poutiainen and Grönholm (1996). On the basis of fluid inclusion studies, they argue that the hydrothermal fluids derived from devolatilization of the lower crust during the metamorphism of the Tampere Schist Belt and a subsequent thermal event occurred at low temperatures and pressures, resulting into secondary enrichment and remobilization of the ore by diluted aqueous solutions. However, fluid inclusion records are hardly preserved during a superimposing greenschist to amphibolite facies metamorphic event, in which the primary magmatic-hydrothermal minerals are recrystallized. As a result, Poutiainen and Grönholm (1996) most likely recorded the conditions of metamorphic overprint in their fluid inclusion studies. On the other hand, Kinnunen (2008) reports no evidence of major scale enrichment or remobilization of gold.

Other examples of Paleoproterozoic metamorphosed porphyry and epithermal deposits in the greater area of Fennoscandia are the Enåsen gold deposit in central Sweden (Hallberg 1994, Hallberg and Fallick 1994) and the Boliden Au-Cu-As deposit in the Skellefte District in northern Sweden which formed at 1.86–1.85 Ga (Weihed et al. 1996). In the northern part of Swedish Lapland also lies the Aitik Cu-Au-Ag deposit that is considered as a porphyry deposit, associated with the emplacement of a quartz monzodiorite at c. 1.89 Ga (Wanhainen et al. 2012). In the Tampere and Uusimaa belts, the Järveenpää Au-Ag-base metal and Isovesi Au prospects are also classified as metamorphosed epithermal Au occurrences (Eilu, 2015, Haapala and Rämö, 2015). Another example from the Tampere Schist Belt and in a close distance to the Kutemajärvi deposit, is the Ylöjärvi porphyry W-Cu-Sn-Au deposit, hosted in a tourmaline breccia and linked to the 1.88 Ga Hämeenkyrö granodiorite batholith. The similar ages of the Ylöjärvi granitoids and the tourmaline breccias, the structure and texture of the tourmaline breccia, as well as the ore mineral assemblage support the idea that explosion of mineralizing hydrothermal fluids, derived from the crystallizing Hämeenkyrö pluton, are responsible for the formation of the tourmaline breccia, a process which is documented in the case of the Chilean tourmaline breccia pipes of the Central Andes (Haapala and Rämö, 2015). The southeastern margin of the breccia is a shear zone that may have controlled the explosion and migration of the mineralizing fluids that generated the Ylöjärvi deposit (Nironen, 1989). The Tampere Schist Belt consists of several other magmatic-hydrothermal prospects, such as the Tammijärvi Sn-W prospect in the Luhanka municipality (Haapala and Rämö, 2015). In southwestern Finland, the Forssa-Jokioinen ore province of the Häme belt hosts the Kedonojankulma Cu-Mo-Au deposit that is related to a 1.88 Ga syn-orogenic tonalite-granite porphyry intrusion. The geochemical affinities and the vein system of the Kedonojankulma Cu-Mo-Au deposit share many similarities to porphyry copper systems, while the presence of a lithocap supports the potential of preserved epithermal gold mineralization zones in the volcanic rocks surrounding the intrusion (Tiainen et al. 2013). In addition, the Kedonojankulma deposit resembles the Kopsa porphyry Cu-Au deposit of central Finland (Tiainen et al. 2012, Eilu, 2015). However, recent evidence, such as the low gold grade, the synchronicity of the mineralization and the emplacement of its granitoid host, the presence of shearing in the ore and the fact that the deposit is hosted by a granitoid in an orogenic belt advocate in favor of classification of the Kopsa deposit as an intrusion-related gold deposit (Eilu, 2015).

5.2.3. Syn-collision events

A landmark in the geological history of the Tampere Schist Belt and southwestern Finland in general is the main collisional stage of the Svecofennian orogeny that culminated with metamorphism and deformation between 1.89–1.88 Ga (Kähkönen et al. 1989, Nironen 1989, Kilpeläinen et al. 1994, Kilpeläinen, 1998, Kähkönen 1999, Mouri et al. 1999, Eilu et al. 2003, Talikka and Mänttäri 2005, Talikka 2007, Lahtinen et al. 2009, Kalliomäki et al. 2014, Kara et al. 2021). Peak metamorphism in the Svecofennian Tonalite-Trondhjemite Migmatite Belt is determined at 1878.5±1.5 (Mouri et al. 1999). In the Tampere Schist Belt, the main D_2 deformation stage is expressed with the development of east-west striking faults and subvertical foliation, large shear zones and formation of a large synform that probably represents a folded early thrust. (Kähkönen 1989, Nironen 1989, Kilpeläinen 1998, Kähkönen 2005). Moreover, the syn-orogenic Hämeenkyrö granodiorite batholith and Värmälä granodiorite stock intruded the Svecofennian supracrustal rocks of the Tampere Schist Belt at 1885±2 Ma and 1878±3 Ma, respectively, whereas the 1.86 Ga age of uraninite from a tourmaline breccia of the Ylöjärvi deposit reflects a retrogressive tectonothermal stage (Nironen 1989). As a consequence, during this major collisional event, which is ubiquitous all over the Central Svecofennian Arc Complex, peak metamorphism was contemporaneous with the syn-collisional magmatism that engendered the large plutonic bodies of the Central Finland Granitoid Complex. In contrast, in the Southern Svecofennian Arc Complex the 1.91–1.88 Ga early phase of plutonism is coeval with volcanism, whereas syn-orogenic magmatism began approximately 10 Ma earlier than in the Central Svecofennian Arc Complex at 1.88–1.86 Ga (Nironen 1997, Korsman et al. 1999, Rämö et al. 2001, Väisänen et al. 2002, Saalmann et al. 2009). The collision of the Central Svecofennian Arc Complex with the Southern Svecofennian Arc Complex transpired at 1.88–1.86 Ga, about 10 to 20 Ma later after the collision of the former with the Archean Karelian craton (Väisänen et al. 2002). Mänttäri et al. (1997) reported the U-Pb age of monazite of sample A1447 at 1879±2 Ma based on the air-abraded monazite fraction, whereas the HF-leached monazite fraction yielded a 1850±2 Ma. U-Pb dating of sample A1447, which was reanalyzed in this study, demonstrated similar ages for three monazite grains (1873±20 Ma, 1875±21 Ma, 1878±26 Ma) of the same sample, despite the high 1σ error. Furthermore, U-Pb results for the reanalyzed zircon of sample A1447 reveals a second population with a concordia age of 1873.8±8.9 Ma. U-Pb monazite ages, produced from

samples 31-0-1 KOH-8 95.20, 31-0-1 KOH-15 146.20 and KU-567 243.20, fall within the same time span, whilst the obtained ages of the distinct monazite populations of samples ORV KU-543 and Sarvisuo IIA are 1877.6±4.0 Ma and c. 1870 Ma, respectively. Thus, the 1.89–1.87 Ga time interval marks the main regional metamorphic and deformation phase (D_2), during which the Kutemajärvi gold deposit was subjected to greenschist to lower-amphibolite facies metamorphism, and compressional deformation (Poutiainen and Grönholm 1996, Eilu et al 2003, Talikka and Mänttäri 2005, Talikka 2007, Kinnunen 2008). The intense deformation resulted in the formation of large isoclinal folds and rotation of the deposit alongside the Pukala intrusion with its roof facing south (Talikka and Mänttäri 2005, Talikka 2007, Kinnunen 2008).

5.2.4. Post-collision events

Several monazite and zircon crystals from the samples of Kutemajärvi gold deposit of this study and from the reanalyzed sample A1447 of Mänttäri et al. (1997) are dated between 1.87 Ga and 1.83 Ga which marks the post-collisional stage of the Central Svecofennian Arc Complex. This time period also corresponds to the D_3 deformation stage of the tectonic evolution of the area and is evidenced by features such as fracturing, kink-folding and movement along narrow shear zones (Nironen, 1989, Kilpeläinen, 1998, Talikka, 2007). Talikka and Mänttäri (2005) interpret the titanite U-Pb age of 1851±5 Ma for the granodiorite sample A1675 of the Pukala intrusion as a posterior local cooling after the emplacement of the intrusion and the ensuing peak metamorphism. This age is comparable to the Rb-Sr whole rock isochron age of 1847±92 Ma for the Orivesi volcanics that is attributed to late metamorphism and slow cooling (Kähkönen et al. 1989) and possibly represents the late post-collision stage of the area. Apart from the previous ages, this study has revealed ages that span between 1.83 Ga and 1.78 Ga. Admittedly, the boundary of the two time periods at c. 1.84–1.83 Ga points to the peak metamorphism in the Southern Svecofennian Arc Complex and postdates the former collision event between the two terranes. This orogenic episode is widespread in the late Svecofennian granite-migmatite zone of southern Finland (Ehlers et al. 1993) and ignited granulite facies metamorphism, migmatization and anatectic granitic melts, the generation of which was sustained until c. 1.80–1.78 Ga (Nironen 1997, Väisänen et al. 2002). In the Uusimaa Belt, granitic magmatism and migmatization started before ~1845 Ma and climaxed at

~1835–1825 Ma (Skyttä and Mänttäri 2008). The leucogranites of southern Finland intruded between ≥1.85 Ga and ~1.79 Ga, thereby overlapping with the syn-, late-, and post-orogenic stages of the Southern Svecofennian Arc Complex (Kurhila et al. 2011). Post-collisional magmatism is also recorded at the margin of the Karelian craton which is expressed with the emplacement of shoshonitic lamprophyres at c. 1.79–1.78 Ga (Woodard et al. 2014). During the time interval of c. 1.83–1.78 Ga, orogenic gold mineralization events accompanied the syn- and post-collisional magmatism in southern Finland. Dating of samples, collected from two gold prospects in the Somero-Tammela gold zone of the Häme belt, gave a U-Pb zircon age of 1832±15 Ma, which is reportedly the maximum mineralization age, whereas the 1.78 and 1.76 Ga ^{39}Ar-^{40}Ar biotite cooling ages provided a minimum age for the mineralization (Saalmann et al. 2009). The same minimum mineralization age of c. 1.80–1.79 Ga has been found for the Jokisivu orogenic gold deposit, in the border zone between the Pirkanmaa and the Häme belts, but the maximum age in that case was c. 1.88 Ga, as indicated by U-Pb dating of the quartz diorite host rocks. The 1.80–1.79 Ga age of mineralization, nonetheless, is reinforced by the ore zone fabrics, which post-date regional-scale folding and the metamorphic peak, and are correlated with the late Svecofennian shear tectonics of the 1.83–1.78 Ga period (Saalmann et al. 2010). Although, the boundary of the two belts, at which the Jokisivu deposit lies, is not well defined, it marks the suture zone of the terranes of the Central Svecofennian and Southern Svecofennian Arc complexes and may constitute the missing link that explains the presence of structurally-controlled gold occurrences in the Häme belt (Saalmann 2007) and the absence of orogenic gold in the Uusimaa belt (Saalmaan et al. 2010).

5.2.5. Distant events of post-orogenic activity

The last set of geochronological data includes monazite and to a lesser extent zircon ages from samples from Kutemajärvi gold deposit, and a few scattered ages from the reanalyzed sample A1447 of Mänttäri et al. (1997), which yield ages between 1.78 Ga and c. 1.54 Ga. Although, these ages mainly represent discordant unfiltered data, they may have significant implications about the tectonic evolution of the area. During that time period, Fennoscandia underwent large-scale crustal thinning which resulted in extensive rapakivi magmatism. Rämö and Haapala (2005) postulate that rapakivi magma was generated in response to magmatic underplating and partial melting of the lower crust

in an extensional tectonic regime. Nonetheless, the driving force that caused the extension is still debatable and a number of feasible scenarios have been proposed that involve active or passive rifting, extensional orogenic collapse, or deep mantle plumes (Haapala and Rämö 1999). The rapakivi complexes define an anorogenic magmatic province that encompasses parts of central Sweden, southern Finland, the Baltic countries and Russian Karelia and consist of four large granitic batholiths (Wiborg, Åland, Laitila, and Vehmaa). The rapakivi granites are spatially and temporally associated with smaller gabbroic and anorthositic bodies, including tholeitic diabase dike swarms (Rämö and Haapala 2005). Dating of the rapakivi intrusions demonstrates that magmatism occurred in two distinct pulses. The oldest of the two magmatic pulses ranges between 1.65 Ga and 1.62 Ga, whereby the Wiborg batholith, and the Ahvenisto and Suomenniemi complexes of southeastern Finland were emplaced. The intrusion of the Häme diabase dike swarm, which extends from the Wiborg batholith to the Kutemajärvi area, commenced somewhat earlier at around 1.67 Ga. By contrast, the ages of the rapakivi plutons of southwestern Finland are determined at around 1.59 to 1.54 Ga (Vaasjoki et al. 1991, Alviola et al. 1999, Rämö and Haapala 2005, Rämö and Mänttäri 2015). In the Kutemajärvi area, a 1.5 Ga brannerite/thucholite age from an andalusite-muscovite breccia and a 1.0 Ga thucholite age from a muscovite are construed as retrograde metamorphic events related to the intrusion of rapakivi granites and the Grenvillian orogeny, respectively (Kinnunen 2008). The aforementioned observations signify that the entire Svecofennian domain remained overly disquieted throughout its intricate tectonometamorphic evolution. Hence, it is conceivable that the 1.78–1.54 Ga ages of the current study reflect the waning stages of the post-orogenic activity of southern Svecofennia and rapakivi magmatism in the region of Kutemajärvi. Geochronological data and ages of the most important geotectonic events for the Kutemajärvi gold deposit, the Tampere Schist Belt, and the Southern Svecofennian Arc Complex, which are referred to in the previous section, are summarized in Figures 37 and 38 below.

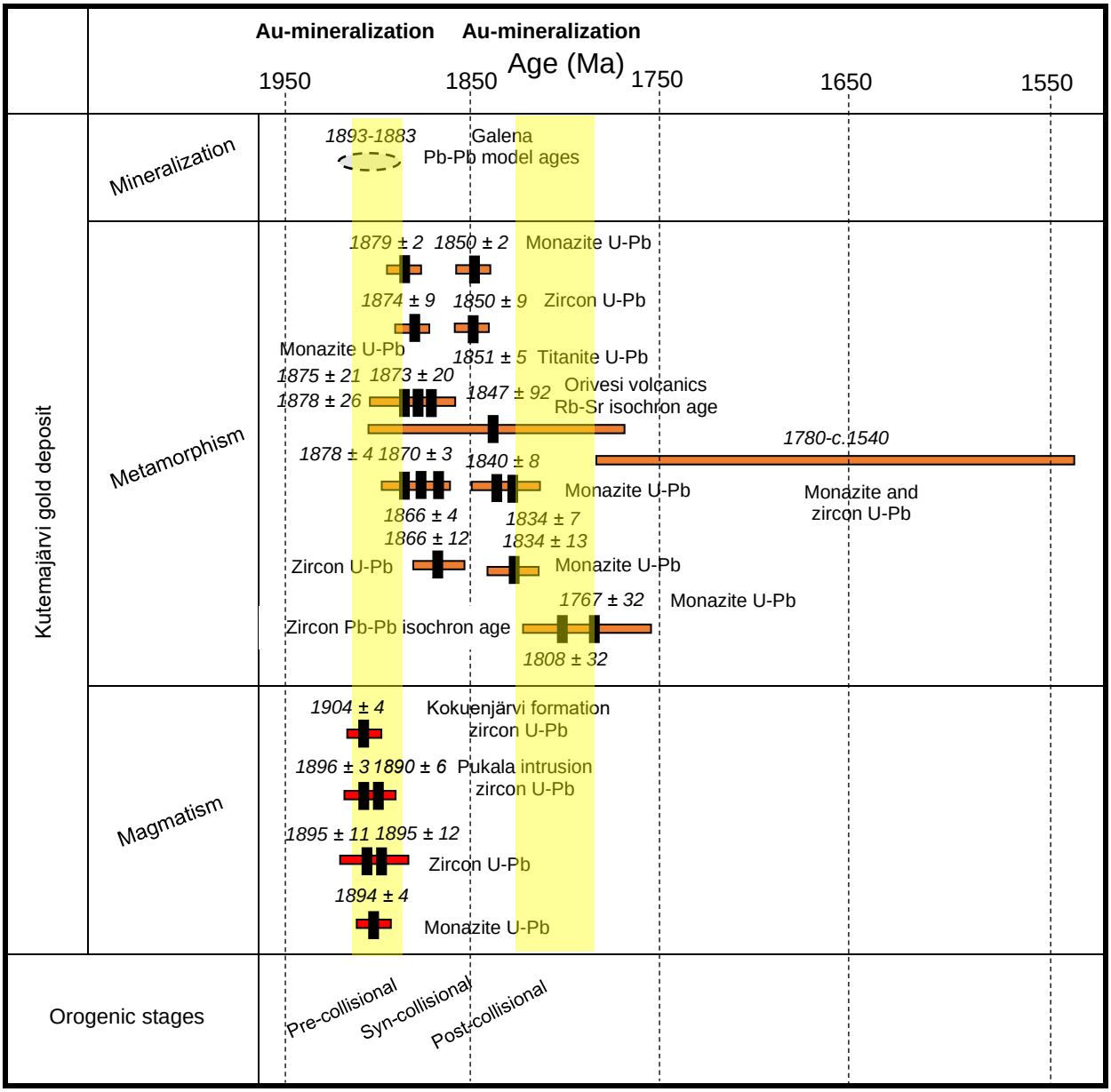

Figure 37. Summary of geochronological data and ages of magmatism and metamorphism for the Kutemajärvi gold deposit.

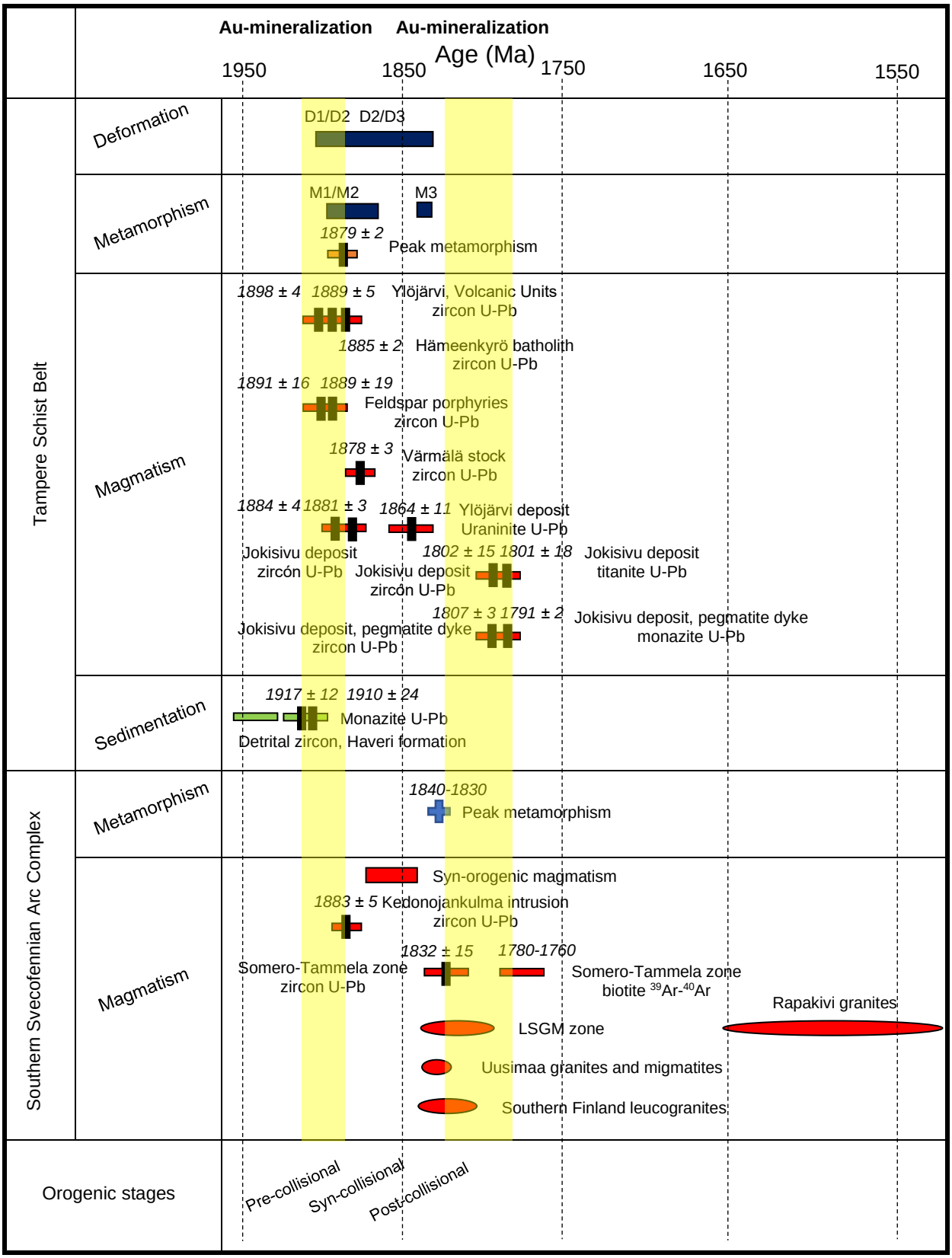

Figure 38. Summary of geochronological data ages of magmatism, metamorphism and deformation events for the Tampere Schist Belt and the Southern Svecofennian Arc Complex in the framework of the Svecofennian orogeny.

6. Conclusions

The current study provides a comprehensive geochronological dataset of the magmatic and hydrothermal processes that took place in the Kutemajärvi gold deposit, in the eastern part of the Tampere Schist Belt. According to the SEM results, two types of monazite grains have been identified: metamorphic monazite which displays strain shadow and hydrothermal monazite, characterized by a large number of interior inclusions. Zircons are also divided into magmatic, metamorphic, and hydrothermal grains. The new U-Pb data for monazite and zircon grains, in conjunction with earlier published geochronological data, suggests that the geodynamic evolution of the area of Kutemajärvi can be described in four distinct stages.

Rifting along the southern margin of a composite continental mass, formed during older Paleoproterozoic orogenic episodes, led to the opening of the Tampere basin at ~1.92 Ga. This stage is marked by the deposition of the Haveri formation in a back-arc or marginal basin that evolved to a mature basin, along with detrital material from the uplifted orogen as indicated by Archean and >1.91 Ga ages. The opening of the Tampere basin is followed by subduction of oceanic crust under island-arc or active continental margin, resulting in volcanism which is expressed with the extrusion of the Koskuenjärvi formation at 1904 Ma. At the late stages of subduction or at the early-collision stage (1900–1890 Ma) between island-arcs or an island-arc and a continental margin, continued volcanism gave rise to the emplacement of the Pukala porphyry intrusion at hypabyssal depths around 1890 Ma which provides the maximum age of mineralization. Crystallization of the intrusion released hydrothermal fluids that caused pervasive hydrothermal alteration of the Kutemajärvi host rocks and deposition of gold alongside other metals.

Subsequently, during the syn-collision stage at 1890–1878 Ma, the Pukala intrusion and the Kutemajärvi hydrothermally altered domain experienced compressional deformation and greenschist to lower amphibolite facies metamorphism, which reached its peak at 1880–1878 Ma. Metamorphism also resulted in overprinting of the early deposited epithermal gold by metamorphic fluids, generated by devolatilization of the Svecofennian lower crust. The metamorphic peak is recorded by abundant metamorphic monazite and zircon grains from host rocks of Kutemajärvi which ages fall within this time-interval and provides the minimum age of mineralization. This profound orogenic event typifies the culmination of Svecofennian orogeny that left its footprint over a wide

area and induced the emplacement of the synorogenic granitoids that constitute the Central Finland Granitoid Complex. Furthermore, at 1880–1860 Ma occurred the collision between the Central Svecofennian Arc Complex and the Southern Svecofennian Arc Complex.

After the consummation of the Svecofennian orogeny in the Tampere Schist Belt, the orogenetic front migrated southward, where Southern Svecofennia reached its metamorphic peak at 1.83 Ga, and induced concurrent syn-orogenic magmatism that lasted until 1.78 Ga. It is evident from younger generations of monazite and zircon grains from Kutemajärvi that the latter and its vicinity were perturbed by retrograde metamorphic and regional cooling events. The ages of these grains record the prolonged post-collisional stage and implicate repeated tectonothermal activity in the region that can be affiliated to the syn- and post-collisional magmatism of the Southern Svecofennian Arc Complex and the intrusion of rapakivi granites of southern Finland. Age constraints for the mineralization in Kutemajärvi utilizes U-Pb dating of single monazite and zircon grains and attempts to collate the obtained ages with those of previously published studies, in order to establish a spatial and temporal framework with respect to the tectonometamorphic evolution of the Kutemajärvi gold deposit and the Tampere Schist Belt. The results of this study also contribute to distinguishing magmatic, metamorphic, and hydrothermal events that lay the groundwork for an effective assessment of mineral prospectivity and the potential location of other epithermal deposits in the metamorphic terranes of the Svecofennian domain in southern Finland.

Acknowledgements

First and foremost, I would like to express my profound gratitude to my supervisors, Petri Peltonen (Professor of Practice, University of Helsinki, PhD, MAusIMM (CP)) and Férenc Molnár (Research Professor, Geological Survey of Finland and Associate Professor, Department of Mineralogy, Faculty of Natural Sciences, Eötvös Loráns University) for their guidance, constructive remarks and insightful corrections during the implementation of this Master's Thesis. Matti Talikka (M.Sc., FAusIMM (CP)) is greatly acknowledged for providing the polished thin sections used for microscopical analysis and U-Pb dating. Sari Lukkari (Geological Survey of Finland) and Matti Kurhila (Geological Survey of Finland) are thanked for their contribution with reference to the

SEM analysis and U-Pb dating, respectively. Special thanks to Miguel Francisco Aldana Paéz, Dovydas Kičiatovas and Nikolaos Karampelas for making my life in Helsinki more pleasant, during the challenging times of the pandemics. Finally, I would like to thank my family for their profuse moral and psychological support that assisted me in fulfilling my dream of conducting my postgraduate studies in Finland.

REFERENCES

Achterberg, E. Ryan, C. Jackson, S. and Griffin, W. 2001. Data reduction software for LA-ICP-MS. In: Sylvester, P. (Ed.) Laser-Ablation ICPMS in the Earth Sciences-Principles and applications. Mineralogical Association of Canada short course series, Volume 29, Ottawa, Ontario, Canada, 239-243.

Alviola, R., Johanson, B. S., Rämö, O. T. and Vaasjoki, M. 1999. The Proterozoic Ahvenisto rapakivi granite–massif-type anorthosite complex, southeastern Finland; petrography and U–Pb chronology. Precambrian Research 95, 89-107.

Ayers, J., Loflin, M., Miller, C., Barton, M., Coath, C., Wanty, R., and Seal, R. 2004. Dating fluid infiltration using monazite. In: Wanty, R.B. and Seal II, R.R. (Eds.) Water-Rock Interaction. Proceedings of the Eleventh International Symposium on Water-Rock Interaction WRI-11, Saratoga Springs, New York, USA, 27 June-2 July 2004. Volume 1, AA Balkema Publishers, 247-251.

Barra, F., Ruiz, J., Mathur, R. and Titley, S. 2003. A Re–Os study of sulfide minerals from the Bagdad porphyry Cu–Mo deposit, northern Arizona, USA. Mineralium Deposita 38, 585-596.

Belousova, E.A., Griffin, W.L. and O'Reilly, S.Y. 2005. Zircon Crystal Morphology, Trace Element Signatures and Hf Isotope Composition as a Tool for Petrogenetic Modelling: Examples From Eastern Australian Granitoids. Journal of Petrology 47, 329-353.

Berger, A., Gnos, E., Janots, E., Fernandez, A. and Giese, J. 2008. Formation and composition of rhabdophane, bastnäsite and hydrated thorium minerals during alteration: Implications for geochronology and low-temperature processes. Chemical Geology 254, 238-248.

Cabral, A.R., Eugster, O., Brauns, M., Lehmann, B., Rösel, D., Zack, T., de Abreu, F.R., Pernicka, E. and Barth, M. 2013. Direct dating of gold by radiogenic helium: Testing the method on gold from Diamantina, Minas Gerais, Brazil: Geology 41, 163-166.

Chen, L., Xu, J. and Chen, J. 2015. Applications of scanning electron microscopy in earth sciences. Science China Earth Sciences 58, 1768-1778.

Deng, X.-H., Wang, J.-B., Pirajno, F., Wang, Y.-W., Li, Y.-C., Li, C., Zhou, L.-M. and Chen, Y.-J. 2016. Re–Os dating of chalcopyrite from selected mineral deposits in the Kalatag district in the eastern Tianshan Orogen, China. Ore Geology Reviews 77, 72-81.

Dowling, K. and Morrison, G. 1989. Application of Quartz Textures to the Classification of Gold Deposits Using North Queensland Examples. In: Keays, R.R., Ramsay, W.R.H. and Groves, D.I. (Eds.) The Geology of Gold Deposits: The Perspective in 1988. Society of Economic Geologists, 342-355.

Ehlers, C., Lindroos, A. and Selonen, O. 1993. The late Svecofennian granite-migmatite zone of southern Finland—a belt of transpressive deformation and granite emplacement. Precambrian Research 64, 295-309.

Eilu, P. 2015. Overview on Gold Deposits in Finland. In: Maier, W.D., Lahtinen, R. and O'Brien, H. (Eds.) Mineral Deposits of Finland. Elsevier, 377-410.

Eilu, P., Sorjonen-Ward, P., Nurmi, P. and Niiranen, T. 2003. A Review of Gold Mineralization Styles in Finland. Economic Geology 98, 1329-1353.

Feng, C., Qu, W., Zhang, D., Dang, X., Du, A., Li, D. and She, H. 2009. Re–Os dating of pyrite from the Tuolugou stratabound Co(Au) deposit, eastern Kunlun Orogenic Belt, northwestern China. Ore Geology Reviews 36, 213-220.

Fielding, I.O.H., Johnson, S.P., Zi, J.-W., Rasmussen, B., Muhling, J.R., Dunkley, D.J., Sheppard, S., Wingate, M.T.D. and Rogers, J.R. 2017. Using In Situ SHRIMP U-Pb Monazite and Xenotime Geochronology to Determine the Age of Orogenic Gold Mineralization: An Example from the Paulsens Mine, Southern Pilbara Craton. Economic Geology 112, 1205-1230.

Fielding, I.O.H., Johnson, S.P., Zi, J.-W., Sheppard, S. and Rasmussen, B. 2018. Neighbouring orogenic gold deposits may be the products of unrelated mineralizing events. Ore Geology Reviews 95, 593-603.

Frelinger, S.N., Ledvina, M.D., Kyle, J.R. and Zhao, D. 2015. Scanning electron microscopy cathodoluminescence of quartz: Principles, techniques and applications in ore geology. Ore Geology Reviews 65, 840-852.

Freydier, C., Ruiz, J., Chesley, J., McCandless, T. and Munizaga, F. 1997. Re-Os isotope systematics of sulfides from felsic igneous rocks: Application to base metal porphyry mineralization in Chile. Geology 25, 775-778.

Haapala, I. and Rämö, O. T. 1999. Rapakivi granites and related rocks: an introduction. Precambrian Research 95, 1-7.

Haapala, I and Rämö, O. T. 2015. Mineral Deposits Related to Granitic Rocks. In: Maier, W.D., Lahtinen, R. and O'Brien, H. (Eds.) Mineral Deposits of Finland. Elsevier, 531-556.

Hallberg, A. 1994. The Enåsen gold deposit, central Sweden. Mineralium Deposita 29, 150-162.

Hallberg, A. and Fallick, A.E. 1994. The Enåsen gold deposit, central Sweden. Mineralium Deposita 29, 163-169.

Hedenquist, J.W., Arribas A.R. and Gonzalez-Urien, E. 2000. Exploration for Epithermal Gold Deposits. In: Hagemann, S.G. and Brown, P.E. (Eds.) Gold in 2000. Reviews in Economic Geology 13. Society of Economic Geologists, 245-277.

Hetherington, C.J., Harlov, D.E. and Budzyń, B. 2010. Experimental metasomatism of monazite and xenotime: mineral stability, REE mobility and fluid composition. Mineralogy and Petrology 99, 165-184.

Hnatyshin, D., Creaser, R.A., Wilkinson, J.J. and Gleeson, S.A. 2015. Re-Os dating of pyrite confirms an early diagenetic onset and extended duration of mineralization in the Irish Zn-Pb ore field. Geology 43, 143-146.

Hölttä, P., Huhma, H., Mänttäri, I. and Paavola, J. 2000. P–T–t development of Archaean granulites in Varpaisjärvi, Central Finland: II. Dating of high-grade metamorphism with the U–Pb and Sm–Nd methods. Lithos 50, 121-136.

Hu, R.-Z., Burnard, P.G., Bi, X.-W., Zhou, M.-F., Pen, J.-T., Su, W.-C. and Wu, K.-X. 2004. Helium and argon isotope geochemistry of alkaline intrusion-associated gold and copper deposits along the Red River–Jinshajiang fault belt, SW China. Chemical Geology 203, 305-317.

Hu, R.-Z., Burnard, P.G., Bi, X.-W., Zhou, M.-F., Peng, J.-T., Su, W.-C. and Zhao, J.-H. 2009. Mantle-derived gaseous components in ore-forming fluids of the Xiangshan uranium deposit, Jiangxi province, China: Evidence from He, Ar and C isotopes. Chemical Geology 266, 86-95.

Huhma, H., Claesson, S., Kinny, P.D. and Williams, I.S. 1991. The growth of Early Proterozoic crust: new evidence from Svecofennian detrital zircons. Terra Nova 3, 175-178.

Huhma, H., Mänttäri, I., Peltonen, P., Kontinen, A., Halkoaho, T., Hansi, E., Hokkanen, T., Hölttä, P., Juopperi, H., Konnunaho, J., Layahe, Y., Luukonen, E., Pietikäinen, K., Pulkkinen, A., Sorjoinen-Ward, P., Vaasjoki, M. and Whitehouse, M. 2012. The age of the Archaean greenstone belts in Finland. Geological Survey of Finland, Special Paper 54, 73-174.

Kähkönen, Y. 1987. Geochemistry and tectonomagmatic affinities of the metavolcanic rocks of the early proterozoic tampere schist belt, Southern Finland. Precambrian Research 35, 295-311.

Kähkönen, Y. 1989. Geochemistry and petrology of the metavolcanic rocks of the early Proterozoic Tampere Schist Belt, southern Finland. Geological Survey of Finland, Bulletin 345, 104 pp.

Kähkönen, Y. 1999. Stratigraphy of the central parts of the Palaeoproterozoic Tampere Schist Belt, southern Finland: Review and revision. Bulletin of the Geological Society of Finland 71, 13-29.

Kähkönen, Y. 2005. Svecofennian supracrustal rocks. In: Lehtinen, M., Nurmi, P.A., and Rämö, O.T. (Eds.) Developments in Precambrian Geology 14, Elsevier, 343-405.

Kähkönen, Y. and Huhma, H. 1993. An Archean Cobble In A Svecofennian Conglomerate Near Tampere, Southern Finland. Geological Survey of Finland, Special Paper 18, 31-36.

Kähkönen, Y., Huhma, H. and Aro, K. 1989. U-Pb zircon ages and Rb-Sr whole-rock isotope studies of early Proterozoic volcanic and plutonic rocks near Tampere, southern Finland Precambrian Research 45, 27-43.

Kähkönen, Y. and Nironen, M. 1994. Supracrustal Rocks Around The Paleoproterozoic Haveri Au-Cu Deposit, Southern Finland: Evolution From a Spreading Center To A Volcanic Arc Environment. Geological Survey of Finland, Special Paper 19, 141-159.

Kalliomäki, H., Torvela, T., Moreau, J. and Kähkönen, Y. 2014. Relationships between basin architecture, basin closure, and occurrence of sulphide-bearing schists: an example from Tampere Schist Belt, Finland. Journal of the Geological Society 171, 659-671.

Käpyaho, A., Molnár, F., Sorjonen-Ward, P., Mänttäri, I., Sakellaris, G. and Whitehouse, M.J. 2017. New U-Pb age constraints for the timing of gold mineralization at the Pampalo gold deposit, Archaean Hattu schist belt, eastern Finland, obtained from hydrothermally altered and recrystallised zircon. Precambrian Research 289, 48-61.

Kara, J., Leskelä, T., Väisänen, M., Skyttä, P., Lahaye, Y., Tiainen, M. and Leväniemi, H. 2021. Early Svecofennian rift-related magmatism: Geochemistry, U-Pb-Hf zircon isotope data and tectonic setting of the Au-hosting Uunimäki gabbro, SW Finland. Precambrian Research 364, p. 106364.

Kendrick, M.A., Burgess, R., Pattrick, R.A.D. and Turner, G. 2001. Fluid inclusion noble gas and halogen evidence on the origin of Cu-Porphyry mineralising fluids. Geochimica et Cosmochimica Acta 65, 2651-2668.

Kilpeläinen, T. 1998. Evolution and 3D modelling of structural and metamorphic patterns of the Palaeoproterozoic crust in the Tampere-Vammala area, southern Finland. Geological Survey of Finland, Bulletin 397, 124 pp.

Kilpeläinen, T., Korikovsky, S., Korsman, K. and Nironen, M. 1994. Tectono-Metamorphic Evolution In The Tampere-Vammala Area. In: Pajunen, M. (Ed.) High temperature-low pressure metamorphism and deep crustal structures. Meeting of IGCP project ”Deep Crustal Processes” in Finland, September 16-20, 1994. Geological Survey of Finland, Guide 37, 27-34.

Kinnunen, A. 2008. A Palaeoproterozoic high-sulphidation epithermal gold deposit at Orivesi, southern Finland. Doctoral Dissertation, University of Oulu, Faculty of Science, Department of Geosciences, 183 pp.

Korsman, K., Korja, T., Pajunen, M., Virransalo, P. and Group, G.S.W. 1999. The GGT/SVEKA Transect: Structure and Evolution of the Continental Crust in the Paleoproterozoic Svecofennian Orogen in Finland. International Geology Review 41, 287-333.

Kurhila, M., Mänttäri, I., Vaasjoki, M., Rämö, T.O. and Nironen, M. 2011. U–Pb geochronological constraints of the late Svecofennian leucogranites of southern Finland. Precambrian Research 190, 1-24.

Lahtinen, R. and Huhma, H. 1997. Isotopic and geochemical constraints on the evolution of the 1.93-1.79 Ga Svecofennian crust and mantle in Finland. Precambrian Research 82, 13-34.

Lahtinen, R., Huhma, H., Kähkönen, Y. and Mänttäri, I. 2009. Paleoproterozoic sediment recycling during multiphase orogenic evolution in Fennoscandia, the Tampere and Pirkanmaa belts, Finland. Precambrian Research 174, 310-336.

Liu, Z., Mao, X., Ackerman, L., Li, B., Dick, J.M., Yu, M., Peng, J. and Shahzad, S.M. 2020. Two-stage gold mineralization of the Axi epithermal Au deposit, Western Tianshan, NW China: Evidence from Re–Os dating, S isotope, and trace elements of pyrite. Mineralium Deposita 55, 863-880.

Ludwig, K. R. 2003. Isoplot 3.0: A Geochronological Toolkit for Microsoft Excel. Berkeley Geochronology Center Special Publication 4.

Luukkonen, A. 1994. Main Geological Features, Metallogeny And Hydrothermal Alteration Phenomena Of Certain Gold and Gold-Tin-Tungsten Prospects in Southern Finland. Geological Survey of Finland, Bulletin 377, 153 pp.

Luukkonen, A., Gronholm, P. and Hannila, T. 1992. Eräiden Etelä-Suomen kulta- ja sen seuralaismetalliesiintymien geologiset pääpiirteet. Summary: Main geological features of certain gold and tungsten-tin-gold prospects in Southern Finland. Geological Survey of Finland, Report of Investigation 113, 90 pp.

Mänttäri, I., Luukkonen, A. and Grönholm, P. 1997. Isotopic Studies On The Kutemajärvi Gold Deposit, Orivesi, Southern Finland. Geological Survey of Finland, Special Paper 23, 55-58.

Márton, I., Moritz, R. and Spikings, R. 2010. Application of low-temperature thermochronology to hydrothermal ore deposits: Formation, preservation and exhumation of epithermal gold systems from the Eastern Rhodopes, Bulgaria. Tectonophysics 483, 240-254.

Mathur, R., Ruiz, J. and Tornos, F. 1999. Age and sources of the ore at Tharsis and Rio Tinto, Iberian Pyrite Belt, from Re-Os isotopes. Mineralium Deposita 34, 790-793.

Mikulski, S.Z., Williams, I.S., Stein, H.J. and Wierchowiec, J. 2020. Zircon U-Pb Dating of Magmatism and Mineralizing Hydrothermal Activity in the Variscan Karkonosze Massif and Its Eastern Metamorphic Cover (SW Poland). Minerals, 10, 787.

Molnár, F., Middleton, A., Stein, H., O`Brien, H., Lahaye, Y., Huhma, H., Pakkanen, L. and Johanson, B. 2018. Repeated syn- and post-orogenic gold mineralization events between 1.92 and 1.76 Ga along the Kiistala Shear Zone in the Central Lapland Greenstone Belt, northern Finland. Ore Geology Reviews 101, 936-959.

Morelli, R., Creaser, R.A., Seltmann, R., Stuart, F.M., Selby, D. and Graupner, T. 2007. Age and source constraints for the giant Muruntau gold deposit, Uzbekistan, from coupled Re-Os-He isotopes in arsenopyrite. Geology 35, 795-798.

Morelli, R.M., Creaser, R.A., Selby, D., Kontak, D.J. and Horne, R.J. 2005. Rhenium-Osmium Geochronology of Arsenopyrite in Meguma Group Gold Deposits, Meguma Terrane, Nova Scotia, Canada: Evidence for Multiple Gold-Mineralizing Events. Economic Geology 100, 1229-1242.

Mortensen, J.K., Craw, D., MacKenzie, D.J., Gabites, J.E. and Ullrich, T. 2010. Age and Origin of Orogenic Gold Mineralization in the Otago Schist Belt, South Island, New Zealand: Constraints from Lead Isotope and 40Ar/39Ar Dating Studies. Economic Geology 105, 777-793.

Mouri, H., Korsman, K. and Huhma, H. 1999. Tectono-metamorphic evolution and timing of the melting processes in the Svecofennian Tonalite-Trondhjemite Migmatite Belt: an example from Luopioinen, Tampere area, southern Finland. Bulletin of the Geological Society of Finland 71, 31-56.

Müller, W., Shelley, M., Miller, P. and Broude, S. 2009. Initial performance metrics of a new custom-designed ArF Excimer LA-ICP-MS system coupled to a two-volume laser-ablation cell. Journal of Analytical Atomic Spectrometry 24, 209-214.

Nironen, M. 1989. Emplacement and structural setting of granitoids in the early Proterozoic Tampere and Savo schist belts, Finland - implications for contrasting crustal evolution. Geological Survey of Finland, Bulletin 346, 83pp.

Nironen, M. 1997. The Svecofennian Orogen: a tectonic model. Precambrian Research 86, 21-44.

Nironen, M., Elliott, B.A. and Rämö, O.T. 2000. 1.88–1.87 Ga post-kinematic intrusions of the Central Finland Granitoid Complex: a shift from C-type to A-type magmatism during lithospheric convergence. Lithos 53, 37-58.

Oelkers, E.H. and Poitrasson, F. 2002. An experimental study of the dissolution stoichiometry and rates of a natural monazite as a function of temperature from 50 to 230 °C and pH from 1.5 to 10. Chemical Geology 191, 73-87.

Pelleter, E., Cheilletz, A., Gasquet, D., Mouttaqi, A., Annich, M., El Hakour, A., Deloule, E. and Féraud, G. 2007. Hydrothermal zircons: A tool for ion microprobe U–Pb dating of gold mineralization (Tamlalt–Menhouhou gold deposit — Morocco). Chemical Geology 245, 135-161.

Phillips, G.N. and Powell, R. 2015. A practical classification of gold deposits, with a theoretical basis. Ore Geology Reviews 65, 568-573.

Pohjolainen, E., Molnar, F., O'Brien, H., Huhma, H., Tiljander, M., Sorjonen-Ward, P., Lukkari, S., Johanson, B. and Talikka, M. 2017. U-Pb geochronology of monazite from the Hangaslampi gold deposit in the Paleoproterozoic Kuusamo schist belt, northern Finland: implications for dating multi-stage mineralizing events. In: Mineral resources to discover. Proceedings of the 14th SGA Biennial Meeting, Québec City, Canada, Volume 3, Society for Geology Applied to Mineral Deposits, 1039-1042.

Poutiainen, M. and Groenholm, P. 1996. Hydrothermal fluid evolution of the Paleoproterozoic Kutemajarvi gold telluride deposit, Southwest Finland. Economic Geology 91, 1335-1353.

Rämö, O.T. and Haapala, I. 2005. Rapakivi Granites. In: Lehtinen, M., Nurmi, P.A., and Rämö, O.T. (Eds.) Developments in Precambrian Geology 14, Elsevier, 533-562.

Rämö, O.T. and Mänttäri, I. 2015. Geochronology of the Suomenniemi rapakivi granite complex revisited: Implications of point-specific errors on zircon U-Pb and refined λ87 on whole-rock Rb-Sr. Bulletin of the Geological Society of Finland 87, 25-45.

Rämö, O.T., Vaasjoki, M., Mänttäri, I., Elliott, B.A. and Nironen, M. 2001. Petrogenesis of the Post-kinematic Magmatism of the Central Finland Granitoid Complex I; Radiogenic Isotope Constraints and Implications for Crustal Evolution. Journal of Petrology 42, 1971-1993.

Rasmussen, B. and Muhling, J.R. 2007. Monazite begets monazite: evidence for dissolution of detrital monazite and reprecipitation of syntectonic monazite during low-grade regional metamorphism. Contributions to Mineralogy and Petrology 154, 675-689.

Ridley, J. 2013, Ore deposit geology. Cambridge University Press. 409 pp.

Robert, F., Poulsen, K.H. and Dubé, B. 1997. Gold Deposits And Their Geological Classification. In: Gubins, A. G. (Ed.) Geophysics and Geochemistry at the Millenium: Proceedings of Exploration 97: Fourth Decennial International Conference on Mineral Exploration, Toronto, Canada, September 14-18, 1997, Prospectors and Developers Association of Canada, 209-220.

Roy, P.S. 1999. Heavy mineral beach placers in southeastern Australia; their nature and genesis. Economic Geology 94, 567-588.

Saalmann, K. 2007. Structural control on gold mineralization in the Satulinmäki and Riukka prospects, Häme belt, southern Finland. Bulletin of the Geological Society of Finland 79, 69-93.

Saalmann, K., Mänttäri, I., Peltonen, P., Whitehouse, M.J., Grönholm, P. and Talikka, M. 2010. Geochronology and structural relationships of mesothermal gold mineralization in the Palaeoproterozoic Jokisivu prospect, southern Finland. Geological Magazine 147, 551-569.

Saalmann, K., Mänttäri, I., Ruffet, G. and Whitehouse, M.J. 2009. Age and tectonic framework of structurally controlled Palaeoproterozoic gold mineralization in the Häme belt of southern Finland. Precambrian Research 174, 53-77.

Salli, I. (Ed.) 1983. Pielavesi. Explanation to the Geological map of Finland 1:100000, pre-Quaternary rocks, sheet 3314. Geological Survey of Finland, Espoo.

Sanematsu, K., Duncan, R., Imai, A. and Watanabe, K. 2005. Geochronological Constraints Using 40Ar/39Ar Dating on the Mineralization of the Hishikari Epithermal Gold Deposit, Japan. Resource Geology 55, 249-266.

Selby, D., Creaser, R.A., Hart, C.J.R., Rombach, C.S., Thompson, J.F.H., Smith, M.T., Bakke, A.A. and Goldfarb, R.J. 2002. Absolute timing of sulfide and gold mineralization: A comparison of Re-Os molybdenite and Ar-Ar mica methods from the Tintina Gold Belt, Alaska. Geology 30, 791-794.

Selby, D., Kelley, K.D., Hitzman, M.W. and Zieg, J. 2009. Re-Os Sulfide (Bornite, Chalcopyrite, And Pyrite) Systematics Of The Carbonate-Hosted Copper Deposits At Ruby Creek, Southern Brooks Range, Alaska. Economic Geology 104, 437-444.

Seydoux-Guillaume, A.-M., Montel, J.-M., Bingen, B., Bosse, V., de Parseval, P., Paquette, J.-L., Janots, E. and Wirth, R. 2012. Low-temperature alteration of monazite: Fluid mediated coupled dissolution–precipitation, irradiation damage, and disturbance of the U–Pb and Th–Pb chronometers. Chemical Geology 330-331, 140-158.

Siani, G.M., Mehrabi, B., Azizi, H., Wilkinson, C.M. and Ganerød, M. 2015. Geochemistry and geochronology of`the volcano-plutonic rocks associated with the Glojeh epithermal gold mineralization, NW Iran. Open Geosciences 7, 207-222.

Sillitoe, R.H. 2010. Porphyry Copper Systems. Economic Geology 105, 3-41.

Simonen, A. 1980. The Precambrian in Finland. Geological Survey of Finland, Bulletin 304, 58 pp.

Skyttä, P. and Mänttäri, I. 2008. Structural setting of late Svecofennian granites and pegmatites in Uusimaa Belt, SW Finland: Age constraints and implications for crustal evolution. Precambrian Research 164, 86-109.

Stacey, J.S. and Kramers, J.D. 1975. Approximation of terrestrial lead isotope evolution by a two-stage model. Earth and Planetary Science Letters 26, 207-221.

Stein, H.J., Sundblad, K., Markey, R.J., Morgan, J.W. and Motuza, G. 1998. Re-Os ages for Archean molybdenite and pyrite, Kuittila-Kivisuo, Finland and Proterozoic molybdenite, Kabeliai, Lithuania: testing the chronometer in a metamorphic and metasomatic setting. Mineralium Deposita 33, 329-345.

Steven, N., Creaser, R., Wulff, K., Kisters, A., Eglington, B. and Miller, J. 2014. Implications of high-precision Re-Os molybdenite dating of the Navachab orogenic gold deposit, Namibia. Geochemistry: Exploration, Environment, Analysis 15, 125-130.

Talikka, M. 2007. Tectonic evolution of the Paleoprotezoic Tampere Belt during the Svecofennian orogeny, with reference to hydrothermal alteration at Kutemajärvi: Au-Ag telluride-selenide deposits. Geological Survey of Finland, Guide 53, 71-77.

Talikka, M. and Manttari, I. 2005. Pukala intrusion, its age and connection to hydrothermal alteration in Orivesi, southwestern Finland. Bulletin of the Geological Society of Finland 77, 165-180.

Tiainen, M., Kärkkäinen, E., Koistinen, J., Lohva, J., Sipilä, P. and Huhta, P. 2012. Discovery of the Kedonojankulma Cu-Au occurrence, hosted by a Svecofennian porphyritic granitoid in Southern Finland. In: Grönholm, S. and Kärkkäinen, N. (Eds.) Gold in Soutern Finland: Results of GTK studies 1998-2011. Geological Survey of Finland, Special Paper 52, 73-90.

Tiainen, M., Molnár, F. and Koistinen, E. 2013. The Cu-Mo-Au mineralization of the Paleoproterozoic Kedonojankulma intrusion, Häme belt, Southern Finland. In: Jonsson, E. et al. (Ed.) Mineral Deposit Research for a high-tech world. Proceedings of the 12th Biennial SGA Meeting, 12-15 August 2013, Uppsala, Sweden, Volume 2, Society for Geology Applied to Mineral Deposits, 892-895.

Vaasjoki, M., Rämö, T.O. and Sakko, M. 1991 New U-Pb ages from the Wiborg rapakivi area: constraints on the temporal evolution of the rapakivi granite-anorthosite-diabase dyke association of southeastern Finland. Precambrian Research 51, 227-243.

Väisänen, M., Mänttäri, I. and Hölttä, P. 2002. Svecofennian magmatic and metamorphic evolution in southwestern Finland as revealed by U-Pb zircon SIMS geochronology. Precambrian Research 116, 111-127.

van Emden, B., Thornber, M.R., Graham, J. and Lincoln, F. 1997. The incorporation of actinides in monazite and xenotime from placer deposits in Western Australia. Canadian Mineralogist 35, 95-104.

Walshe, J.L. and Cleverley, J.S. 2009. Gold Deposits: Where, When and Why. Elements 5, 288-288.

Wang, J., Wen, H., Li, C., Zhang, J. and Ding, W. 2019. Age and metal source of orogenic gold deposits in Southeast Guizhou Province, China: Constraints from Re–Os and He–Ar isotopic evidence. Geoscience Frontiers 10, 581-593.

Wang, Y., Zeng, Q. and Liu, J. 2014. Rb–Sr Dating of Gold-bearing Pyrites from Wulaga Gold Deposit and its Geological Significance. Resource Geology 64, 262-270.

Wanhainen, C., Broman, C., Martinsson, O. and Magnor, B. 2012. Modification of a Palaeoproterozoic porphyry-like system: Integration of structural, geochemical, petrographic, and fluid inclusion data from the Aitik Cu–Au–Ag deposit, northern Sweden. Ore Geology Reviews 48, 306-331.

Weihed, J.B., Bergstrom, U., Billstrom, K. and Weihed, P. 1996. Geology, tectonic setting, and origin of the Paleoproterozoic Boliden Au-Cu-As deposit, Skellefte District, northern Sweden. Economic Geology 91, 1073-1097.

Williams, M.L., Jercinovic, M.J., Harlov, D.E., Budzyń, B. and Hetherington, C.J. 2011. Resetting monazite ages during fluid-related alteration. Chemical Geology 283, 218-225.

Wood, S.A. 1990a. The aqueous geochemistry of the rare-earth elements and yttrium: 1. Review of available low-temperature data for inorganic complexes and the inorganic REE speciation of natural waters. Chemical Geology 82, 159-186.

Wood, S.A. 1990b. The aqueous geochemistry of the rare-earth elements and yttrium: 2. Theoretical predictions of speciation in hydrothermal solutions to 350°C at saturation water vapor pressure. Chemical Geology 88, 99-125.

Woodard, J., Kietäväinen, R. and Eklund, O. 2014. Svecofennian post-collisional shoshonitic lamprophyres at the margin of the Karelia Craton: Implications for mantle metasomatism. Lithos 205, 379-393.

Zhu, Y.-N. and Peng, J.-T. 2015. Infrared microthermometric and noble gas isotope study of fluid inclusions in ore minerals at the Woxi orogenic Au–Sb–W deposit, western Hunan, South China. Ore Geology Reviews 65, 55-69.

Supplementary Material Table 1: LA-ICP-MS U-Pb data for monazite grains from Kutemajärvi samples.

		Concentration in ppm			Isotopic ratios								Age (Ma)						
Analytical No	Sample-grain	Pb	Th	U	$^{206}Pb/^{204}Pb$	$^{207}Pb/^{206}Pb$	1s	$^{207}Pb/^{235}U$	1s	$^{206}Pb/^{238}U$	1s	r	$^{207}Pb/^{206}Pb$	1s	$^{207}Pb/^{235}U$	1s	$^{206}Pb/^{238}U$	1s	Concordance %
99323	KU567_mnz02	2343	7374	544	2689184	0.1060	0.0003	4.981	0.106	0.341	0.007	0.99	1732	5	1816	18	1890	35	109
99324	KU567_mnz03	728	4277	589	2771880	0.1159	0.0003	5.190	0.111	0.325	0.007	0.99	1894	4	1851	18	1813	34	96
99325	KU567_mnz04	557	3226	477	2302440	0.1141	0.0003	5.245	0.112	0.333	0.007	0.99	1866	4	1860	18	1855	35	99
99326	KU567_mnz05	3070	31910	423	2184760	0.1073	0.0003	5.289	0.113	0.357	0.008	0.99	1754	6	1867	18	1970	36	112
99327	KU567_mnz06	1989	22336	166	762007	0.1026	0.0003	4.498	0.096	0.318	0.007	0.99	1671	6	1731	18	1780	33	106
99328	KU567_mnz07	1382	12661	462	2283894	0.1102	0.0003	5.208	0.111	0.343	0.007	0.99	1803	5	1854	18	1899	35	105
99329	KU567_mnz08	907	7207	400	2049786	0.1066	0.0003	5.221	0.111	0.355	0.008	0.99	1742	5	1856	18	1959	36	112
99330	KU567_mnz09	733	6445	345	1720098	0.1061	0.0003	5.054	0.108	0.346	0.007	0.99	1733	5	1828	18	1914	36	110
99331	KU567_mnz10	1002	9045	283	1424666	0.1072	0.0003	5.160	0.110	0.349	0.008	0.99	1752	5	1846	18	1931	36	110
99332	KU567_mnz12	791	6001	455	2384363	0.1060	0.0003	5.325	0.114	0.364	0.008	0.99	1732	4	1873	18	2002	37	116
99333	KU567_mnz13	713	6874	198	1020436	0.1065	0.0003	5.268	0.112	0.359	0.008	0.99	1741	5	1864	18	1976	37	113
99339	KU568_mnz01	1251	13505	221	760508	0.1109	0.0004	3.674	0.079	0.240	0.005	0.99	1814	6	1566	17	1389	27	77
99340	KU568_mnz02	588	6078	72	357658	0.1121	0.0004	5.354	0.115	0.346	0.007	0.98	1834	7	1878	18	1917	36	105
99341	KU568_mnz03	490	5243	58	510	0.0798	0.0003	3.467	0.074	0.315	0.007	0.99	1191	6	1520	17	1766	33	103
99342	KU568_mnz04	783	8074	117	537078	0.1026	0.0003	4.550	0.097	0.322	0.007	0.99	1671	5	1740	18	1798	34	108
99343	KU568_mnz05	937	10131	176	837423	0.1026	0.0003	4.710	0.101	0.333	0.007	0.99	1671	5	1769	18	1853	35	111
99344	KU568_mnz06	630	6482	115	528591	0.1043	0.0003	4.654	0.099	0.324	0.007	0.99	1703	5	1759	18	1807	34	106
99345	KU568_mnz07	282	2431	77	373230	0.1076	0.0003	5.061	0.108	0.341	0.007	0.99	1759	5	1830	18	1893	35	108
99346	KU568_mnz08	506	4858	122	558539	0.1023	0.0003	4.546	0.097	0.322	0.007	0.99	1666	5	1739	18	1801	34	108
99347	KU568_mnz09	522	5279	103	471017	0.1039	0.0003	4.597	0.098	0.321	0.007	0.99	1694	5	1749	18	1794	34	106
99348	KU568_mnz10	897	9579	125	561890	0.1034	0.0003	4.525	0.097	0.317	0.007	0.99	1687	5	1736	18	1776	33	105
99354	KU543_mnz01	781	2187	1155	5389957	0.1152	0.0003	5.252	0.112	0.331	0.007	0.99	1882	4	1861	18	1842	34	98
99355	KU543_mnz02	497	3161	409	2063119	0.1063	0.0003	~~5.243~~	~~0.112~~	~~0.358~~	~~0.008~~	~~0.99~~	1737	5	1860	18	1971	36	113
99356	KU543_mnz03	448	2150	470	2364670	0.1061	0.0003	~~5.225~~	~~0.111~~	~~0.357~~	~~0.008~~	~~0.99~~	1733	4	1857	18	1969	36	114
99357	KU543_mnz04	1424	6596	1743	8111590	0.1152	0.0003	5.249	0.112	0.331	0.007	0.99	1882	4	1861	18	1841	34	98
99358	KU543_mnz05	827	2175	1265	5916329	0.1149	0.0003	5.268	0.112	0.333	0.007	0.99	1878	4	1864	18	1851	35	99
99359	KU543_mnz06	219	1410	133	656848	0.1080	0.0003	~~5.245~~	~~0.112~~	~~0.352~~	~~0.008~~	~~0.99~~	1766	5	1860	18	1945	36	110
99360	KU543_mnz07	433	2362	406	2038010	0.1060	0.0003	~~5.222~~	~~0.111~~	~~0.357~~	~~0.008~~	~~0.99~~	1732	4	1856	18	1970	36	114
99361	KU543_mnz08	511	3242	415	2086965	0.1067	0.0003	~~5.275~~	~~0.113~~	~~0.359~~	~~0.008~~	~~0.99~~	1743	4	1865	18	1976	37	113
99362	KU543_mnz09	504	2692	534	2469614	0.1145	0.0003	5.206	0.111	0.330	0.007	0.99	1871	4	1854	18	1838	34	98
99371	KOH8 95.20_mnz04	671	1762	1002	5563	0.1124	0.0003	5.243	0.112	0.338	0.007	0.99	1839	4	1860	18	1878	35	100
99369	KOH8 95.20_mnz02	877	1372	1501	8122	0.1136	0.0003	5.305	0.113	0.339	0.007	0.99	1858	4	1870	18	1880	35	100
99372	KOH8 95.20_mnz05	1042	4042	1434	4703	0.1138	0.0003	5.122	0.109	0.326	0.007	0.99	1861	4	1840	18	1821	34	96
99383	KOH8 95.20_mnz16	545	2489	617	8494	0.1143	0.0003	5.302	0.113	0.337	0.007	0.99	1868	5	1869	18	1870	35	99
99374	KOH8 95.20_mnz07	715	3818	742	3498141	0.1143	0.0003	5.356	0.114	0.340	0.007	0.99	1869	4	1878	18	1886	35	101
99376	KOH8 95.20_mnz09	641	2667	804	3757628	0.1144	0.0003	5.327	0.114	0.338	0.007	0.99	1870	4	1873	18	1876	35	100
99378	KOH8 95.20_mnz11	908	2049	1460	7709	0.1144	0.0003	5.291	0.113	0.335	0.007	0.99	1870	4	1867	18	1865	35	98
99380	KOH8 95.20_mnz13	734	4200	697	1986	0.1146	0.0003	5.387	0.115	0.341	0.007	0.99	1874	4	1883	18	1891	35	96
99370	KOH8 95.20_mnz03	859	1263	1551	7711	0.1147	0.0003	5.141	0.110	0.325	0.007	0.99	1876	4	1843	18	1814	34	95
99377	KOH8 95.20_mnz10	656	3436	693	3258589	0.1148	0.0003	5.379	0.115	0.340	0.007	0.99	1877	4	1882	18	1886	35	101
99373	KOH8 95.20_mnz06	525	1530	749	3530082	0.1156	0.0003	5.411	0.115	0.340	0.007	0.99	1889	4	1887	18	1884	35	100
99375	KOH8 95.20_mnz08	984	2343	1579	7305941	0.1157	0.0003	5.331	0.114	0.334	0.007	0.99	1892	4	1874	18	1858	35	98
99381	KOH8 95.20_mnz14	749	1081	1378	10886	0.1081	0.0003	4.903	0.105	0.329	0.007	0.99	1768	4	1803	18	1833	34	103
99368	KOH8 95.20_mnz01	781	8269	104	1095	0.0965	0.0003	4.750	0.102	0.357	0.008	0.99	1557	5	1776	18	1968	36	112
99382	KOH8 95.20_mnz15	568	3258	506	2530231	0.1060	0.0003	5.309	0.113	0.363	0.008	0.99	1732	5	1870	18	1997	37	115
99379	KOH8 95.20_mnz12	293	3196	180	921303	0.1058	0.0004	5.405	0.116	0.371	0.008	0.99	1728	6	1886	18	2032	37	118

99399	KOH15_mnz01	4022	13231	1211	2689184	0.1060	0.0007	4.981	0.106	0.341	0.007	0.95	1732	12	1816	18	1890	33	109
99400	KOH15_mnz02	1249	7674	1311	2771880	0.1159	0.0008	5.190	0.110	0.325	0.007	0.95	1894	12	1851	18	1813	32	96
99401	KOH15_mnz03	956	5788	1062	2302440	0.1141	0.0008	5.245	0.111	0.333	0.007	0.95	1866	12	1860	18	1855	32	99
99402	KOH24X_mnz01	5269	57253	940	2184760	0.1073	0.0007	5.289	0.113	0.357	0.007	0.95	1754	13	1867	18	1970	34	112
99403	KOH24X_mnz02	3414	40075	369	762007	0.1026	0.0007	4.498	0.096	0.318	0.006	0.95	1671	13	1731	18	1780	31	106
99404	KOH24X_mnz03	2371	22716	1028	2283894	0.1102	0.0007	5.208	0.111	0.343	0.007	0.95	1803	12	1854	18	1899	33	105
99405	KOH24X_mnz04	1557	12931	890	2049786	0.1066	0.0007	5.221	0.111	0.355	0.007	0.95	1742	12	1856	18	1959	34	112
99406	KOH24X_mnz05	1257	11563	768	1720098	0.1061	0.0007	5.054	0.107	0.346	0.007	0.95	1733	12	1828	18	1914	33	110
99407	KOH24X_mnz06	1720	16229	630	1424666	0.1072	0.0007	5.160	0.110	0.349	0.007	0.95	1752	12	1846	18	1931	33	110
99408	KOH24X_mnz07	1358	10768	1012	2384363	0.1060	0.0007	5.325	0.113	0.364	0.007	0.95	1732	12	1873	18	2002	34	116
99409	KOH24X_mnz08	1224	12334	440	1020436	0.1065	0.0007	5.268	0.112	0.359	0.007	0.95	1741	12	1864	18	1976	34	113
99415	KOH24X_mnz09	2148	24231	492	760508	0.1109	0.0008	3.674	0.078	0.240	0.005	0.94	1814	13	1566	17	1389	25	77
99416	KOH24X_mnz10	1010	10906	161	357658	0.1121	0.0008	5.354	0.115	0.346	0.007	0.94	1834	13	1878	18	1917	33	105
99417	KOH24X_mnz11	842	9407	129	510	0.0798	0.0006	3.467	0.074	0.315	0.006	0.94	1191	14	1520	17	1766	31	103
99418	KOH24X_mnz12	1343	14486	260	537078	0.1026	0.0007	4.550	0.097	0.322	0.006	0.95	1671	13	1740	18	1798	31	108
99419	KOH24X_mnz13	1609	18177	393	837423	0.1026	0.0007	4.710	0.100	0.333	0.007	0.95	1671	13	1769	18	1853	32	111
99420	KOH24X_mnz14	1082	11631	255	528591	0.1043	0.0007	4.654	0.099	0.324	0.006	0.95	1703	13	1759	18	1807	32	106
99421	KOH24X_mnz15	485	4362	171	373230	0.1076	0.0007	5.061	0.108	0.341	0.007	0.95	1759	13	1830	18	1893	33	108
99422	021-6A_mnz01	868	8717	271	558539	0.1023	0.0007	4.546	0.097	0.322	0.006	0.95	1666	13	1739	18	1801	31	108
99423	KU569_mnz01	896	9471	230	471017	0.1039	0.0007	4.597	0.098	0.321	0.006	0.95	1694	13	1749	18	1794	31	106
99424	KU569_mnz02	1539	17187	278	561890	0.1034	0.0007	4.525	0.096	0.317	0.006	0.95	1687	13	1736	18	1776	31	105
99425	KU569_mnz03a	3503	23523	1180	3684136	0.1788	0.0012	12.089	0.256	0.490	0.010	0.95	2642	11	2611	20	2572	42	97
99426	KU569_mnz03b	4111	43471	1287	2731255	0.1174	0.0008	5.400	0.115	0.334	0.007	0.95	1917	12	1885	18	1856	32	97
99492	KU582Mnz01	605	2503	2169	853379	0.1173	0.0016	3.001	0.062	0.186	0.005	0.86	1916	24	1408	16	1097	27	57
99493	KU582Mnz02	823	8125	177	847	0.0987	0.0015	4.530	0.099	0.333	0.009	0.81	1599	29	1736	18	1853	43	100
99494	KU582Mnz03	216	4303	20	1	1.2092	0.0183	-2749.662	-59.632	-16.493	-0.443	0.83	5503	21	#VALUE!	#VALUE!	#VALUE!	#VALUE!	161
99495	KU582Mnz04	62	947	22	1	1.1923	0.0220	-552.748	-12.977	-3.362	-0.092	0.75	5483	25	#VALUE!	#VALUE!	#VALUE!	#VALUE!	54
99496	KU582Mnz05	40	375	19	56	-0.2352	-0.0043	-8.636	-0.206	0.266	0.007	0.74	#NUM!	#NUM!	#VALUE!	#VALUE!	1522	36	119
99497	KU582Mnz06	69	1178	10	1	1.0521	0.0350	-571.818	-20.336	-3.942	-0.115	0.49	5309	46	#VALUE!	#VALUE!	#VALUE!	#VALUE!	111
99498	KU582Mnz07	276	2321	615	32	-0.7019	-0.0098	-13.478	-0.281	0.139	0.004	0.85	#NUM!	#NUM!	#VALUE!	#VALUE!	840	21	86
99499	KU559_mnz01	988	8171	581	407877	0.1110	0.0015	5.037	0.105	0.329	0.009	0.85	1816	25	1826	18	1834	42	101
99500	KU559_mnz02	1512	5183	3280	2390041	0.1195	0.0016	5.623	0.116	0.341	0.009	0.86	1948	24	1920	18	1893	43	97
99501	KU559_mnz03	1934	12230	2613	13499	0.1169	0.0016	5.453	0.113	0.338	0.009	0.86	1910	24	1893	18	1878	43	98
99502	Sarvisuo IA_mnz01	2433	3809	6634	2196	0.1191	0.0016	5.592	0.116	0.341	0.009	0.86	1943	24	1915	18	1890	43	94
99503	Sarvisuo IA_mnz02	2258	11077	3747	15682	0.1108	0.0015	5.164	0.107	0.338	0.009	0.85	1812	25	1847	18	1877	43	103
99504	Sarvisuo IA_mnz03	2146	13728	2373	324	0.1205	0.0016	5.563	0.115	0.335	0.009	0.86	1964	24	1910	18	1862	43	78
99510	Sarvisuo IA_mnz04	1777	8750	1653	137	0.1166	0.0016	6.298	0.130	0.392	0.010	0.86	1904	24	2018	18	2131	48	80
99511	Sarvisuo IA_mnz05	2916	16022	4106	741	0.1191	0.0016	5.533	0.114	0.337	0.009	0.86	1943	24	1906	18	1871	43	87
99512	Sarvisuo IA_mnz06	1807	14401	1158	241	0.1127	0.0015	5.705	0.118	0.367	0.010	0.86	1844	25	1932	18	2015	45	84
99513	Sarvisuo IA_mnz07	1672	12325	744	108	0.1180	0.0016	6.569	0.136	0.404	0.011	0.86	1926	24	2055	18	2186	49	79
99514	Sarvisuo IIA mnz01	2771	12388	3389	146	0.1263	0.0017	6.272	0.130	0.360	0.009	0.86	2047	24	2015	18	1983	45	73
99515	Sarvisuo IIA mnz02	1510	7713	2354	10054	0.1121	0.0015	5.338	0.111	0.345	0.009	0.86	1834	25	1875	18	1913	44	103
99516	Sarvisuo IIA mnz03	1073	7723	765	714	0.1093	0.0015	5.243	0.109	0.348	0.009	0.85	1789	25	1860	18	1924	44	94
99517	Sarvisuo IIA mnz04	2710	12004	5384	35263	0.1181	0.0016	5.468	0.113	0.336	0.009	0.86	1928	24	1896	18	1866	43	97
99518	Sarvisuo IIA mnz05	1078	4330	2208	3650	0.1084	0.0015	4.817	0.100	0.322	0.008	0.86	1773	25	1788	17	1801	41	99
99519	Sarvisuo IIA mnz06	2926	16105	4780	2297	0.1198	0.0016	5.395	0.112	0.327	0.009	0.86	1953	24	1884	18	1822	42	90
99520	Sarvisuo IIA mnz07	2031	7287	3508	342	0.1209	0.0017	5.763	0.119	0.346	0.009	0.86	1969	24	1941	18	1915	44	81
99521	Sarvisuo IIA mnz08	1644	13787	999	829	0.1128	0.0015	5.568	0.115	0.358	0.009	0.86	1846	25	1911	18	1972	45	96
99522	Sarvisuo IIA mnz09	3249	6583	9274	24251	0.1196	0.0016	5.197	0.108	0.315	0.008	0.86	1951	24	1852	17	1765	41	90
99523	Sarvisuo IIA mnz10	1762	8671	2824	3933	0.1117	0.0015	5.381	0.111	0.350	0.009	0.86	1827	25	1882	18	1932	44	103

99529	Sarvisuo IIA mnz11	1858	8678	1006	63	0.1434	0.0020	9.723	0.201	0.492	0.013	0.86	2269	23	2409	19	2578	56	84
99530	Sarvisuo IIA mnz12	1439	7010	1938	444	0.1208	0.0017	5.789	0.120	0.348	0.009	0.86	1968	24	1945	18	1923	44	84
99531	Sarvisuo IIA mnz13	2698	12144	3914	281	0.1231	0.0017	5.790	0.120	0.341	0.009	0.86	2002	24	1945	18	1892	43	77
99532	Sarvisuo IIA mnz14	1662	10832	1690	2333	0.1124	0.0016	5.402	0.112	0.349	0.009	0.86	1838	25	1885	18	1928	44	101
99533	Sarvisuo IIA mnz15	1541	8771	2284	817	0.1215	0.0017	5.318	0.110	0.317	0.008	0.86	1979	24	1872	18	1777	41	82
99534	Sarvisuo IIA mnz16	2884	12194	5951	4231380	0.1214	0.0017	5.425	0.112	0.324	0.009	0.86	1977	24	1889	18	1809	41	91
99535	Sarvisuo IIA mnz17	3079	9847	6708	780	0.1246	0.0017	5.422	0.112	0.316	0.008	0.86	2023	24	1888	18	1769	41	80
99536	Sarvisuo IIA mnz18	2179	18232	1351	3309	0.1151	0.0016	5.685	0.118	0.358	0.009	0.85	1882	25	1929	18	1974	45	102
99537	Sarvisuo IIA mnz19	1879	13720	1926	1437115	0.1126	0.0016	5.265	0.109	0.339	0.009	0.86	1841	25	1863	18	1883	43	102
99538	Sarvisuo IIA mnz20	2826	15536	4397	1894	0.1205	0.0017	5.340	0.111	0.321	0.008	0.86	1964	24	1875	18	1797	41	88
99539	Sarvisuo IIA mnz21	1722	9277	2748	1827	0.1224	0.0017	5.412	0.112	0.321	0.008	0.86	1991	24	1887	18	1794	41	86
99540	Sarvisuo IIA mnz22	2896	14448	1938	84	0.1311	0.0018	8.083	0.167	0.447	0.012	0.86	2113	24	2240	19	2383	52	81
99541	Sarvisuo IIA mnz23	2339	8616	5116	8570	0.1216	0.0017	5.235	0.108	0.312	0.008	0.86	1980	24	1858	17	1751	40	88
99542	Sarvisuo IIA mnz24	2168	9979	3947	6470	0.1218	0.0017	5.519	0.114	0.329	0.009	0.86	1982	24	1904	18	1832	42	91
99543	Sarvisuo IIA mnz25	2474	13106	3635	3505	0.1225	0.0017	5.507	0.114	0.326	0.009	0.86	1992	24	1902	18	1820	42	89
99549	Sarvisuo IIA mnz26	1722	11143	2195	13654	0.1139	0.0016	5.402	0.112	0.344	0.009	0.85	1862	25	1885	18	1906	43	102
99550	Sarvisuo IIA mnz27	3030	23991	1899	1200	0.1144	0.0016	5.641	0.117	0.358	0.009	0.86	1871	25	1922	18	1970	45	98
99551	Sarvisuo IIA mnz28	2348	5409	6115	4376821	0.1233	0.0017	5.468	0.113	0.322	0.008	0.86	2004	24	1896	18	1798	41	90
99552	Sarvisuo IIA mnz29	2217	7778	1832	70	0.1541	0.0021	9.106	0.188	0.428	0.011	0.86	2392	23	2349	19	2299	51	75
99553	Sarvisuo IIA mnz30	3391	34533	668	517	0.1122	0.0015	4.983	0.103	0.322	0.008	0.86	1835	25	1817	17	1800	41	84
99554	Sarvisuo IIA mnz31	1947	12638	2102	907	0.1239	0.0017	5.534	0.115	0.324	0.009	0.86	2013	24	1906	18	1809	41	83
99555	Sarvisuo IIA mnz32	2717	17754	3533	7803	0.1222	0.0017	5.458	0.113	0.324	0.009	0.86	1989	24	1894	18	1809	41	90
99556	Sarvisuo IIA mnz33	2239	10005	3726	424	0.1237	0.0017	5.432	0.113	0.318	0.008	0.86	2011	24	1890	18	1782	41	77
99557	Sarvisuo IIA mnz34	2259	11888	3068	453	0.1187	0.0016	5.103	0.106	0.312	0.008	0.86	1937	24	1837	17	1749	40	77
99558	Sarvisuo IIA mnz35	1540	6399	2904	2184184	0.1147	0.0016	5.316	0.110	0.336	0.009	0.86	1875	25	1871	18	1868	43	100
99559	Sarvisuo IIA mnz36	1414	1298	684	42	0.2139	0.0029	20.312	0.421	0.689	0.018	0.86	2935	22	3106	20	3378	69	103
99560	Sarvisuo IIA mnz37	2779	19422	3743	6488	0.1130	0.0016	4.257	0.088	0.273	0.007	0.86	1849	25	1685	17	1557	36	83
99561	Sarvisuo IIA mnz38	1954	5823	4325	1450	0.1219	0.0017	5.442	0.113	0.324	0.009	0.86	1985	24	1892	18	1808	41	86
99562	Sarvisuo IIA mnz39	1790	9105	2827	10946	0.1152	0.0016	5.307	0.110	0.334	0.009	0.86	1883	25	1870	18	1859	42	98
99563	Sarvisuo IIA mnz40	1908	14662	1428	510	0.1149	0.0016	5.400	0.112	0.341	0.009	0.86	1878	25	1885	18	1891	43	87

Supplementary Material Table 2: LA-ICP-MS U-Pb data for zircon grains from Kutemajärvi samples.

		Concentration in ppm					Isotopic ratios								Age (Ma)					
Analytical No	Sample-grain	Pb	Th	U	$^{206}Pb/^{Pb}204$	$^{206}Pbc(\%)$	$^{207}Pb/^{206}Pb$	1s	$^{207}Pb/^{235}U$	1s	$^{206}Pb/^{238}U$	1s	r	$^{207}Pb/^{206}Pb$	1s	$^{207}Pb/^{235}U$	1s	$^{206}Pb/^{238}U$	1s	Concordance %
99827	KU021-6A_zr01	153	1357	481	49	35.4007	0.1817	0.0009	2.869	0.059	0.115	0.002	0.97	2668	8	1374	15	699	13	26
99828	KU021-6A_zr02	364	606	1360	30	58.3118	0.3335	0.0015	3.092	0.063	0.067	0.001	0.97	3633	7	1431	16	420	8	12
99829	KU021-6A_zr03	9317	467	424	15	112.3801	1.2554	0.0056	527.586	10.739	3.048	0.061	0.98	5555	6	6367	20	9014	97	162
99830	KU021-6A_zr04	210	834	1197	213	8.0956	0.0959	0.0004	1.499	0.031	0.113	0.002	0.97	1546	9	930	12	692	13	45
99831	KU021-6A_zr05	127	3322	825	8	216.1469	2.7723	0.0143	-14.551	-0.298	-0.038	-0.001	0.97	6635	7	#VALUE!	#VALUE!	-250	-5	-4
99832	KU021-6A_zr06	63	73	190	1531	1.1241	0.1196	0.0006	4.452	0.091	0.270	0.005	0.97	1950	9	1722	17	1541	27	79
99821	KU174_zr01	84	89	226	4344	0.3963	0.1125	0.0005	4.857	0.099	0.313	0.006	0.97	1840	9	1795	17	1756	31	95
99822	KU174_zr02	39	45	99	2341	0.7353	0.1128	0.0006	5.042	0.103	0.324	0.007	0.97	1845	9	1826	17	1810	32	98
99823	KU174_zr03	106	158	246	5147	0.3345	0.1125	0.0005	5.300	0.108	0.342	0.007	0.97	1841	9	1869	17	1894	33	103
99824	KU174_zr04	193	385	454	7177	0.2399	0.1135	0.0005	4.994	0.102	0.319	0.006	0.97	1856	8	1818	17	1786	31	96
99825	KU174_zr05	609	1423	1361	32141	0.0536	0.1232	0.0006	5.381	0.110	0.317	0.006	0.98	2003	8	1882	17	1774	31	89
99826	KU174_zr06	287	541	599	1114751	0.0015	0.1141	0.0005	5.689	0.116	0.362	0.007	0.97	1865	8	1930	17	1990	34	107
99766	KU453_zr01	198	215	480	9634	0.1787	0.1149	0.0004	5.573	0.113	0.352	0.007	0.98	1878	7	1912	17	1943	34	103
99767	KU453_zr02	398	576	971	1363	1.2630	0.1042	0.0004	4.762	0.096	0.331	0.007	0.98	1701	6	1778	17	1845	32	108
99768	KU453_zr03	67	58	182	3290	0.5233	0.1107	0.0004	4.868	0.099	0.319	0.006	0.98	1811	7	1797	17	1785	31	99
99769	KU453_zr04	195	263	441	811229	0.0021	0.1151	0.0004	5.753	0.116	0.363	0.007	0.98	1881	6	1939	17	1994	34	106
99770	KU453_zr05	164	153	388	718123	0.0024	0.1141	0.0004	5.739	0.116	0.365	0.007	0.98	1866	7	1937	17	2004	34	107
99771	KU453_zr06	111	135	253	467499	0.0037	0.1161	0.0004	5.828	0.118	0.364	0.007	0.98	1897	7	1951	17	2001	34	105
99772	KU453_zr07	59	47	161	1748	0.9846	0.1073	0.0005	4.729	0.096	0.320	0.006	0.98	1753	8	1772	17	1789	31	102
99773	KU453_zr08	344	328	812	1216	1.4153	0.1006	0.0004	4.931	0.100	0.356	0.007	0.98	1635	7	1808	17	1962	34	120
99774	KU453_zr09	91	128	225	3185	0.5405	0.1116	0.0004	5.120	0.104	0.333	0.007	0.98	1826	7	1839	17	1851	32	101
99775	KU453_zr10	209	389	600	848	2.0311	0.0982	0.0004	3.775	0.076	0.279	0.006	0.98	1589	7	1587	16	1586	28	100
99784	KU568_zr01	181	1055	1066	12420	0.1386	0.1008	0.0004	1.967	0.040	0.142	0.003	0.98	1639	7	1104	14	854	16	52
99785	KU568_zr02	1156	3672	2751	3724	0.4622	0.1076	0.0004	4.334	0.088	0.292	0.006	0.98	1759	7	1700	17	1652	29	94
99786	KU568_zr03	164	713	566	8575	0.2007	0.1092	0.0005	3.532	0.072	0.235	0.005	0.98	1786	8	1534	16	1358	25	76
99787	KU568_zr04a	406	1116	973	9637	0.1786	0.1214	0.0005	4.967	0.100	0.297	0.006	0.98	1976	7	1814	17	1676	30	85
99788	KU568_zr04b	40	32	102	2029	0.8485	0.1084	0.0005	5.135	0.105	0.343	0.007	0.97	1773	8	1842	17	1903	33	107
99789	KU568_zr05	195	1534	780	763083	0.0023	0.1105	0.0004	2.924	0.059	0.192	0.004	0.98	1808	7	1388	15	1132	21	63
99790	KU568_zr06	126	1487	975	521728	0.0033	0.1104	0.0005	1.597	0.033	0.105	0.002	0.97	1806	8	969	13	643	12	36
99791	KU568_zr07	112	401	301	473155	0.0036	0.1144	0.0005	4.858	0.098	0.308	0.006	0.98	1870	7	1795	17	1731	30	93
99792	KU568_zr08	80	463	239	5192	0.3316	0.1088	0.0004	4.143	0.084	0.276	0.006	0.98	1779	8	1663	16	1572	28	88
99793	KU568_zr09	239	744	840	8982	0.1916	0.1076	0.0004	3.383	0.069	0.228	0.005	0.98	1760	7	1500	16	1324	24	75
99794	KU568_zr10	370	2551	3080	5859	0.2938	0.0824	0.0003	1.038	0.021	0.091	0.002	0.98	1254	8	723	10	564	11	45
99795	KU568_zr11	194	698	700	6304	0.2731	0.1083	0.0005	3.338	0.068	0.224	0.004	0.98	1771	8	1490	16	1300	24	73
99796	KU568_zr12	39	36	109	174249	0.0099	0.1173	0.0008	5.069	0.106	0.313	0.006	0.94	1915	12	1831	18	1757	31	92
99797	KU568_zr13	172	541	496	10111	0.1703	0.1104	0.0004	4.126	0.084	0.271	0.005	0.98	1806	7	1660	16	1547	28	86
99798	KU568_zr14	155	408	509	9444	0.1823	0.1202	0.0005	4.267	0.087	0.258	0.005	0.98	1959	8	1687	17	1477	26	75
99803	KU568_zr15	51	262	146	3291	0.5231	0.1085	0.0005	4.210	0.086	0.281	0.006	0.97	1775	8	1676	17	1598	28	90
99804	KU568_zr16	315	1746	2260	4562	0.3773	0.0777	0.0003	1.116	0.023	0.104	0.002	0.98	1139	8	761	11	639	12	56
99805	KU568_zr17	203	1442	1655	6403	0.2688	0.0879	0.0004	1.215	0.025	0.100	0.002	0.98	1380	8	808	11	616	12	45
99806	KU568_zr18	218	1118	808	7728	0.2228	0.1071	0.0004	3.192	0.065	0.216	0.004	0.98	1751	8	1455	16	1261	23	72
99807	KU568_zr19	154	237	426	671379	0.0026	0.1140	0.0005	4.833	0.098	0.308	0.006	0.98	1864	8	1791	17	1728	30	93
99808	KU568_zr20	132	230	333	543883	0.0032	0.1155	0.0005	5.071	0.103	0.318	0.006	0.98	1887	8	1831	17	1782	31	94
99809	KU568_zr21	259	582	924	1113710	0.0015	0.1123	0.0005	3.643	0.074	0.235	0.005	0.98	1837	8	1559	16	1362	25	74
99810	KU568_zr22	195	380	756	828999	0.0021	0.1090	0.0005	3.217	0.065	0.214	0.004	0.98	1782	8	1461	16	1251	23	70
99811	KU568_zr23	185	1706	1415	10010	0.1720	0.0872	0.0004	1.209	0.025	0.101	0.002	0.98	1365	8	805	11	618	12	45

99812	KU568_zr24	113	1257	948	3563	0.4832	0.0985	0.0005	1.189	0.024	0.088	0.002	0.97	1596	9	795	11	541	10	34
99813	KU568_zr25	193	3172	2123	3907	0.4406	0.0743	0.0004	0.670	0.014	0.065	0.001	0.97	1049	10	521	8	408	8	39
99814	KU568_zr26	189	670	702	8106	0.2124	0.1073	0.0005	3.258	0.066	0.220	0.004	0.98	1753	8	1471	16	1284	23	73
99815	KU568_zr27	119	382	395	7348	0.2343	0.1179	0.0005	3.882	0.079	0.239	0.005	0.97	1925	8	1610	16	1380	25	72
99816	KU568_zr28	262	3746	3211	7040	0.2445	0.0693	0.0003	0.570	0.012	0.060	0.001	0.97	908	9	458	7	374	7	41

Supplementary Material Table 3: Concentrated data for monazite grains from Kutemajärvi samples.

Single-grain	O	Mg	F	Br	Al	Si	P	K	Ni	Cu	Ag	Ca	Fe	Y	La	Ce	Nd	Sm	Total	$^{207}Pb/^{206}Pb$ Age (Ma)	1s	Concordance	Textural setting
KOH-8 95.20 mnz1	41.85	-	-	-	4.09	11.48	10.33	0.96	-	-	1.33	-	-	-	7.95	15.58	6.44	-	100.00	1557	5	112	Strain shadow type
KOH-8 95.20 mnz2	40.47	-	-	-	6.13	6.81	10.79	1.84	-	-	-	0.88	-	-	6.69	17.47	8.91	-	100.00	1858	4	100	Strain shadow type
KOH-8 95.20 mnz3	40.82	-	0.00	-	4.96	8.26	10.23	1.12	-	-	1.43	0.93	-	-	8.55	16.82	6.88	-	100.00	1876	4	95	Strain shadow type
KOH-8 95.20 mnz4	39.57	-	-	-	6.81	5.78	10.84	1.74	-	-	-	-	-	-	10.30	18.59	6.37	-	100.00	1839	4	100	Spongy
KOH-8 95.20 mnz5	39.74	-	1.45	-	3.67	4.10	12.12	1.04	-	-	-	3.17	-	-	10.43	17.80	6.46	-	100.00	1861	4	96	Spongy
KOH-8 95.20 mnz6	38.72	-	-	-	4.41	5.16	12.21	1.20	-	-	-	1.76	-	-	8.41	19.20	8.94	-	100.00	1889	4	100	Both types
KOH-8 95.20 mnz7	40.35	-	0.00	-	7.40	6.58	10.22	1.79	-	-	-	-	-	-	8.31	18.09	7.26	-	100.00	1869	4	101	Spongy
KOH-8 95.20 mnz8	40.37	-	0.00	-	6.51	6.11	10.35	1.65	-	-	-	0.75	-	-	9.83	17.86	6.57	-	100.00	1892	4	98	Ambiguous
KOH-8 95.20 mnz9	40.43	-	-	-	3.41	10.85	10.62	0.93	-	-	-	-	-	-	7.87	18.57	7.32	-	100.00	1870	4	100	Spongy
KOH-8 95.20 mnz10	39.78	-	0.00	-	4.70	5.48	11.17	1.23	-	-	-	1.17	-	-	9.73	18.59	8.15	-	100.00	1877	4	101	Spongy
KOH-8 95.20 mnz11	42.23	-	0.00	-	4.57	6.16	11.56	1.03	-	-	-	1.94	-	-	6.65	16.49	9.38	-	100.00	1870	4	98	Both types
KOH-8 95.20 mnz12	39.84	-	0.00	-	1.18	14.13	9.84	0.56	-	-	-	-	-	-	9.95	18.36	6.13	-	100.00	1728	6	118	Ambiguous
KOH-8 95.20 mnz13	38.48	-	0.00	-	2.70	5.56	12.03	0.72	-	-	-	1.98	-	-	8.51	18.77	3.07	-	100.00	1874	4	96	Spongy
KOH-8 95.20 mnz14	41.38	-	_	_	6.23	5.61	10.41	1.53	-	-	_	1.78	-	-	9.40	17.02	6.65	-	100.00	1768	4	103	Ambiguous
KOH-8 95.20 mnz15	41.19	-	_	_	3.85	8.85	10.62	1.07	-	-	1.05	0.94	-	-	9.65	16.81	5.96	-	100.00	1732	5	115	Spongy
KOH-8 95.20 mnz16	39.27	-	_	_	3.13	9.01	11.18	0.81	-	-	_	0.75	-	-	9.85	18.94	7.06	-	100.00	1868	5	99	Both types
KOH-15 mnz1	40.84	-	_	_	_	10.93	11.33	_	_	_	_	0.42	-	-	9.04	19.86	7.58	-	100.00	1732	12	109	Ambiguous
KOH-15 mnz2	43.55	-	_	_	0.62	9.16	12.32	_	_	_	_	0.81	-	-	4.22	16.98	12.33	-	100.00	1894	12	96	Ambiguous
KOH-15 mnz3	40.49	-	_	_	0.39	9.74	11.51	_	_	_	_	0.54	-	-	9.19	19.73	8.41	-	100.00	1866	12	99	Ambiguous
KOH-24x mnz1	39.48	1.34	_	_	5.16	4.26	11.95	_	_	_	_	_	-	-	11.01	20.85	5.94	-	100.00	1754	13	112	Spongy
KOH-24x mnz2	38.30	1.71	_	_	2.32	5.70	11.93	_	_	_	_	_	-	-	11.74	21.65	6.66	-	100.00	1671	13	106	Spongy
KOH-24x mnz3	40.85	_	_	_	8.91	4.99	10.52	_	_	_	_	_	-	-	9.73	19.57	5.42	-	100.00	1803	12	105	Ambiguous
KOH-24x mnz4	39.05	_	_	_	8.14	4.62	10.78	_	_	_	_	_	-	-	10.67	19.29	7.46	-	100.00	1742	12	112	Spongy
KOH-24x mnz5	40.35	2.70	_	_	3.33	5.46	10.61	0.96	-	-	_	_	-	-	9.61	19.45	7.54	-	100.00	1733	12	110	Ambiguous
KOH-24x mnz6	42.21	_	_	_	9.15	5.49	10.18	_	_	_	_	_	-	-	9.06	18.39	5.53	-	100.00	1752	12	110	Ambiguous
KOH-24x mnz7	41.63	_	_	_	8.38	5.76	10.30	_	_	_	_	_	-	-	9.26	17.92	6.76	-	100.00	1732	12	116	Ambiguous
KOH-24x mnz8	39.19	1.15	_	_	2.96	7.23	10.60	_	_	_	_	_	-	-	10.69	20.21	7.97	-	100.00	1741	12	113	Spongy
KOH-24x mnz9	41.50	_	_	_	5.92	6.69	10.58	0.77	-	-	_	_	-	-	9.43	17.50	7.60	-	100.00	1814	13	77	Ambiguous
KOH-24x mnz10	40.59	_	_	_	7.73	4.81	10.33	0.73	-	-	_	_	-	-	8.55	18.68	8.59	-	100.00	1834	13	105	Ambiguous
KOH-24x mnz11	43.70	_	_	_	9.45	4.62	10.69	_	_	_	_	_	-	-	7.98	17.94	5.62	-	100.00	1191	14	103	Ambiguous
KOH-24x mnz12	40.60	_	_	_	7.14	5.92	10.65	_	_	_	_	_	-	-	9.50	18.67	7.52	-	100.00	1671	13	108	Ambiguous
KOH-24x mnz13	39.06	_	_	_	6.16	6.24	11.66	_	_	_	_	_	-	-	11.31	18.44	7.13	-	100.00	1671	13	111	Ambiguous
KOH-24x mnz14	40.33	_	_	_	9.64	5.69	9.34	_	_	_	_	_	-	-	9.98	18.63	6.38	-	100.00	1703	13	106	Ambiguous
KOH-24x mnz15	40.09	_	_	_	5.79	7.01	11.24	_	_	_	_	_	-	-	8.96	20.89	6.02	-	100.00	1759	13	108	Ambiguous
KU 021-6A mnz1	41.05	_	0.00	-	2.90	3.46	11.91	0.73	-	-	_	_	1.55	-	10.46	20.75	7.19	-	100.00	1666	13	108	Ambiguous
KU-567 243.20 mnz1	40.20	_	0.00	-	1.47	8.53	11.52	0.48	-	-	-	0.36	-	-	13.07	19.22	5.15	-	100.00	-	-	-	Ambiguous
KU-567 243.20 mnz2	39.77	_	0.00	-	1.07	8.65	12.11	_	-	-	-	-	-	-	12.67	20.36	5.36	-	100.00	1732	5	109	Ambiguous
KU-567 243.20 mnz3	41.01	_	0.00	-	1.37	8.38	12.08	_	-	-	-	-	-	-	10.81	20.29	6.06	-	100.00	1894	4	96	Ambiguous
KU-567 243.20 mnz4	40.22	_	0.00	-	2.02	7.59	11.78	0.37	-	_	_	_	-	-	13.05	19.91	5.05	-	100.00	1866	4	99	Ambiguous
KU-567 243.20 mnz5	41.32	_	0.00	-	1.55	9.10	11.44	0.41	-	_	_	_	-	-	8.63	20.15	7.41	-	100.00	1754	6	112	Spongy
KU-567 243.20 mnz6	41.35	_	0.00	-	2.78	5.90	11.48	0.69	-	_	1.94	_	-	-	10.23	19.33	6.30	-	100.00	1671	6	106	Strain shadow type
KU-567 243.20 mnz7	39.72	_	2.22	-	4.50	4.33	11.49		-	-	1.24	0.79	-	-	7.37	18.86	9.46	-	100.00	1803	5	105	Spongy
KU-567 243.20 mnz8	40.71	_	0.00	-	2.38	6.36	12.09	0.60	-	_	_	_	-	-	8.27	20.97	8.63	-	100.00	1742	5	112	Strain shadow type
KU-567 243.20 mnz9	39.88	_	0.00	-	1.48	8.49	11.48	0.29	-	_	_	_	-	-	12.00	20.33	6.05	-	100.00	1733	5	110	Ambiguous
KU-567 243.20 mnz10	41.47	_	0.00	-	2.44	7.41	11.95	0.58	-	_	_	_	-	-	9.11	20.19	6.86	-	100.00	1752	5	110	Ambiguous
KU-567 243.20 mnz11	39.74	_	0.00	-	0.73	5.32	13.14	_	-	_	_	_	-	-	8.92	22.21	9.94	-	100.00	-	-	-	Both types
KU-567 243.20 mnz12	39.29	_	1.77	-	3.29	4.20	11.11	0.73	-	2.16	1.06	0.30	-	-	11.44	18.27	6.38	-	100.00	1732	4	116	Spongy

KU-567 243.20 mnz13	39.14	_	1.56	-	0.79	8.81	11.83	_	0.00	_	_	_	-	-	12.59	19.99	5.29	-	100.00	1741	5	113	Spongy
KU-568 59.80 mnz1	40.46	_	0.00	-	3.48	4.88	11.03	1.01	0.00	_	1.60	0.29	-	-	10.94	20.38	5.92	-	100.00	1814	6	77	Ambiguous
KU-568 59.80 mnz2	40.58	_	0.90	-	3.70	4.17	11.23	1.11	0.22	_	1.83	0.36	-	-	10.53	19.30	6.08	-	100.00	1834	7	105	Strain shadow type
KU-568 59.80 mnz3	40.13	_	0.00	-	0.76	9.84	11.27	_	_	_		0.25	-	-	11.60	19.72	6.43	-	100.00	1191	6	103	Ambiguous
KU-568 59.80 mnz4	41.19	_	0.00	-	7.22	3.57	11.26	_	_	_	1.90	0.31	-	-	9.94	18.63	5.97	-	100.00	1671	5	108	Ambiguous
KU-568 59.80 mnz5	40.33	_	0.00	-	4.39	4.49	11.73	1.27	-	_		_	-	-	11.26	20.04	6.50	-	100.00	1671	5	111	Ambiguous
KU-568 59.80 mnz6	40.27	_	0.00	-	5.73	2.64	12.14	_	-	_	1.10	_	-	-	11.05	20.69	6.38	-	100.00	1703	5	106	Spongy
KU-568 59.80 mnz7	40.41	_	0.00	-	7.70	3.47	11.48	_	-	_		_	-	-	10.83	20.35	5.75	-	100.00	1759	5	108	Spongy
KU-568 59.80 mnz8	41.49	_	0.00	-	4.93	3.27	11.24	_	-	_	1.23	_	-	-	11.16	20.38	6.30	-	100.00	1666	5	108	Spongy
KU-568 59.80 mnz9	40.62	_	0.00	-	3.77	4.20	11.66	0.83	-	_	1.68	_	-	-	11.02	20.04	6.19	-	100.00	1694	5	106	Spongy
KU-568 59.80 mnz10	40.69	_	0.00	-	4.01	4.37	11.45	1.03	-	_	1.82	_	-	-	10.52	19.75	6.36	-	100.00	1687	5	105	Ambiguous
KU-569 308.80 mnz1	38.41	_	_	_	4.61	8.58	9.82	1.62	-	_	3.11	_	-	_	10.52	18.56	4.76	-	100.00	1694	13	106	Strain shadow type
KU-569 308.80 mnz2	38.97	_	_	_	1.25	14.10	10.49	_	-	_	_	_	-	_	9.94	18.81	6.43	-	100.00	1687	13	105	Ambiguous
KU-569 308.80 mnz3a	42.18	_	_	_	2.23	11.21	10.60	_	-	_	_	_	-	_	10.51	16.45	6.82	-	100.00	2642	11	97	Both types
KU-569 308.80 xnt2(mnz3b)	40.15	_	_	_	2.38	12.63	9.60	0.93	-	_	_	_	-	_	10.55	18.84	4.93	-	100.00	1917	12	97	Both types
ORV KU-543 mnz1	39.87	_	0.00	_	4.85	4.43	11.73	_	_	_	_	_	_	_	10.95	20.45	7.72	-	100.00	1882	4	98	Spongy
ORV KU-543 mnz2	40.87	_	_	_	5.51	4.46	12.45	_	_	_	_	_	_	_	8.65	19.88	8.19	-	100.00	1737	5	113	Spongy
ORV KU-543 mnz3	40.52	_	0.00	_	6.14	3.60	11.83	_	_	_	_	_	_	_	10.24	20.60	7.07	-	100.00	1733	4	114	Spongy
ORV KU-543 mnz4	41.81	_	_	_	_	8.76	12.31	_	_	_	_	0.39	_	_	6.29	18.17	12.26	-	100.00	1882	4	98	Spongy
ORV KU-543 mnz5	41.18	_	_	_	_	9.36	12.07	_	_	_	_	_	_	_	7.85	20.37	9.16	-	100.00	1878	4	99	Spongy
ORV KU-543 mnz6	39.70	_	1.54	_	4.82	4.01	11.49	_	_	_	_	0.65	_	_	10.10	19.19	8.51	-	100.00	1766	5	110	Spongy
ORV KU-543 mnz7	40.16	_	_	_	0.69	8.84	11.74	_	_	_	_	_	_	_	10.75	20.59	7.24	-	100.00	1732	4	114	Ambiguous
ORV KU-543 mnz8	40.56	_	0.00	_	0.83	7.44	12.41	_	_	_	_	0.62	_	_	10.15	19.76	8.23	-	100.00	1743	4	113	Spongy
ORV KU-543 mnz9	39.33	_	0.00	_	0.51	9.48	11.84	_	_	_	_	_	_	_	12.28	20.73	5.82	-	100.00	1871	4	98	Spongy
ORV KU-582 mnz1	38.79	_	_	_	_	10.03	12.32	_	_	_	_	0.38	_	_	8.16	17.71	12.61	-	100.00	1916	24	57	Spongy
ORV KU-582 mnz2	37.86	_	_	_	_	10.20	12.42	_	_	_	_		_	_	7.86	19.99	11.67	-	100.00	1599	29	100	Spongy
ORV KU-582 mnz3	39.95	_	_	_	_	9.58	10.19	_	_	_	_	11.07	_	_	6.85	14.29	8.08	-	100.00	5503	21	161	Spongy
ORV KU-582 mnz4	40.53	_	8.59	_	_	10.37	_	_	_	_	_	10.98	_	_	6.59	15.08	7.86	-	100.00	5483	25	54	Spongy
ORV KU-582 mnz5	39.97	_	9.13	_	0.52	10.42	_	_	_	_	_	10.91	_	_	6.78	14.87	7.40	-	100.00	#NUM!	#NUM!	119	Spongy
ORV KU-582 mnz6	40.74	_	8.26	_	_	10.84	_	_	_	_	_	10.73	_	_	6.75	13.87	8.81	-	100.00	5309	46	111	Spongy
ORV KU-582 mnz7	36.96	_	_	_	_	9.88	11.63	_	_	_	_	0.84	_	_	7.84	18.68	11.79	2.37	100.00	#NUM!	#NUM!	86	Spongy
ORV KU-559 mnz1	39.58	_	_	_	3.87	8.90	10.85	_	_	_	_	_	_	_	9.26	20.69	6.85	_	100.00	1816	25	101	Spongy
ORV KU-559 mnz2	40.67	_	_	_	1.27	11.73	11.73	_	_	_	_	_	_	_	5.84	17.57	11.18	_	100.00	1948	24	97	Spongy
ORV KU-559 mnz3	40.02	_	_	_	_	13.92	10.84	_	_	_	_	_	_	_	7.67	19.36	8.19	_	100.00	1910	24	98	Spongy
Sarvisuo IA mnz1	41.45	_	1.42	_	2.72	5.78	12.08	-	_	_	-	0.89	_	_	6.50	18.11	11.05	_	100.00	1943	24	94	Spongy
Sarvisuo IA mnz2	40.49	_	0.00	_	2.69	5.22	12.03	-	_	_	_	_	_	_	11.63	21.44	6.50	_	100.00	1812	25	103	Ambiguous
Sarvisuo IA mnz3	41.85	_	0.00	_	3.67	5.15	11.43	0.38	_	_	1.12	0.44	_	_	9.60	19.17	7.18	_	100.00	1964	24	78	Ambiguous
Sarvisuo IA mnz4	40.26	_	0.00	_	2.97	7.09	11.64	_	_	_	_	_	_	_	11.10	19.99	6.95	_	100.00	1904	24	80	Spongy
Sarvisuo IA mnz5	42.15	_	_	_	2.65	5.73	12.60	0.34	_	_	_	_	_	_	6.96	19.07	10.50	_	100.00	1943	24	87	Both types
Sarvisuo IA mnz6	41.09	_	0.00	_	2.74	7.02	11.69	_	_	_	_	0.68	_	_	10.57	18.79	7.42	_	100.00	1844	25	84	Spongy
Sarvisuo IA mnz7	40.76	_	0.00	_	2.72	6.42	11.67	_	_	_	0.92	0.87	_	_	12.55	18.83	5.25	_	100.00	1926	24	79	Spongy
Sarvisuo IIA mnz1	40.98	_	0.00	_	3.08	6.72	11.87	_	_	_	_	_	_	_	8.50	20.20	8.64	-	100.00	2047	24	73	Spongy
Sarvisuo IIA mnz2	41.11	_	0.00	_	2.02	7.15	12.24	_	_	_	_	_	_	_	9.29	20.64	7.55	-	100.00	1834	25	103	Spongy
Sarvisuo IIA mnz3	42.55	_	0.00	_	2.70	7.35	11.46	_	_	_	0.92	0.44	_	_	9.55	18.32	6.70	-	100.00	1789	25	94	Spongy
Sarvisuo IIA mnz4	41.21	_	0.95	_	3.81	5.28	12.22	_	_	_	_	_	_	_	7.80	19.72	9.01	-	100.00	1928	24	97	Spongy
Sarvisuo IIA mnz5	39.88	_	2.58	_	3.25	5.45	11.54	_	0.00	_	_	_	_	_	9.19	20.36	7.76	-	100.00	1773	25	99	Spongy
Sarvisuo IIA mnz6	41.57	_	0.00	_	4.04	5.45	11.91	_	_	_	_	0.34	_	_	8.71	19.91	8.06	-	100.00	1953	24	90	Spongy
Sarvisuo IIA mnz7	42.76	_	0.00	_	2.47	7.12	12.06	_	_	_	_	0.38	_	_	7.65	18.48	9.08	-	100.00	1969	24	81	Spongy
Sarvisuo IIA mnz8	39.61	_	0.00	_	2.09	5.32	12.26	_	_	_	_	1.46	_	_	12.60	21.72	4.94	-	100.00	1846	25	96	Spongy
Sarvisuo IIA mnz9	39.67	_	1.12	_	3.19	6.03	11.66	_	0.00	_	_	0.43	_	_	7.36	17.59	10.77	2.16	100.00	1951	24	90	Spongy

Sarvisuo IIA mnz10	40.94	-	0.00	-	2.88	5.77	12.55	-	-	-	-	-	-	-	8.69	21.18	7.99	-	100.00	1827	25	103	Spongy
Sarvisuo IIA mnz11	39.82	-	-	-	6.12	11.02	8.38	-	-	-	-	0.46	-	-	10.16	17.68	6.36	-	100.00	2269	23	84	Spongy
Sarvisuo IIA mnz12	38.43	-	0.81	-	4.28	7.40	10.98	-	-	-	-	0.69	-	-	9.03	20.52	7.85	-	100.00	1968	24	84	Spongy
Sarvisuo IIA mnz13	39.99	-	1.12	-	3.42	5.74	11.98	-	-	-	-	0.68	-	-	9.14	19.22	8.72	-	100.00	2002	24	77	Spongy
Sarvisuo IIA mnz14	39.73	-	0.93	-	1.94	7.82	11.30	-	-	-	1.01	0.60	-	-	10.35	20.29	6.03	-	100.00	1838	25	101	Spongy
Sarvisuo IIA mnz15	42.43	-	0.00	-	3.38	5.52	11.89	-	-	-	-	0.87	-	-	7.28	19.21	9.43	-	100.00	1979	24	82	Spongy
Sarvisuo IIA mnz16	40.64	-	1.00	-	2.98	5.08	12.28	-	-	-	-	0.35	-	-	8.45	20.15	9.09	-	100.00	1977	24	91	Spongy
Sarvisuo IIA mnz17	41.74	-	0.00	-	3.45	6.90	11.75	-	-	-	-	0.36	-	-	6.85	18.34	10.61	-	100.00	2023	24	80	Spongy
Sarvisuo IIA mnz18	41.43	-	0.00	-	2.47	5.83	12.10	-	-	-	-	1.00	-	-	10.13	20.32	6.72	-	100.00	1882	25	102	Spongy
Sarvisuo IIA mnz19	39.86	-	1.05	-	4.67	5.51	11.47	-	0.00	-	1.11	0.34	-	-	7.84	18.55	9.61	-	100.00	1841	25	102	Ambiguous
Sarvisuo IIA mnz20	41.12	-	0.00	-	2.06	7.15	11.83	-	-	-	-	-	-	-	9.94	20.59	7.30	-	100.00	1964	24	88	Ambiguous
Sarvisuo IIA mnz21	46.84	-	2.64	-	5.34	6.28	9.73	-	0.00	-	-	-	-	-	8.43	15.51	5.23	-	100.00	1991	24	86	Ambiguous
Sarvisuo IIA mnz22	42.53	-	0.00	-	2.14	6.93	12.22	-	-	-	-	0.48	-	-	8.95	18.98	7.76	-	100.00	2113	24	81	Spongy
Sarvisuo IIA mnz23	42.93	-	0.00	-	4.16	5.72	11.99	-	-	-	-	0.44	-	-	6.04	17.98	10.74	-	100.00	1980	24	88	Ambiguous
Sarvisuo IIA mnz24	41.81	-	0.00	-	1.93	7.94	11.70	-	-	-	-	0.43	-	-	7.17	19.12	9.90	-	100.00	1982	24	91	Ambiguous
Sarvisuo IIA mnz25	40.24	-	0.84	-	2.58	7.15	11.96	-	-	-	-	-	-	-	6.58	19.64	11.01	-	100.00	1992	24	89	Ambiguous
Sarvisuo IIA mnz26	40.03	-	0.93	-	3.10	5.63	11.89	-	0.00	-	-	-	-	-	10.59	21.28	6.54	-	100.00	1862	25	102	Ambiguous
Sarvisuo IIA mnz27	41.18	-	0.89	-	2.36	7.26	11.63	-	-	-	-	0.52	-	-	8.76	20.40	6.99	-	100.00	1871	25	98	Spongy
Sarvisuo IIA mnz28	41.47	-	0.00	-	3.12	5.32	12.19	-	-	-	-	-	-	-	9.17	20.19	8.54	-	100.00	2004	24	90	Spongy
Sarvisuo IIA mnz29	40.68	-	0.00	-	2.00	4.99	12.44	-	-	-	-	1.14	-	-	9.29	21.15	8.32	-	100.00	2392	23	75	Spongy
Sarvisuo IIA mnz30	41.04	-	1.18	-	3.06	3.93	11.72	-	0.00	-	1.95	1.71	-	-	9.89	19.44	6.09	-	100.00	1835	25	84	Spongy
Sarvisuo IIA mnz31	40.46	-	1.26	-	1.98	7.92	11.88	-	-	-	-	-	-	-	10.58	19.48	6.45	-	100.00	2013	24	83	Spongy
Sarvisuo IIA mnz32	41.77	-	0.00	-	2.23	7.94	11.91	-	-	-	-	-	-	-	6.40	19.03	10.72	-	100.00	1989	24	90	Spongy
Sarvisuo IIA mnz33	27.63	-	0.75	-	4.64	11.14	7.35	-	-	-	-	0.52	-	-	12.91	26.01	9.05	-	100.00	2011	24	77	Spongy
Sarvisuo IIA mnz34	35.08	-	0.72	-	3.93	5.93	10.55	-	-	-	1.26	2.06	-	-	10.49	22.58	7.40	-	100.00	1937	24	77	Spongy
Sarvisuo IIA mnz35	39.94	-	1.00	-	3.10	6.16	11.84	-	-	-	-	-	-	-	9.97	19.88	8.11	-	100.00	1875	25	100	Ambiguous
Sarvisuo IIA mnz36	48.77	-	0.00	-	2.22	3.76	12.84	-	-	-	-	0.91	-	-	5.10	17.13	9.28	-	100.00	2935	22	103	Spongy
Sarvisuo IIA mnz37	40.58	-	1.36	-	2.82	6.12	11.81	-	0.00	-	-	0.47	-	-	8.09	17.84	10.90	-	100.00	1849	25	83	Spongy
Sarvisuo IIA mnz38	41.06	-	0.00	-	3.43	4.63	12.32	-	-	-	-	0.55	-	-	9.49	19.84	8.68	-	100.00	1985	24	86	Spongy
Sarvisuo IIA mnz39	33.70	-	0.00	-	2.59	7.11	10.62	-	-	-	-	0.66	-	-	11.63	24.41	9.27	-	100.00	1883	25	98	Ambiguous
Sarvisuo IIA mnz40	42.82	-	2.12	-	1.95	5.67	11.50	-	0.17	-	-	0.42	-	-	11.52	18.83	5.01	-	100.00	1878	25	87	Ambiguous

Supplementary Material Table 4: Concordance-filtered and texture-sorted concentrated data for monazite grains from Kutemajärvi samples.

Single-grain	O	Mg	F	Br	Al	Si	P	K	Ni	Cu	Ag	Ca	Fe	Y	La	Ce	Nd	Sm	Total	$^{207}Pb/^{206}Pb$ Age (Ma)	1s	Concordance	Textural setting
KOH-8 95.20 mnz8	40.37	-	0.00	-	6.51	6.11	10.35	1.65	-	-	-	0.75	-	-	9.83	17.86	6.57	-	100.00	1892	4	98	Ambiguous
KOH-8 95.20 mnz14	41.38	-	_	_	6.23	5.61	10.41	1.53	-	-	_	1.78	-	-	9.40	17.02	6.65	-	100.00	1768	4	103	Ambiguous
KOH-15 mnz2	43.55	-	_	_	0.62	9.16	12.32	_	_	_	_	0.81	-	-	4.22	16.98	12.33	-	100.00	1894	12	96	Ambiguous
KOH-15 mnz3	40.49	-	_	_	0.39	9.74	11.51	_	_	_	_	0.54	-	-	9.19	19.73	8.41	-	100.00	1866	12	99	Ambiguous
KOH-24x mnz10	40.59	_	_	_	7.73	4.81	10.33	0.73	-	-	_	_	-	-	8.55	18.68	8.59	-	100.00	1834	13	105	Ambiguous
KOH-24x mnz11	43.70	_	_	_	9.45	4.62	10.69	_	_	_	_	_	-	-	7.98	17.94	5.62	-	100.00	1191	14	103	Ambiguous
KU-567 243.20 mnz3	41.01	_	0.00	-	1.37	8.38	12.08	_	-	_	_	_	-	-	10.81	20.29	6.06	-	100.00	1894	4	96	Ambiguous
KU-567 243.20 mnz4	40.22	_	0.00	-	2.02	7.59	11.78	0.37	-	_	_	_	-	-	13.05	19.91	5.05	-	100.00	1866	4	99	Ambiguous
KU-568 59.80 mnz3	40.13	_	0.00	-	0.76	9.84	11.27	_	_	_	_	0.25	-	-	11.60	19.72	6.43	-	100.00	1191	6	103	Ambiguous
Sarvisuo IA mnz2	40.49	_	0.00	_	2.69	5.22	12.03	-	_	_	_	_	_	_	11.63	21.44	6.50	_	100.00	1812	25	103	Ambiguous
Sarvisuo IIA mnz19	39.86	_	1.05	_	4.67	5.51	11.47	_	0.00	_	1.11	0.34	_	_	7.84	18.55	9.61	_	100.00	1841	25	102	Ambiguous
Sarvisuo IIA mnz26	40.03	_	0.93	_	3.10	5.63	11.89	_	0.00	_	_	_	_	_	10.59	21.28	6.54	_	100.00	1862	25	102	Ambiguous
Sarvisuo IIA mnz35	39.94	_	1.00	_	3.10	6.16	11.84	_	_	_	_	_	_	_	9.97	19.88	8.11	_	100.00	1875	25	100	Ambiguous
Sarvisuo IIA mnz39	33.70	_	0.00	_	2.59	7.11	10.62	_	_	_	_	0.66	_	_	11.63	24.41	9.27	_	100.00	1883	25	98	Ambiguous
KOH-8 95.20 mnz6	38.72	-	-	-	4.41	5.16	12.21	1.20	-	-	-	1.76	-	-	8.41	19.20	8.94	-	100.00	1889	4	100	Both types
KOH-8 95.20 mnz11	42.23	-	0.00	-	4.57	6.16	11.56	1.03	-	-	-	1.94	-	-	6.65	16.49	9.38	-	100.00	1870	4	98	Both types
KOH-8 95.20 mnz16	39.27	-	_	_	3.13	9.01	11.18	0.81	-	-	_	0.75	-	-	9.85	18.94	7.06	-	100.00	1868	5	99	Both types
KU-569 308.80 mnz3a	42.18	_	_	_	2.23	11.21	10.60	_	-	_	_	_	-	_	10.51	16.45	6.82	-	100.00	2642	11	97	Both types
KU-569 308.80 xnt2(mnz3b)	40.15	_	_	_	2.38	12.63	9.60	0.93	-	_	_	_	-	_	10.55	18.84	4.93	-	100.00	1917	12	97	Both types
KOH-8 95.20 mnz4	39.57	-	-	-	6.81	5.78	10.84	1.74	-	-	-	-	-	-	10.30	18.59	6.37	-	100.00	1839	4	100	Spongy
KOH-8 95.20 mnz5	39.74	-	1.45	-	3.67	4.10	12.12	1.04	-	-	-	3.17	-	-	10.43	17.80	6.46	-	100.00	1861	4	96	Spongy
KOH-8 95.20 mnz7	40.35	-	0.00	-	7.40	6.58	10.22	1.79	-	-	-	-	-	-	8.31	18.09	7.26	-	100.00	1869	4	101	Spongy
KOH-8 95.20 mnz9	40.43	-	-	-	3.41	10.85	10.62	0.93	-	-	-	-	-	-	7.87	18.57	7.32	-	100.00	1870	4	100	Spongy
KOH-8 95.20 mnz10	39.78	-	0.00	-	4.70	5.48	11.17	1.23	-	-	-	1.17	-	-	9.73	18.59	8.15	-	100.00	1877	4	101	Spongy
KOH-8 95.20 mnz13	38.48	-	0.00	-	2.70	5.56	12.03	0.72	-	-	-	1.98	-	-	8.51	18.77	3.07	-	100.00	1874	4	96	Spongy
ORV KU-543 mnz1	39.87	_	0.00	_	4.85	4.43	11.73	_	_	_	_	_	_	_	10.95	20.45	7.72	-	100.00	1882	4	98	Spongy
ORV KU-543 mnz4	41.81	_	_	_	_	8.76	12.31	_	_	_	_	0.39	_	_	6.29	18.17	12.26	-	100.00	1882	4	98	Spongy
ORV KU-543 mnz5	41.18	_	_	_	_	9.36	12.07	_	_	_	_	_	_	_	7.85	20.37	9.16	-	100.00	1878	4	99	Spongy
ORV KU-543 mnz9	39.33	_	0.00	_	0.51	9.48	11.84	_	_	_	_	_	_	_	12.28	20.73	5.82	-	100.00	1871	4	98	Spongy
ORV KU-582 mnz2	37.86	_	_	_	_	10.20	12.42	_	_	_	_	_	_	_	7.86	19.99	11.67	-	100.00	1599	29	100	Spongy
ORV KU-559 mnz1	39.58	_	_	_	3.87	8.90	10.85	_	_	_	_	_	_	_	9.26	20.69	6.85	_	100.00	1816	25	101	Spongy
ORV KU-559 mnz2	40.67	_	_	_	1.27	11.73	11.73	_	_	_	_	_	_	_	5.84	17.57	11.18	_	100.00	1948	24	97	Spongy
ORV KU-559 mnz3	40.02	_	_	_	_	13.92	10.84	_	_	_	_	_	_	_	7.67	19.36	8.19	_	100.00	1910	24	98	Spongy
Sarvisuo IIA mnz2	41.11	_	0.00	_	2.02	7.15	12.24	_	_	_	_	_	_	_	9.29	20.64	7.55	-	100.00	1834	25	103	Spongy
Sarvisuo IIA mnz4	41.21	_	0.95	_	3.81	5.28	12.22	_	_	_	_	_	_	_	7.80	19.72	9.01	-	100.00	1928	24	97	Spongy
Sarvisuo IIA mnz5	39.88	_	2.58	_	3.25	5.45	11.54	_	0.00	_	_	_	_	_	9.19	20.36	7.76	-	100.00	1773	25	99	Spongy
Sarvisuo IIA mnz8	39.61	_	0.00	_	2.09	5.32	12.26	_	_	_	_	1.46	_	_	12.60	21.72	4.94	-	100.00	1846	25	96	Spongy
Sarvisuo IIA mnz10	40.94	_	0.00	_	2.88	5.77	12.55	_	_	_	_	_	_	_	8.69	21.18	7.99	_	100.00	1827	25	103	Spongy
Sarvisuo IIA mnz14	39.73	_	0.93	_	1.94	7.82	11.30	_	_	_	1.01	0.60	_	_	10.35	20.29	6.03	-	100.00	1838	25	101	Spongy
Sarvisuo IIA mnz18	41.43	_	0.00	_	2.47	5.83	12.10	_	_	_	_	1.00	_	_	10.13	20.32	6.72	_	100.00	1882	25	102	Spongy
Sarvisuo IIA mnz27	41.18	_	0.89	_	2.36	7.26	11.63	_	_	_	_	0.52	_	_	8.76	20.40	6.99	_	100.00	1871	25	98	Spongy
Sarvisuo IIA mnz36	48.77	_	0.00	_	2.22	3.76	12.84	_	_	_	_	0.91	_	_	5.10	17.13	9.28	_	100.00	2935	22	103	Spongy
KOH-8 95.20 mnz2	40.47	-	-	-	6.13	6.81	10.79	1.84	-	-	-	0.88	-	-	6.69	17.47	8.91	-	100.00	1858	4	100	Strain shadow type
KOH-8 95.20 mnz3	40.82	-	0.00	-	4.96	8.26	10.23	1.12	-	-	1.43	0.93	-	-	8.55	16.82	6.88	-	100.00	1876	4	95	Strain shadow type
KU-568 59.80 mnz2	40.58	_	0.90	-	3.70	4.17	11.23	1.11	0.22	_	1.83	0.36	-	-	10.53	19.30	6.08	-	100.00	1834	7	105	Strain shadow type

Supplementary Material Table 5: Concordance-filtered and mineralogy-sorted concentrated data for monazite grains from Kutemajärvi samples.

Single-grain	O	Mg	F	Br	Al	Si	P	K	Ni	Cu	Ag	Ca	Fe	Y	La	Ce	Nd	Sm	Total	$^{207}Pb/^{206}Pb$ Age (Ma)	1s	Concordance	Textural setting	Mineralogy	Lithology (Map of Kinnunen, 2008)
KOH-8 95.20 mnz8	40.37	-	0.00	-	6.51	6.11	10.35	1.65	-	-	-	0.75	-	-	9.83	17.86	6.57	-	100.00	1892	4	98	Ambiguous	M: quartz, sericite, chlorite A: opaque, fluorite, tourmaline, epidote	Sericite-dominant schists
KOH-8 95.20 mnz14	41.38	-	-	-	6.23	5.61	10.41	1.53	-	-	-	1.78	-	-	9.40	17.02	6.65	-	100.00	1768	4	103	Ambiguous	M: quartz, sericite, chlorite A: opaque, fluorite, tourmaline, epidote	Sericite-dominant schists
KOH-8 95.20 mnz6	38.72	-	-	-	4.41	5.16	12.21	1.20	-	-	-	1.76	-	-	8.41	19.20	8.94	-	100.00	1889	4	100	Both types	M: quartz, sericite, chlorite A: opaque, fluorite, tourmaline, epidote	Sericite-dominant schists
KOH-8 95.20 mnz11	42.23	-	0.00	-	4.57	6.16	11.56	1.03	-	-	-	1.94	-	-	6.65	16.49	9.38	-	100.00	1870	4	98	Both types	M: quartz, sericite, chlorite A: opaque, fluorite, tourmaline, epidote	Sericite-dominant schists
KOH-8 95.20 mnz16	39.27	-	-	-	3.13	9.01	11.18	0.81	-	-	-	0.75	-	-	9.85	18.94	7.06	-	100.00	1868	5	99	Both types	M: quartz, sericite, chlorite A: opaque, fluorite, tourmaline, epidote	Sericite-dominant schists
KOH-8 95.20 mnz4	39.57	-	-	-	6.81	5.78	10.84	1.74	-	-	-	-	-	-	10.30	18.59	6.37	-	100.00	1839	4	100	Spongy	M: quartz, sericite, chlorite A: opaque, fluorite, tourmaline, epidote	Sericite-dominant schists
KOH-8 95.20 mnz5	39.74	-	1.45	-	3.67	4.10	12.12	1.04	-	-	-	3.17	-	-	10.43	17.80	6.46	-	100.00	1861	4	96	Spongy	M: quartz, sericite, chlorite A: opaque, fluorite, tourmaline, epidote	Sericite-dominant schists
KOH-8 95.20 mnz7	40.35	-	0.00	-	7.40	6.58	10.22	1.79	-	-	-	-	-	-	8.31	18.09	7.26	-	100.00	1869	4	101	Spongy	M: quartz, sericite, chlorite A: opaque, fluorite, tourmaline, epidote	Sericite-dominant schists
KOH-8 95.20 mnz9	40.43	-	-	-	3.41	10.85	10.62	0.93	-	-	-	-	-	-	7.87	18.57	7.32	-	100.00	1870	4	100	Spongy	M: quartz, sericite, chlorite A: opaque, fluorite, tourmaline, epidote	Sericite-dominant schists
KOH-8 95.20 mnz10	39.78	-	0.00	-	4.70	5.48	11.17	1.23	-	-	-	1.17	-	-	9.73	18.59	8.15	-	100.00	1877	4	101	Spongy	M: quartz, sericite, chlorite A: opaque, fluorite, tourmaline, epidote	Sericite-dominant schists
KOH-8 95.20 mnz13	38.48	-	0.00	-	2.70	5.56	12.03	0.72	-	-	-	1.98	-	-	8.51	18.77	3.07	-	100.00	1874	4	96	Spongy	M: quartz, sericite, chlorite A: opaque, fluorite, tourmaline, epidote	Sericite-dominant schists
KOH-8 95.20 mnz2	40.47	-	-	-	6.13	6.81	10.79	1.84	-	-	-	0.88	-	-	6.69	17.47	8.91	-	100.00	1858	4	100	Strain shadow type	M: quartz, sericite, chlorite A: opaque, fluorite, tourmaline, epidote	Sericite-dominant schists
KOH-8 95.20 mnz3	40.82	-	0.00	-	4.96	8.26	10.23	1.12	-	-	1.43	0.93	-	-	8.55	16.82	6.88	-	100.00	1876	4	95	Strain shadow type	M: quartz, sericite, chlorite A: opaque, fluorite, tourmaline, epidote	Sericite-dominant schists
KOH-15 mnz2	43.55	-	-	-	0.62	9.16	12.32	-	-	-	-	0.81	-	-	4.22	16.98	12.33	-	100.00	1894	12	96	Ambiguous	M: quartz, phlogopite, andalusite A: opaque, hematite, sericite	Quartz-dominant schists with topaz and andalusite
KOH-15 mnz3	40.49	-	-	-	0.39	9.74	11.51	-	-	-	-	0.54	-	-	9.19	19.73	8.41	-	100.00	1866	12	99	Ambiguous	M: quartz, phlogopite, andalusite A: opaque, hematite, sericite	Quartz-dominant schists with topaz and andalusite
KOH-24x mnz10	40.59	-	-	-	7.73	4.81	10.33	0.73	-	-	-	-	-	-	8.55	18.68	8.59	-	100.00	1834	13	105	Ambiguous	M: andalusite, biotite, kaolinite, quartz, sericite A: zircons, phlogopite, epidote	Quartz-dominant schists with sericite and chlorite
KOH-24x mnz11	43.70	-	-	-	9.45	4.62	10.69	-	-	-	-	-	-	-	7.98	17.94	5.62	-	100.00	1191	14	103	Ambiguous	M: andalusite, biotite, kaolinite, quartz, sericite A: zircons, phlogopite, epidote	Quartz-dominant schists with sericite and chlorite
KU-567 243.20 mnz3	41.01	-	0.00	-	1.37	8.38	12.08	-	-	-	-	-	-	-	10.81	20.29	6.06	-	100.00	1894	4	96	Ambiguous	M: quartz, sericite/muscovite, phlogopite, andalusite A: opaque, zircons, monazite	Chlorite-dominant schists
KU-567 243.20 mnz4	40.22	-	0.00	-	2.02	7.59	11.78	0.37	-	-	-	-	-	-	13.05	19.91	5.05	-	100.00	1866	4	99	Ambiguous	M: quartz, sericite/muscovite, phlogopite, andalusite A: opaque, zircons, monazite	Chlorite-dominant schists
KU-568 59.80 mnz3	40.13	-	0.00	-	0.76	9.84	11.27	-	-	-	-	0.25	-	-	11.60	19.72	6.43	-	100.00	1191	6	103	Ambiguous	M: quartz, sericite, kaolinite, pyrophyllite A: opaque, monazite	Chlorite-dominants schists
KU-568 59.80 mnz2	40.58	-	0.90	-	3.70	4.17	11.23	1.11	0.22	-	1.83	0.36	-	-	10.53	19.30	6.08	-	100.00	1834	7	105	Strain shadow type	M: quartz, sericite, kaolinite, pyrophyllite A: opaque, monazite	Chlorite-dominants schists
KU-569 308.80 mnz3a	42.18	-	-	-	2.23	11.21	10.60	-	-	-	-	-	-	-	10.51	16.45	6.82	-	100.00	2642	11	97	Both types	M: quartz, phlogopite, sericite A: opaque, chlorite, monazite	Sericite-dominant schists/Chlorite-dominants schist boundary
KU-569 308.80 xnt2(mnz3b)	40.15	-	-	-	2.38	12.63	9.60	0.93	-	-	-	-	-	-	10.55	18.84	4.93	-	100.00	1917	12	97	Both types	M: quartz, phlogopite, sericite A: opaque, chlorite, monazite	Sericite-dominant schists/Chlorite-dominants schist boundary
ORV KU-543 mnz1	39.87	-	0.00	-	4.85	4.43	11.73	-	-	-	-	-	-	-	10.95	20.45	7.72	-	100.00	1882	4	98	Spongy	M: quartz, sericite, kaolinite, andalusite, pyrophyllite, apatite? A: opaque	Sericite-dominant schists
ORV KU-543 mnz4	41.81	-	-	-	-	8.76	12.31	-	-	-	-	0.39	-	-	6.29	18.17	12.26	-	100.00	1882	4	98	Spongy	M: quartz, sericite, kaolinite, andalusite, pyrophyllite, apatite? A: opaque	Sericite-dominant schists
ORV KU-543 mnz5	41.18	-	-	-	-	9.36	12.07	-	-	-	-	-	-	-	7.85	20.37	9.16	-	100.00	1878	4	99	Spongy	M: quartz, sericite, kaolinite, andalusite, pyrophyllite, apatite? A: opaque	Sericite-dominant schists
ORV KU-543 mnz9	39.33	-	0.00	-	0.51	9.48	11.84	-	-	-	-	-	-	-	12.28	20.73	5.82	-	100.00	1871	4	98	Spongy	M: quartz, sericite, kaolinite, andalusite, pyrophyllite, apatite? A: opaque	Sericite-dominant schists
ORV KU-559 mnz1	39.58	-	-	-	3.87	8.90	10.85	-	-	-	-	-	-	-	9.26	20.69	6.85	-	100.00	1816	25	101	Spongy	M: quartz, pyrophyllite, andalusite A: muscovite, diaspore, opaque, rutile	Quartz rock/quartz schist, sericite-quartz schist
ORV KU-559 mnz2	40.67	-	-	-	1.27	11.73	11.73	-	-	-	-	-	-	-	5.84	17.57	11.18	-	100.00	1948	24	97	Spongy	M: quartz, pyrophyllite, andalusite A: muscovite, diaspore, opaque, rutile	Quartz rock/quartz schist, sericite-quartz schist
ORV KU-559 mnz3	40.02	-	-	-	-	13.92	10.84	-	-	-	-	-	-	-	7.67	19.36	8.19	-	100.00	1910	24	98	Spongy	M: quartz, pyrophyllite, andalusite A: muscovite, diaspore, opaque, rutile	Quartz rock/quartz schist, sericite-quartz schist
ORV KU-582 mnz2	37.86	-	-	-	-	10.20	12.42	-	-	-	-	-	-	-	7.86	19.99	11.67	-	100.00	1599	29	100	Spongy	M: quartz, sericite	Quartz rock/quartz schist, sericite quartz schist
Sarvisuo IA mnz2	40.49	-	0.00	-	2.69	5.22	12.03	-	-	-	-	-	-	-	11.63	21.44	6.50	-	100.00	1812	25	103	Ambiguous	M: quartz, pyrohphyllite, kaolinite, andalusite A: opaque, rutile, hematite	Quartz-dominant schist with sericite
Sarvisuo IIA mnz19	39.86	-	1.05	-	4.67	5.51	11.47	-	0.00	-	1.11	0.34	-	-	7.84	18.55	9.61	-	100.00	1841	25	102	Ambiguous	M: quartz, kaolinite, pyrophyllite, andalusite A: opaque, zircons	Quartz-dominant schist with sericite
Sarvisuo IIA mnz26	40.03	-	0.93	-	3.10	5.63	11.89	-	0.00	-	-	-	-	-	10.59	21.28	6.54	-	100.00	1862	25	102	Ambiguous	M: quartz, kaolinite, pyrophyllite, andalusite A: opaque, zircons	Quartz-dominant schist with sericite
Sarvisuo IIA mnz35	39.94	-	1.00	-	3.10	6.16	11.84	-	-	-	-	-	-	-	9.97	19.88	8.11	-	100.00	1875	25	100	Ambiguous	M: quartz, kaolinite, pyrophyllite, andalusite A: opaque, zircons	Quartz-dominant schist with sericite
Sarvisuo IIA mnz39	33.70	-	0.00	-	2.59	7.11	10.62	-	-	-	-	0.66	-	-	11.63	24.41	9.27	-	100.00	1883	25	98	Ambiguous	M: quartz, kaolinite, pyrophyllite, andalusite A: opaque, zircons	Quartz-dominant schist with sericite
Sarvisuo IIA mnz2	41.11	-	0.00	-	2.02	7.15	12.24	-	-	-	-	-	-	-	9.29	20.64	7.55	-	100.00	1834	25	103	Spongy	M: quartz, kaolinite, pyrophyllite, andalusite A: opaque, zircons	Quartz-dominant schist with sericite
Sarvisuo IIA mnz4	41.21	-	0.95	-	3.81	5.28	12.22	-	-	-	-	-	-	-	7.80	19.72	9.01	-	100.00	1928	24	97	Spongy	M: quartz, kaolinite, pyrophyllite, andalusite A: opaque, zircons	Quartz-dominant schist with sericite
Sarvisuo IIA mnz5	39.88	-	2.58	-	3.25	5.45	11.54	-	0.00	-	-	-	-	-	9.19	20.36	7.76	-	100.00	1773	25	99	Spongy	M: quartz, kaolinite, pyrophyllite, andalusite A: opaque, zircons	Quartz-dominant schist with sericite
Sarvisuo IIA mnz8	39.61	-	0.00	-	2.09	5.32	12.26	-	-	-	-	1.46	-	-	12.60	21.72	4.94	-	100.00	1846	25	96	Spongy	M: quartz, kaolinite, pyrophyllite, andalusite A: opaque, zircons	Quartz-dominant schist with sericite
Sarvisuo IIA mnz10	40.94	-	0.00	-	2.88	5.77	12.55	-	-	-	-	-	-	-	8.69	21.18	7.99	-	100.00	1827	25	103	Spongy	M: quartz, kaolinite, pyrophyllite, andalusite A: opaque, zircons	Quartz-dominant schist with sericite
Sarvisuo IIA mnz14	39.73	-	0.93	-	1.94	7.82	11.30	-	-	-	1.01	0.60	-	-	10.35	20.29	6.03	-	100.00	1838	25	101	Spongy	M: quartz, kaolinite, pyrophyllite, andalusite A: opaque, zircons	Quartz-dominant schist with sericite
Sarvisuo IIA mnz18	41.43	-	0.00	-	2.47	5.83	12.10	-	-	-	-	1.00	-	-	10.13	20.32	6.72	-	100.00	1882	25	102	Spongy	M: quartz, kaolinite, pyrophyllite, andalusite A: opaque, zircons	Quartz-dominant schist with sericite
Sarvisuo IIA mnz27	41.18	-	0.89	-	2.36	7.26	11.63	-	-	-	-	0.52	-	-	8.76	20.40	6.99	-	100.00	1871	25	98	Spongy	M: quartz, kaolinite, pyrophyllite, andalusite A: opaque, zircons	Quartz-dominant schist with sericite
Sarvisuo IIA mnz36	48.77	-	0.00	-	2.22	3.76	12.84	-	-	-	-	0.91	-	-	5.10	17.13	9.28	-	100.00	2935	22	103	Spongy	M: quartz, kaolinite, pyrophyllite, andalusite A: opaque, zircons	Quartz-dominant schist with sericite

Supplementary Material Table 6: LA-ICP-MS U-Pb data for monazite grains from sample A1447 of Mänttäri et al. (1997).

	Concentration in ppm			Isotopic ratios							Age (Ma)						
Sample-grain	Pb	Th	U	$^{206}Pb/^{204}Pb$	$^{207}Pb/^{206}Pb$	1s	$^{207}Pb/^{235}U$	1s	$^{206}Pb/^{238}U$	1s	r	$^{207}Pb/^{206}Pb$	1s	$^{207}Pb/^{235}U$	1s	$^{206}Pb/^{238}U$	1s	Concordance %
A1447_mnz01	270	1156	507	1895	0.1057	0.0012	4.926	0.135	0.338	0.011	0.94	1727	20	1807	23	1877	50	102
A1447_mnz02	767	8354	45	50112	0.1061	0.0024	5.385	0.179	0.368	0.012	0.76	1733	41	1882	28	2021	56	116
A1447_mnz03	247	1714	235	241991	0.1086	0.0012	5.140	0.142	0.343	0.011	0.93	1777	21	1843	23	1902	51	107
A1447_mnz04	964	9243	403	3796	0.1084	0.0013	5.087	0.141	0.340	0.011	0.92	1773	22	1834	23	1888	51	103
A1447_mnz05	236	2058	114	118691	0.1104	0.0020	5.243	0.160	0.344	0.011	0.83	1806	32	1860	26	1908	52	106
A1447_mnz06	432	3837	184	1445	0.0999	0.0015	4.613	0.134	0.335	0.011	0.88	1622	28	1752	24	1862	51	105
A1447_mnz07	1042	11180	64	68388	0.1077	0.0017	5.260	0.156	0.354	0.011	0.86	1760	29	1862	25	1955	53	111
A1447_mnz08	270	2119	225	227853	0.1100	0.0017	5.081	0.148	0.335	0.011	0.88	1799	28	1833	24	1863	51	104
A1447_mnz09	768	7279	211	211171	0.1114	0.0018	5.080	0.149	0.331	0.010	0.87	1822	28	1833	25	1842	50	101
A1447_mnz10	607	5539	265	266426	0.1102	0.0015	5.034	0.144	0.331	0.010	0.90	1802	25	1825	24	1845	50	102
A1447_mnz11	140	960	168	167960	0.1100	0.0025	5.011	0.167	0.330	0.011	0.76	1800	41	1821	28	1840	51	102
A1447_mnz12	338	2591	284	284811	0.1101	0.0014	5.008	0.141	0.330	0.010	0.91	1801	23	1821	24	1838	50	102
A1447_mnz13	1384	13957	398	401148	0.1113	0.0012	5.082	0.139	0.331	0.010	0.94	1821	20	1833	23	1844	50	101
A1447_mnz14	425	4324	35	35997	0.1082	0.0029	5.087	0.184	0.341	0.011	0.69	1769	49	1834	30	1892	54	107
A1447_mnz15	333	3366	29	30964	0.1125	0.0037	5.376	0.215	0.347	0.012	0.62	1839	58	1881	34	1919	56	104
A1447_mnz16	904	9329	262	263754	0.1121	0.0016	5.096	0.147	0.330	0.010	0.88	1833	26	1835	24	1837	50	100
A1447_mnz17	585	5402	238	1998	0.1067	0.0012	4.861	0.133	0.330	0.010	0.94	1743	20	1795	23	1841	50	100
A1447_mnz18	257	2059	180	187017	0.1125	0.0013	5.226	0.145	0.337	0.010	0.93	1841	21	1857	23	1871	50	102
A1447_mnz19	636	5898	203	1839	0.1067	0.0012	4.926	0.135	0.335	0.010	0.93	1744	21	1807	23	1861	50	100
A1447_mnz20	676	6168	236	244547	0.1131	0.0012	5.236	0.143	0.336	0.010	0.94	1850	20	1858	23	1866	50	101
A1447_mnz21	2380	23485	291	49	0.1618	0.0016	8.824	0.237	0.396	0.012	0.95	2475	16	2320	24	2148	57	69
A1447_mnz22	274	2514	95	99425	0.1132	0.0017	5.250	0.152	0.336	0.011	0.88	1852	27	1861	24	1868	51	101
A1447_mnz23	326	3235	106	110450	0.1149	0.0017	5.304	0.153	0.335	0.011	0.89	1878	26	1870	24	1862	51	99
A1447_mnz24	285	2153	248	255364	0.1131	0.0014	5.167	0.143	0.331	0.010	0.92	1850	21	1847	23	1845	50	100
A1447_mnz25	180	1407	133	137020	0.1134	0.0015	5.194	0.146	0.332	0.010	0.91	1855	23	1852	24	1849	50	100
A1447_mnz26	247	1934	193	197518	0.1147	0.0014	5.199	0.144	0.329	0.010	0.93	1875	21	1852	23	1833	50	98
A1447_mnz27	547	4880	236	244802	0.1146	0.0013	5.259	0.144	0.333	0.010	0.93	1873	20	1862	23	1853	50	99
A1447_mnz28	241	1524	189	86	0.0870	0.0009	3.876	0.105	0.323	0.010	0.95	1361	19	1609	22	1805	49	67

Supplementary Material Table 7: LA-ICP-MS U-Pb data for zircon grains from sample A1447 of Mänttäri et al. (1997).

Sample-grain	Concentration in ppm			Isotopic ratios									Age (Ma)						
	Pb	Th	U	$^{206}Pb/^{204}Pb$	$^{206}Pbc(\%)$	$^{207}Pb/^{206}Pb$	1s	$^{207}Pb/^{235}U$	1s	$^{206}Pb/^{238}U$	1s	r	$^{207}Pb/^{206}Pb$	1s	$^{207}Pb/^{235}U$	1s	$^{206}Pb/^{238}U$	1s	Concordance %
A1447_zr01	67	64	161	978	1.7603	0.1079	0.0010	5.059	0.110	0.340	0.007	0.90	1764	17	1829	18	1888	33	107
A1447_zr02	98	115	246	1421	1.2114	0.1118	0.0012	4.930	0.110	0.320	0.007	0.88	1828	20	1807	19	1789	32	98
A1447_zr03	63	46	161	1600	1.0759	0.1079	0.0010	5.005	0.108	0.336	0.007	0.91	1765	16	1820	18	1869	33	106
A1447_zr04	252	103	201	35	48.8358	0.2127	0.0014	11.205	0.233	0.382	0.008	0.95	2927	10	2540	19	2086	36	71
A1447_zr05	64	59	154	2575	0.6684	0.1116	0.0011	5.396	0.120	0.351	0.007	0.89	1825	19	1884	19	1938	34	106
A1447_zr06	34	27	87	790	2.1801	0.0991	0.0011	4.522	0.102	0.331	0.007	0.87	1607	21	1735	19	1843	33	115
A1447_zr07	95	81	247	4076	0.4223	0.1119	0.0012	5.116	0.115	0.332	0.007	0.87	1830	20	1839	19	1846	33	101
A1447_zr08	59	73	131	865	1.9903	0.1098	0.0014	5.421	0.125	0.358	0.007	0.85	1796	22	1888	20	1973	35	110
A1447_zr09	45	35	115	216382	0.0080	0.1151	0.0012	5.368	0.118	0.338	0.007	0.89	1882	18	1880	19	1878	33	100
A1447_zr10	116	83	176	92	18.7516	0.1233	0.0009	5.758	0.121	0.339	0.007	0.94	2005	13	1940	18	1880	33	94
A1447_zr11	186	135	325	116	14.8167	0.1147	0.0011	5.070	0.111	0.321	0.007	0.89	1875	18	1831	18	1793	32	96
A1447_zr12	60	60	145	591	2.9110	0.0975	0.0010	4.484	0.100	0.334	0.007	0.88	1576	19	1728	18	1856	33	118
A1447_zr13	49	36	126	160	10.7519	0.0278	0.0003	1.157	0.025	0.302	0.006	0.90	#NUM!	#NUM!	781	12	1702	30	#NUM!
A1447_zr14	69	64	153	841	2.0459	0.1138	0.0011	5.689	0.126	0.363	0.007	0.89	1861	18	1930	19	1995	35	107
A1447_zr15	81	105	187	2273	0.7573	0.1125	0.0015	5.457	0.129	0.352	0.007	0.83	1841	24	1894	20	1943	35	106
A1447_zr16	104	87	176	128	13.4015	0.1146	0.0009	5.443	0.115	0.345	0.007	0.93	1873	14	1892	18	1909	33	102
A1447_zr17	175	64	188	31	55.0686	0.2885	0.0020	9.966	0.209	0.251	0.005	0.94	3409	11	2432	19	1441	26	42
A1447_zr18	117	140	281	536778	0.0032	0.1166	0.0010	5.546	0.120	0.345	0.007	0.91	1904	16	1908	18	1911	33	100
A1447_zr19	151	101	225	91	19.0185	0.1223	0.0009	5.740	0.121	0.341	0.007	0.94	1989	13	1937	18	1889	33	95
A1447_zr20	85	64	172	176	9.7564	0.1152	0.0011	5.091	0.111	0.320	0.007	0.91	1884	17	1835	18	1792	32	95
A1447_zr21	53	47	131	2447	0.7036	0.1115	0.0012	5.256	0.117	0.342	0.007	0.88	1824	19	1862	19	1896	33	104
A1447_zr22	258	294	624	8722	0.1974	0.1169	0.0010	5.484	0.118	0.340	0.007	0.92	1909	15	1898	18	1888	33	99
A1447_zr23	85	78	209	1255	1.3715	0.1129	0.0010	5.233	0.112	0.336	0.007	0.92	1846	15	1858	18	1868	33	101
A1447_zr24	44	32	112	833	2.0677	0.1103	0.0013	4.937	0.112	0.325	0.007	0.86	1805	21	1809	19	1812	32	100
A1447_zr25	80	90	198	369238	0.0047	0.1171	0.0013	5.456	0.124	0.338	0.007	0.87	1913	20	1894	19	1876	33	98
A1447_zr26	36	35	90	169488	0.0102	0.1154	0.0013	5.392	0.122	0.339	0.007	0.87	1887	20	1884	19	1881	33	100
A1447_zr27	63	75	150	1118	1.5397	0.1052	0.0010	4.942	0.109	0.341	0.007	0.89	1717	18	1809	18	1891	33	110
A1447_zr28	27	22	71	1090	1.5799	0.1077	0.0015	4.849	0.117	0.327	0.007	0.81	1760	26	1793	20	1822	33	104
A1447_zr29	70	68	168	326009	0.0053	0.1157	0.0013	5.588	0.127	0.350	0.007	0.86	1891	21	1914	19	1936	34	102
A1447_zr30	57	42	137	611	2.8192	0.1117	0.0011	5.175	0.113	0.336	0.007	0.90	1827	17	1848	18	1867	33	102
A1447_zr31	57	57	142	1993	0.8636	0.1094	0.0012	5.095	0.114	0.338	0.007	0.88	1790	19	1835	19	1875	33	105
A1447_zr32	34	28	85	1456	1.1823	0.1072	0.0012	5.007	0.114	0.339	0.007	0.86	1752	21	1821	19	1881	33	107
A1447_zr33	81	79	183	354	4.8567	0.1136	0.0010	5.127	0.111	0.327	0.007	0.91	1858	16	1841	18	1825	32	98
A1447_zr34	86	97	207	2686	0.6409	0.1140	0.0011	5.366	0.118	0.341	0.007	0.89	1864	18	1879	19	1894	33	102
A1447_zr35	67	67	166	314074	0.0055	0.1160	0.0013	5.472	0.123	0.342	0.007	0.88	1895	19	1896	19	1897	34	100
A1447_zr36	66	80	162	302349	0.0057	0.1167	0.0012	5.448	0.120	0.338	0.007	0.89	1907	18	1892	19	1879	33	99
A1447_zr37	26	19	66	123662	0.0139	0.1155	0.0015	5.403	0.126	0.339	0.007	0.84	1888	23	1885	20	1883	34	100
A1447_zr38	72	58	172	549	3.1371	0.1054	0.0010	4.947	0.108	0.340	0.007	0.90	1721	17	1810	18	1889	33	110
A1447_zr39	72	64	182	340463	0.0051	0.1159	0.0011	5.428	0.119	0.340	0.007	0.90	1894	17	1889	19	1885	33	100
A1447_zr40	74	53	120	93	18.5561	0.1279	0.0011	5.700	0.123	0.323	0.007	0.91	2069	15	1931	18	1806	32	87
A1447_zr41	111	97	152	62	27.9262	0.1466	0.0012	6.266	0.134	0.310	0.006	0.92	2307	14	2014	19	1741	31	75
A1447_zr42	80	56	171	221	7.7875	0.1132	0.0010	5.133	0.111	0.329	0.007	0.91	1852	16	1842	18	1832	32	99
A1447_zr43	91	64	178	214	8.0318	0.1115	0.0010	5.422	0.118	0.353	0.007	0.91	1824	16	1888	18	1948	34	107
A1447_zr44	41	33	98	659	2.6136	0.1120	0.0012	5.130	0.115	0.332	0.007	0.88	1832	20	1841	19	1849	33	101
A1447_zr45	73	54	148	261	6.6002	0.1144	0.0011	5.515	0.120	0.350	0.007	0.90	1870	17	1903	19	1933	34	103

Supplementary Material Table 8: LA-ICP-MS U-Pb data for zircon grains from sample A1675 of Talikka and Mänttäri (2005).

Sample-grain	Concentration in ppm			Isotopic ratios									Age (Ma)						
	Pb	Th	U	$^{206}Pb/^{204}Pb$	$^{206}Pbc(\%)$	$^{207}Pb/^{206}Pb$	1s	$^{207}Pb/^{235}U$	1s	$^{206}Pb/^{238}U$	1s	r	$^{207}Pb/^{206}Pb$	1s	$^{207}Pb/^{235}U$	1s	$^{206}Pb/^{238}U$	1s	Concordance %
A1675_zr01	89	85	231	419161	0.0041	0.1161	0.0014	5.272	0.120	0.329	0.007	0.86	1897	21	1864	19	1835	33	97
A1675_zr02	88	76	225	410098	0.0042	0.1156	0.0014	5.271	0.121	0.331	0.007	0.86	1889	21	1864	19	1842	33	97
A1675_zr03	114	116	284	531462	0.0032	0.1158	0.0012	5.432	0.121	0.340	0.007	0.89	1892	18	1890	19	1888	33	100
A1675_zr04	87	90	232	1693	1.0169	0.1153	0.0012	4.887	0.108	0.307	0.006	0.89	1885	18	1800	18	1728	31	92
A1675_zr05	110	71	282	539218	0.0032	0.1151	0.0011	5.514	0.121	0.348	0.007	0.90	1881	18	1903	19	1923	34	102
A1675_zr06	117	124	269	545613	0.0032	0.1155	0.0011	5.860	0.128	0.368	0.007	0.90	1887	17	1955	19	2021	35	107
A1675_zr07	52	41	142	2308	0.7458	0.1139	0.0012	4.943	0.110	0.315	0.006	0.88	1863	19	1810	19	1764	31	95
A1675_zr08	63	60	154	297082	0.0058	0.1158	0.0014	5.596	0.128	0.350	0.007	0.86	1893	21	1916	20	1936	34	102
A1675_zr09	49	35	127	236535	0.0073	0.1163	0.0013	5.412	0.122	0.338	0.007	0.88	1899	19	1887	19	1875	33	99
A1675_zr10	99	94	241	3949	0.4359	0.1148	0.0012	5.481	0.122	0.346	0.007	0.89	1877	19	1898	19	1917	34	102
A1675_zr11	82	63	215	395776	0.0043	0.1158	0.0011	5.346	0.118	0.335	0.007	0.90	1892	17	1876	19	1862	33	98
A1675_zr12	260	357	623	1174739	0.0015	0.1158	0.0012	5.476	0.122	0.343	0.007	0.89	1892	19	1897	19	1901	33	100
A1675_zr13	75	60	190	360064	0.0048	0.1169	0.0013	5.553	0.126	0.344	0.007	0.86	1910	21	1909	19	1908	34	100
A1675_zr14	59	47	151	284496	0.0061	0.1161	0.0012	5.464	0.122	0.341	0.007	0.88	1896	19	1895	19	1893	33	100
A1675_zr15	128	119	300	5612	0.3067	0.1137	0.0012	5.627	0.125	0.359	0.007	0.89	1859	18	1920	19	1977	35	106
A1675_zr16	105	94	264	4041	0.4260	0.1126	0.0012	5.258	0.119	0.339	0.007	0.87	1842	20	1862	19	1880	33	102
A1675_zr17	70	75	172	3180	0.5413	0.1148	0.0012	5.390	0.120	0.341	0.007	0.89	1876	19	1883	19	1889	33	101
A1675_zr18	131	110	322	1830	0.9406	0.1130	0.0015	5.287	0.126	0.339	0.007	0.82	1847	24	1867	20	1884	34	102
A1675_zr19	68	63	187	320285	0.0054	0.1158	0.0012	4.987	0.111	0.312	0.006	0.88	1892	19	1817	19	1753	31	93
A1675_zr20	64	55	166	301902	0.0057	0.1169	0.0013	5.346	0.121	0.332	0.007	0.87	1910	20	1876	19	1846	33	97
A1675_zr21	90	91	221	419032	0.0041	0.1173	0.0013	5.572	0.125	0.345	0.007	0.87	1915	20	1912	19	1909	34	100
A1675_zr22	81	55	208	391000	0.0044	0.1166	0.0015	5.497	0.129	0.342	0.007	0.84	1905	23	1900	20	1896	34	100
A1675_zr23	127	132	314	593972	0.0029	0.1163	0.0012	5.529	0.123	0.345	0.007	0.89	1900	18	1905	19	1910	33	101
A1675_zr24	71	64	178	336333	0.0051	0.1171	0.0013	5.549	0.125	0.344	0.007	0.87	1913	20	1908	19	1904	34	100
A1675_zr25	89	55	258	431024	0.0040	0.1179	0.0013	4.954	0.111	0.305	0.006	0.88	1924	19	1811	19	1715	31	89
A1675_zr26	95	73	244	458877	0.0038	0.1151	0.0012	5.425	0.121	0.342	0.007	0.88	1881	19	1889	19	1896	33	101
A1675_zr27	68	44	174	328941	0.0052	0.1174	0.0013	5.584	0.127	0.345	0.007	0.87	1917	20	1914	19	1910	34	100
A1675_zr28	147	121	344	696864	0.0025	0.1151	0.0013	5.858	0.132	0.369	0.008	0.87	1881	20	1955	19	2026	35	108
A1675_zr29	91	93	229	424823	0.0041	0.1146	0.0014	5.350	0.123	0.338	0.007	0.86	1874	21	1877	19	1879	33	100
A1675_zr30	115	139	285	530553	0.0032	0.1153	0.0013	5.392	0.122	0.339	0.007	0.87	1884	20	1884	19	1883	33	100
A1675_zr31	74	83	180	343944	0.0050	0.1181	0.0015	5.681	0.132	0.349	0.007	0.84	1927	22	1928	20	1930	34	100
A1675_zr32	101	67	248	484685	0.0036	0.1163	0.0014	5.722	0.131	0.357	0.007	0.85	1900	21	1935	20	1967	35	104
A1675_zr33	86	89	210	399129	0.0043	0.1180	0.0013	5.646	0.127	0.347	0.007	0.88	1927	19	1923	19	1920	34	100
A1675_zr34	98	94	264	3540	0.4862	0.1152	0.0013	5.036	0.115	0.317	0.006	0.86	1882	21	1825	19	1776	32	94
A1675_zr35	59	77	145	266877	0.0065	0.1159	0.0014	5.364	0.123	0.336	0.007	0.85	1894	21	1879	19	1866	33	98
A1675_zr36	123	100	297	585541	0.0029	0.1156	0.0014	5.744	0.132	0.360	0.007	0.86	1890	21	1938	20	1984	35	105
A1675_zr37	96	90	244	456077	0.0038	0.1158	0.0014	5.451	0.126	0.342	0.007	0.85	1892	22	1893	20	1894	34	100
A1675_zr38	67	88	169	307072	0.0056	0.1167	0.0016	5.327	0.127	0.331	0.007	0.82	1907	24	1873	20	1843	33	97
A1675_zr39	110	99	275	518481	0.0033	0.1147	0.0017	5.439	0.134	0.344	0.007	0.79	1876	27	1891	21	1905	34	102
A1675_zr40	54	48	188	256376	0.0067	0.1163	0.0014	3.999	0.092	0.249	0.005	0.85	1901	22	1634	19	1435	26	76
A1675_zr41	42	37	108	199829	0.0086	0.1152	0.0016	5.369	0.128	0.338	0.007	0.82	1882	24	1880	20	1878	34	100
A1675_zr42	77	63	194	3029	0.5682	0.1133	0.0013	5.321	0.122	0.341	0.007	0.86	1853	21	1872	19	1890	33	102
A1675_zr43	104	112	252	482503	0.0036	0.1166	0.0015	5.617	0.130	0.349	0.007	0.85	1904	22	1919	20	1932	34	101
A1675_zr44	54	49	140	259084	0.0066	0.1152	0.0014	5.380	0.125	0.339	0.007	0.85	1883	22	1882	20	1880	33	100